Fermilab

FERMILAB-THESIS-1999-25

A Measurement of b-quark Fragmentation Fractions in $\overline{p}p$ Collisions at $\sqrt{s} = 1.8$ TeV

by

Wendy Jane Taylor

A thesis submitted in conformity with the requirements
for the degree of Doctor of Philosophy,
Graduate Department of Physics,
University of Toronto

Abstract

Fragmentation is the process by which quarks and gluons organize themselves into hadrons. The fragmentation properties of the bottom quark cannot be predicted from fundamental principles and hence must be determined empirically. We investigate one such property, namely the flavour dependence of the fragmentation process for bottom quarks produced in 1.8-TeV proton-antiproton collisions. This flavour dependence is investigated by determining the B-hadron production ratios.

We use a sample of $\overline{p}p$ data corresponding to an integrated luminosity of 110 pb^{-1} and reconstruct the following semileptonic B-hadron decays into electrons and charmed hadrons: $B^+ \to e^+\nu_e\overline{D}^0 X$, $B^0 \to e^+\nu_e D^{*-} X$, $B^0 \to e^+\nu_e D^- X$, $B_s^0 \to e^+\nu_e D_s^- X$ and $\overline{\Lambda}_b^0 \to e^+\nu_e\Lambda_c^- X$. With these data, we measure the ratios of fragmentation fractions

$$\begin{aligned} f_d/f_u &= (88 \pm 21)\%, \\ f_s/(f_u + f_d) &= (21.5 \pm 7.1)\% \text{ and} \\ f_{baryon}/(f_u + f_d) &= (12.0 \pm 4.2)\%. \end{aligned}$$

Assuming that these four hadrons saturate production of weakly-decaying B hadrons, that is, that $f_u + f_d + f_s + f_{baryon} \equiv 1$, we determine

$$\begin{aligned} f_u &= (39.8 \pm 5.4)\%, \\ f_d &= (35.2 \pm 4.8)\%, \\ f_s &= (16.1 \pm 4.5)\% \text{ and} \\ f_{baryon} &= (9.0 \pm 2.9)\%. \end{aligned}$$

These results represent the first measurement of all four b-quark fragmentation fractions in a single experiment. These fractions are in agreement both with previous phenomenological interpretations and with other experimental measurements.

Acknowledgements

I have enjoyed the assistance and support of many people throughout the duration of my research career. First and foremost, I must thank my supervisor, Professor Pekka Sinervo for giving me the opportunity to pursue this degree. It was a pleasure to collaborate with Pekka and his confidence in me helped me through more than a few rough spots. Pekka's encouragement and patience were important ingredients to my success.

My CDF colleague and office mate, Dr. Björn Hinrichsen, has been a good friend and confidant. Our frequent venting sessions were essential for maintaining my sanity through the tough times. I will certainly miss them.

I would also like to thank my other CDF colleagues at Toronto, in particular, Dr. Andreas Warburton, Professor William Trischuk, Dr. Szymon Gadomski and Dr. Andreas Hölscher. They were great resources and always took the time to offer advice and exchange knowledge.

Dr. Cortney Sampson also deserves great thanks. His willingness to help and interminable patience were most appreciated. He also was an exceptional drinking companion.

I have several CDF colleagues who have been helpful. Dr. Barry Wicklund, Dr. Karen Byrum and Dr. Jonathan Lewis have all contributed to this work. Dr. Jeff Tseng always managed to squeeze in a few moments to help with crucial aspects of the analysis. I am indebted to Professor Joe Kroll for helping to guide me along the path that I now tread.

Financial support for this work came in part from the National Science and Engineering Research Council, the University of Toronto, the Department of Physics and my supervisor, Professor Pekka Sinervo. I would like to thank all parties for their generous contributions.

I would like to thank Dr. Paul Padley for inspiring me to pursue a graduate degree and for convincing me that I was good enough to do so. Paul continues to have a hand in securing a successful future for me and I am indebted to him for that. I must also thank Dr. Mark Sutherland for the wonderful education he provided during my

course work at Toronto. Mark's time and effort went a long way to ensuring that I was well prepared for my graduate research work.

Finally, I would like to thank Dr. James Brown for his unwavering confidence, support and love always.

Contents

List of Tables

List of Figures

Chapter 1

Introduction

As long ago as the fifth century B.C., philosophers studied the essential nature of matter, a pursuit called physis by the ancient Greeks. At that time, the Greek philosopher Democritus developed the idea that all matter was made up of small indivisible objects called atoms. The idea of the atom persisted through the ages until the early nineteenth century when John Dalton expanded upon the work of his predecessors. He suggested that the chemical elements differed from one another because each one was made up of a specific kind of atom [1]. In 1869, Dmitry Mendeleev organized the elements according to their atomic weights and chemical properties into what is now known as the Periodic Table of Elements. He found three gaps in the table and predicted the existence of three elements with specific characteristics. A few years later, the three elements predicted by Mendeleev, gallium, scandium and germanium, were discovered.

Atoms, however, were not the indivisible units of matter that Democritus had postulated. In 1896, Henri Becquerel discovered while studying uranium salts that the element uranium spontaneously emitted radiation [2, 3]. One year later, J. J. Thomson showed that cathode rays observed when a current was passed through a rarified gas were actually beams of electrically-charged particles streaming from the negative electrode (cathode) to the positive electrode (anode) [4, 5]. These negatively-charged particles came to be called electrons and it was originally thought that they came from the atoms in the cathode. Since atoms were known to be electrically

neutral, it was then proposed that there must be a positively-charged portion of the atom.

Fourteen years later, Ernest Rutherford and his colleagues aimed a beam of doubly-charged α-particles at a sheet of gold foil and discovered that while most beam particles passed straight through the foil, some were deflected at large angles [6]. He inferred that the positively-charged portion of the gold atom was densely packed at the atomic centre. This atomic nucleus was believed to be made of positively-charged particles called protons. In the subsequent twenty years, it became clear that the atomic nucleus also contained neutral particles called neutrons, as discovered by J. Chadwick in 1932 [7].

The discovery of the neutron posed two new problems for physicists. First, it became obvious that a new force of nature must exist to bind together the neutrons and the protons inside the nucleus. Such a force would have to be of very short range ($\sim 10^{-10}$ m) and very strongly attractive to overcome the electromagnetic repulsion of the protons confined to the small volume of the nucleus. Second, the neutron was found to decay spontaneously into a proton and an electron with a half-life of fifteen minutes. This radioactive β decay, as it was called, had a time scale much too long to be attributable to the strong or electromagnetic force. It appeared that a third, much weaker force was at play.

Studies of β decay revealed another puzzle. The energy of the electrons emitted by the decay of a particular element was not simply the energy difference between the parent and daughter atomic masses; rather, it was a continuous spectrum, where the electrons were observed at all energies up to a maximum equivalent to the parent-daughter mass difference. In 1933, Wolfgang Pauli postulated that a third particle, the neutrino, was produced in β decay [8]. Such a particle was neutral and very light, if not massless.

Around the same time, Paul Dirac hypothesized the existence of a positively-charged particle with the same characteristics as an electron except for its charge [9]. This anti-electron, or positron as it came to be called, was discovered in 1933 by Carl Anderson in a cloud chamber experiment [10].

Scientists soon discovered other kinds of particles. The muon, discovered in 1936 [11], was found to have properties much like a heavy electron, although it was originally thought to be the pion proposed by H. Yukawa the previous year [12]. Yukawa had postulated that the strong force binding neutrons and protons together inside the nucleus was mediated by a massive particle, called a π meson or pion. The mass of the mediating particle would ensure that the force only acts over a finite range. The pion was eventually discovered in 1947 [13, 14], even though it was soon apparent that it was not the mediator of the strong force.

Pions, like protons, are strongly-interacting particles, however, and are thus classified as hadrons. Electrons and muons do not experience the strong interaction and are thus classified as leptons. In the early 1950s, several other hadrons were discovered, including the Λ^0, Δ^{++}, Δ^+, Δ^0, Δ^-, and eventually the Σ and the Ξ particles. There appeared to be an unreasonable number of "elementary" particles, so in 1961, Murray Gell-Mann [15, 16] and Yurval Ne'eman [17] independently developed a scheme of ordering the hadrons into families. Gell-Mann used his theory to predict the existence of an as-yet unknown particle, the Ω^- [18], which was discovered only a year later [19]. This classification scheme was further extended by Gell-Mann [20] and, independently, G. Zweig [21, 22], resulting in the hypothesis that all hadrons were composed of objects called "quarks". Three types of quarks were required to explain the hadrons known at that time.[1]

1.1 The Standard Model

The Standard Model of particle physics is the theoretical structure that originated with the work of Gell-Mann and Ne'eman, with many physicists having contributed to its subsequent development [23, 24, 25]. In the Standard Model, matter is made up of six types of quarks and six types of leptons. Quarks come in different flavours, such as up (u) or down (d), each carrying a fractional charge. Along with the leptons, they can be classified into generations, as shown below, where the particles in a given

[1] Three more quarks have been discovered since that time, for a total of six types of quarks.

generation are placed in the same column:

$$\begin{array}{cccc} & & & \text{Charge} \\ \begin{pmatrix} u \\ d \end{pmatrix} & \begin{pmatrix} c \\ s \end{pmatrix} & \begin{pmatrix} t \\ b \end{pmatrix} & \begin{matrix} +\frac{2}{3} \\ -\frac{1}{3} \end{matrix} \\ \begin{pmatrix} e \\ \nu_e \end{pmatrix} & \begin{pmatrix} \mu \\ \nu_\mu \end{pmatrix} & \begin{pmatrix} \tau \\ \nu_\tau \end{pmatrix} & \begin{matrix} -1 \\ 0 \end{matrix} \end{array}$$

Each quark and lepton has an associated antiparticle.

The order of the generations represents the progression of masses of the quarks, where the u, d and s quarks are light (< 1 GeV/c^2), the c and b quarks are heavy (1.5 and 5 GeV/c^2, respectively) and the t quark, discovered recently by two experiments at the Fermilab Tevatron [26, 27, 28, 29], is surprisingly heavy, with a mass 180 times that of the proton, or about 175 GeV/c^2. The charged leptons are also ordered according to increasing mass, but currently only upper mass limits exist for the neutrinos[2]. The relative mass scales are not yet understood, except that the three generations appear to be distinguished from one another by the energy level at which they exist. The Universe is currently dominated by particles in the first generation, but particles in the second and third generations can be produced at high energies, such as those associated with the early moments of the Big Bang.

In the Standard Model, the quarks and leptons interact with one another via three forces[3], shown in Table 1.1 with their mediating particle. The electromagnetic force binds electrons and atomic nuclei together. The strong force binds the protons and neutrons together within atoms (and the quarks together within hadrons). The weak force is responsible for radioactive decays. We now consider the electromagnetic and weak forces as two manifestations of the same force, which we call the electroweak

[2]We note that there is no special relationship between the leptons and the quarks in each generations except for the relative mass scales at which they exist.

[3]The fourth known force, gravity, has not yet been successfully incorporated into the Standard Model. However, its action is so weak that it is not relevant on a subatomic scale.

Force	Mediators	Range
Electromagnetic	γ	∞
Weak	$W^{\pm}, Z^{\circ}$ bosons	$\sim 10^{-18}$ m
Strong	eight gluons	$\sim 10^{-15}$ m

Table 1.1: The three forces governing the interactions of quarks and leptons and their mediating particles.

force.

The electroweak coupling of the $W^{\pm}$ boson to leptons of all three generations occurs with the same coupling strength. In contrast, the strengths of the couplings to quarks appear to be related to the magnitudes of the quark masses. Quark transitions within the same generation are favoured, but transitions across generations also occur. A 3×3 matrix of constants known as the Cabibbo-Kobayashi-Maskawa matrix [30, 31],

$$V = \begin{pmatrix} V_{ud} & V_{us} & V_{ub} \\ V_{cd} & V_{cs} & V_{cb} \\ V_{td} & V_{ts} & V_{tb} \end{pmatrix}, \tag{1.1}$$

describes the electroweak couplings of the quarks to the $W^{\pm}$ boson. The element V_{ub}, for example, describes the strength of the electroweak coupling of b quarks to u quarks.

1.2 Quarks and Hadrons

Free quarks have never been observed in the laboratory; rather, quarks have only been identified bound inside hadrons, such as mesons (a $q\overline{q}$ state) or baryons (a qqq state). The theory of Quantum Chromodynamics (QCD), the element of the Standard Model that describes the strong force, provides an explanation for this phenomenon of confinement. QCD is a renormalizable gauge theory similar to Quantum Electrodynamics

(QED), the gauge theory describing electromagnetic interactions. QCD states that each quark flavour comes in three different colours. Thus, the strong force binding quarks together is mediated via the exchange of eight types of massless vector bosons (called gluons) that carry a property called colour charge. This confined system of quarks and gluons (generically called partons) is what we refer to as a hadron. The term parton also includes the sea of $q\overline{q}$ pairs inside the hadron that arise naturally in QCD.

There are three possible colours for a quark; we arbitrarily choose red, green and blue as their labels. A red quark has colour R and a green antiquark has colour $\overline{G}$. Hadrons are combinations of two or three coloured quarks such that the resulting bound state is "colourless". The eight gluons are associated with the colour combinations

$$R\overline{B}, R\overline{G}, B\overline{R}, G\overline{R}, B\overline{G}, G\overline{B}, (R\overline{R} - G\overline{G})/\sqrt{2}, \text{ and } (R\overline{R} + G\overline{G} - 2B\overline{B})/\sqrt{6}.$$

Since the gluons carry the colour charge themselves, they can couple to each other.

The property of gluon self-interaction gives rise to a phenomenon known as colour-charge screening. We consider a quark with a red colour charge. The red quark can emit gluons that can then create quark-antiquark pairs. However, because gluons can couple to other gluons, we also have the configuration where the emitted gluon turns into a pair of gluons. In QCD, therefore, a red quark is preferentially surrounded by other red colour charges. A test quark would experience a decrease in colour charge as it penetrates the sphere of red charge surrounding the red quark. As two quarks approach at small distances, the colour strength between them diminishes such that they become essentially free, non-interacting particles. This effect is referred to as asymptotic freedom. For the same reason, as a test quark is moved away from its partner, it experiences an increase in force due to the larger colour charge as the distance of separation increases. Thus, QCD is capable of describing the two observed properties of quarks: that they experience asymptotic freedom at short distances and quark confinement at long distances. The QCD running coupling constant, α_s,

which is a measure of the strength of the strong interaction, reflects this behaviour as it decreases as the momentum transfer of the QCD interaction between the quarks increases. Despite this qualitatively correct picture of the strong interaction, the long-distance behaviour of QCD is not fully understood, motivating further experimental studies of these non-perturbative effects.

1.3 Heavy Quarks

In 1970, three quarks were known to exist: up (u), down (d) and strange (s). At that time, it was known that strangeness-changing neutral currents in kaon decays were heavily suppressed compared to the charged currents (i.e., $\mathcal{B}(K^+ \to \pi^+\nu\bar{\nu})/\mathcal{B}(K^+ \to \pi^0\mu^+\nu_\mu) < 10^{-5}$, where $\mathcal{B}$ refers to the branching fraction of a decay). S. L. Glashow, J. Iliopoulos and I. Maiani showed that this suppression could be accommodated in the quark model if there existed a new, much heavier quark [32]. This theory was called the GIM mechanism and the quark was called "charm" (c).

The GIM hypothesis represented a generalization of the three-quark model proposed earlier by Zweig and Gell-Man. The four-quark model was confirmed by the surprising discovery in 1974 of a heavy particle, the J/ψ meson, produced in e^+e^- annihilation [33, 34] and in collisions of 28-GeV protons on a Be target [35]. This long-lived particle was recognized as the bound state of a heavy quark and its antiparticle, and its mass was consistent with the estimate predicted earlier by M. K. Gaillard and B. W. Lee [36].

The four-quark model soon expanded into a six-quark model when the fifth quark, called bottom (b), was discovered in 1977 by a Fermilab fixed-target experiment[4]. The bottomonium ($b\overline{b}$) bound state was observed as a resonance at 9.5 GeV/c^2 in the dimuon invariant mass spectrum measured in proton-nucleus collisions [37].

The discovery of the b quark confirmed the presence of the third generation of matter but provided no insight as to why multiple generations existed. The b quark

[4]The discovery of the fifth quark implied the presence of a partner to complete the third generation.

did, however, provide a means of probing the generation puzzle; since the b quark is lighter than the t quark, it can only decay into quarks of either the first (u) or second (c) generations. This unique situation makes b-quark decays the ideal laboratory for measuring the CKM matrix elements V_{ub} and V_{cb}.

However, b quarks are not observed as independent entities but are confined with a partner antiquark or diquark inside hadrons. Once a b quark is produced, the process by which it combines with quarks and gluons to form a hadron is called hadronization or fragmentation and is governed by QCD. The Standard Model does not predict from fundamental principles the fragmentation properties of the b quark and hence they must be determined empirically. In this dissertation, we investigate one such property, namely the flavour dependence of the fragmentation process for bottom quarks produced in $\overline{p}p$ collisions.

1.3.1 Heavy Quark Production

Bottom quarks are most readily produced in high-energy hadronic interactions. In $\overline{p}p$ interactions, the $b\overline{b}$ quark pairs are produced via the hard collision of a parton from each hadron, according to the process

$$p + \overline{p} \;\; \rightarrow \;\; b + \overline{b} + X. \tag{1.2}$$

The heavy quark production cross section can be calculated as a perturbation series expanded in powers of the QCD running coupling constant α_s, evaluated at the mass of the heavy quark. Quark-antiquark annihilation and gluon-gluon fusion processes, shown in Figure 1.1, occur at lowest order ($\mathcal{O}(\alpha_s^2)$). The remaining partons not participating in the hard collision are represented by X in Equation 1.2. These hadron remnants are what we refer to as the underlying event and result in a spray of particles with low transverse momenta to the proton-antiproton beam.

There are several higher order processes that produce a $b\overline{b}$ pair accompanied by an additional light quark or gluon, some examples of which are shown in Figure 1.2. P. Nason, S. Dawson and R. K. Ellis (NDE) [38, 39] have calculated the parton-level

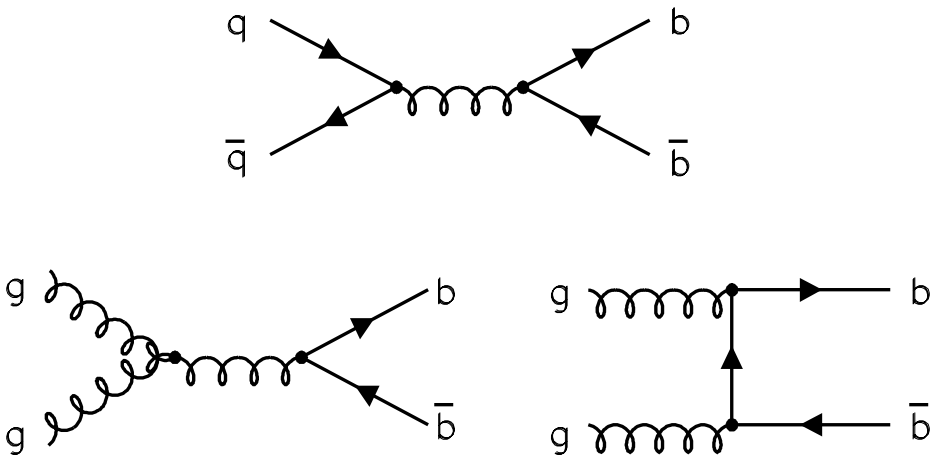

Figure 1.1: Leading order Feynman diagrams depicting b-quark production by quark-antiquark annihilation and gluon-gluon fusion.

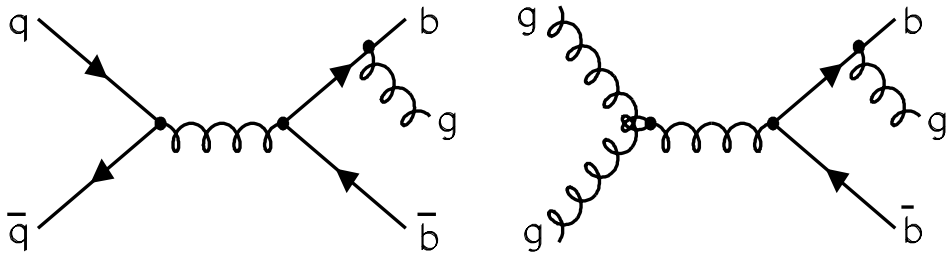

Figure 1.2: Feynman diagrams depicting $\mathcal{O}(\alpha_s^3)$ mechanisms of b-quark production.

heavy quark production cross sections to order α_s^3. They found that the $\mathcal{O}(\alpha_s^3)$ terms in the α_s expansion are similar in magnitude to the lowest-order terms and thus can not be considered as simply higher-order "corrections" to the leading order terms. The gluon-gluon fusion process dominates at both $\mathcal{O}(\alpha_s^2)$ and $\mathcal{O}(\alpha_s^3)$.

These authors have also calculated to $\mathcal{O}(\alpha_s^3)$ the differential heavy quark production cross sections $d^3\sigma/dy\,dP_T^2$, where σ is the production cross section, y is the rapidity and P_T is the heavy quark momentum transverse to the proton-antiproton beam. Rapidity[5] is a quantity related to the polar angle of the particle's direction.

The results of these calculations depend on the mass of the heavy quark, m, and the "renormalization scale", μ. The authors chose the scale $\mu = \mu_0 = \sqrt{m^2 + P_T^2}$ and suggest that variations from $\mu = \mu_0/2$ to $\mu = 2\mu_0$ are sufficient to incorporate the

[5]Rapidity is defined as $y \equiv \frac{1}{2}\ln\left(\frac{E+P_z}{E-P_z}\right)$.

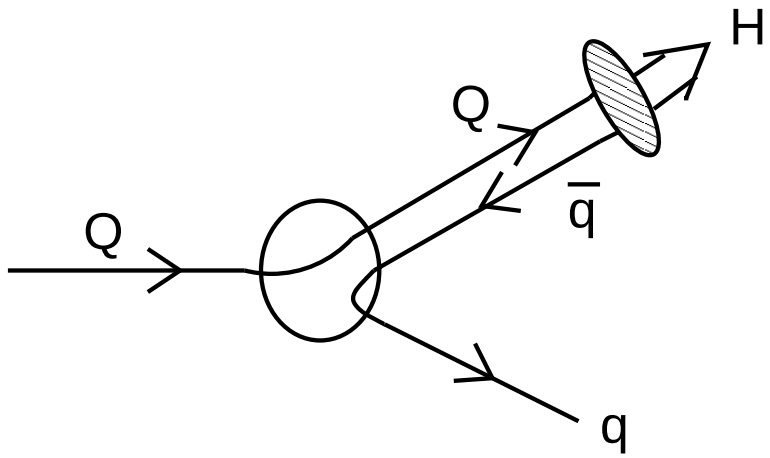

Figure 1.3: The fragmentation of a heavy quark Q into a meson $H(Q\overline{q})$.

range of uncertainty in this choice.

1.3.2 Heavy Quark Fragmentation

After a heavy quark is produced in a hard collision between partons, colour forces "dress up" the heavy quark into a hadron. In this fragmentation process, the colour force field creates additional quark-antiquark partners, one of which combines with the initial produced heavy quark, as represented in Figure 1.3.

Unlike parton production, the "long-distance" process by which a parton fragments into a hadron cannot be reliably calculated using perturbative QCD methods. In order to compare experiment to theory, several phenomenological models have been created that attempt to describe hadronization. These models normally assume that the hadronization process is decoupled from the initial parton production. This is expected to be a reasonable assumption since the time scales for the initial hard QCD processes are believed to be significantly shorter than those of the soft fragmentation processes.

Lund String Fragmentation Model

A popular phenomenological approach is the Lund string fragmentation model [40]. In this model, the attractive force between a quark and an antiquark in a meson is

represented by colour flux lines due to gluon exchange. The strong colour field is confined to a tube or "string" that has constant energy density per unit length (i.e., $E \propto \kappa \cdot l$, where κ represents the string constant and l is the distance between the quarks). As a quark is pulled out of its confining hadron (in this example, a meson), the color flux string lengthens and the energy between the two quarks increases proportionally. As the quarks move apart, they are decelerated by the string tension.

In the Lund model, the fragmentation of the initial quark into the resulting jet is essentially a quantum mechanical process. The quarks can be separated from one another until the energy in the system is sufficient to create a $q\overline{q}$ pair at an intermediate point on the colour flux string. Since the total colour of the final hadrons is neutral, the colour charge of the scattered quark is exactly balanced by the colour charge of the recoiling system (in this example, the antiquark). The probability $\mathcal{P}$ for this occurring at some point x on the string at some time t is uniform in space and time and is given by

$$\frac{d^2\mathcal{P}}{dxdt} = \text{Constant} \cdot \exp\left(-\frac{\pi}{\hbar c}\frac{m^2c^4}{\kappa}\right), \tag{1.3}$$

where m is the mass of the created quarks. This formula is analogous to that describing the tunneling probability through a potential barrier. Since the colour force field is assumed to be uniform save for the string constant κ, no concentrations of energy can appear along the field, hence the massive $q\overline{q}$ partners must be produced some distance apart from each other. The quarks are produced such that they are separated by a distance $2l$, with the quark at $x = +l$ and the antiquark at $x = -l$. The field energy between them is absorbed by the creation of mass. Thus, we have

$$2\kappa \cdot l = 2mc^2. \tag{1.4}$$

Using values $\kappa \approx 1$ GeV/fm (i.e., $\hbar c\kappa \approx 0.2$ GeV^2), $m_u \approx m_d \approx 0.01$ GeV/c^2, $m_s \approx 0.25$ GeV/c^2 and $m_c \approx 1.2$ GeV/c^2, the Lund model predicts the following

production ratios of $q\overline{q}$ partners from the vacuum:

$$u : d : s : c \approx 1 : 1 : 1/3 : 10^{-10}. \tag{1.5}$$

The Lund model assumes that further hadronization occurs locally, such that the initial partons continue to fragment independently of each other. With this description, one predicts the resulting final state to form "jets" of particles - one quark jet and one jet associated with each energetic parton in the recoil system, which typically arises from a single parton. The finite transverse cross section of the colour flux tube gives rise to a momentum spread transverse to the direction of fragmentation of the hadrons in the jet as governed by the Heisenberg Uncertainty Principle. In the centre-of-momentum frame, these jets typically leave the interaction region back-to-back.

Peterson Parametrization

A fragmentation property crucial to our understanding of heavy hadron production is the fraction of parent quark energy-momentum carried by the resulting heavy hadron. C. Peterson *et al.* [42] have proposed a simple model to describe the energy dependence of heavy quark fragmentation into mesons or baryons containing a light quark or light diquark, respectively. Their result follows from the hypothesis that a fast-moving heavy quark Q loses negligible energy when it picks up a light antiquark $\overline{q}$ (or a diquark qq for baryon production). The transition amplitude of a heavy quark fragmenting into a hadron $H = Q\overline{q}$ is governed by the energy transfer in the process, i.e.,

$$\Delta E = E_H + E_q - E_Q. \tag{1.6}$$

Assuming $m_H \approx m_Q$ for simplicity, we have

$$\begin{aligned} \Delta E &= (m_Q^2 + z^2 P_Q^2)^{1/2} + (m_q^2 + (1-z)^2 P_Q^2)^{1/2} - (m_Q^2 + P_Q^2)^{1/2} \\ &\propto 1 - 1/z - \epsilon_Q/(1-z), \end{aligned} \tag{1.7}$$

where P_Q is the momentum of the heavy quark and z is the fraction of the available energy-momentum carried by the heavy hadron, i.e.,

$$z = \frac{(E_H + P_{\parallel}(H))}{(E_Q + P_Q)}, \tag{1.8}$$

and the quantity $\epsilon_Q \sim m_q^2/m_Q^2$ is an input parameter to be measured empirically for individual hadron species. The symbol $P_{\parallel}(H)$ represents the hadron momentum component parallel to the direction of the parent heavy quark. Applying first-order perturbation theory and including an additional factor of z^{-1} to account for longitudinal phase space, one arrives at the Peterson heavy quark fragmentation function,

$$D_Q^H(z) \;=\; \frac{1}{z[1 - 1/z - \epsilon_Q/(1-z)]^2}. \tag{1.9}$$

The Peterson fragmentation function $D_Q^H(z)$ represents the probability of generating the hadron H in the fragmentation of the quark Q with the energy-momentum fraction z. The quantity ϵ_Q is called the Peterson parameter. J. Chrin compiled results from e^+e^- annihilation experiments [43] to determine $\epsilon_b = 0.006 \pm 0.001 \pm 0.002$ for a mixture of bottom-flavoured hadrons produced in high-energy matter-antimatter collisions.

1.3.3 b-Quark Fragmentation Fractions

The bottom antiquarks produced in proton-antiproton collisions fragment into hadrons, such as B^+, B^0, B_s^0 mesons and $\overline{\Lambda}_b^0$ baryons, by combining with a u, d, s quark or a $\overline{u}\overline{d}$ diquark system. We define f_u, f_d, f_s and f_{baryon} to be the probabilities that the fragmentation of a $\overline{b}$ antiquark will result in a B^+, B^0, B_s^0 meson and $\overline{\Lambda}_b^0$ baryon, respectively, and refer to these probabilities as fragmentation fractions.

The values of the b-quark fragmentation fractions are important for measurements of the CKM matrix elements V_{ub} and V_{cb} and the $B - \overline{B}$ mixing parameters Δm_d and Δm_s, as well as B hadron lifetime and decay branching fraction measurements. These fragmentation fractions cannot be reliably calculated using perturbative QCD

methods, therefore, they must be measured empirically.

The b-quark fragmentation fractions have been measured by several experiments. The CLEO experiment determined the ratio f_d/f_u in $\Upsilon(4S) \to B\overline{B}$ decays by reconstructing $B \to D^* l\nu$ decays [44]. Assuming equal partial widths, that is, , $(B^0 \to D^{*-} l^+ \nu) =$, $(B^+ \to D^{*0} l^+ \nu)$, they found

$$\frac{f_d}{f_u} = \frac{\mathcal{B}(\Upsilon(4S) \to B^+ B^-)}{\mathcal{B}(\Upsilon(4S) \to B^0 \overline{B}^0)} = (88 \pm 11 \pm 10 \pm 5)\%, \tag{1.10}$$

where the last error is due to the uncertainties in the ratio of the B^0 and B^+ lifetimes. CLEO obtained a similar result using hadronic $B^+ \to J/\psi K^{(*)+}$ and $B^0 \to J/\psi K^{(*)0}$ decays and assuming equal partial widths , $(B^+ \to J/\psi K^{(*)+}) =$, $(B^0 \to J/\psi K^{(*)0})$ [45]:

$$\frac{f_d}{f_u} = (90 \pm 14)\%. \tag{1.11}$$

Both of these measurements are consistent with the isospin symmetry expectation that $f_d = f_u$.

Heavier B hadrons are not produced at $\Upsilon(4S)$ energies, so measurements of f_s and f_{baryon} have come only from the CDF experiment and the LEP experiments. The CDF experiment measured

$$f_s/f_u \;\; = \;\; (34 \pm 10 \pm 3)\% \tag{1.12}$$

in $B \to J/\psi K$ decays [46], where B refers to B^+, B^0 and B_s^0 mesons and K refers to charged and neutral $K^{(*)}$ mesons and ϕ mesons. In this measurement, the isospin expectation, $f_d = f_u$, and a prediction for the branching fraction $\mathcal{B}(B_s^0 \to J/\Psi\phi)$ were assumed.

The CDF experiment measured $f_s/(f_u+f_d)$ using semileptonic decays of B mesons to muons and charmed mesons, where the charmed meson decays semileptonically to another muon. This novel technique yielded the ratio [47]

$$f_s/(f_u + f_d) = (20.1 \pm 3.5^{+3.9}_{-3.2})\%. \tag{1.13}$$

The ALEPH experiment reconstructed $B_s^0 \to D_s^- l^+ \nu X$ decays produced in e^+e^- collisions at the Z^0 mass [48]. Correcting their result for the world average value of $\mathcal{B}(D_s^- \to \phi\pi^-) = (3.6 \pm 0.9)\%$ [49] yields the value

$$f_s = (12.0^{+4.5}_{-3.4})\%. \tag{1.14}$$

The LEP B Oscillations Working Group has compiled $B^0\overline{B}^0$ mixing results from the four LEP experiments and the CDF experiment for the mixing parameter Δm_d. The average value of this parameter constrains the value of f_s, yielding the result [49]

$$f_s = (10.1^{+2.0}_{-1.9})\%. \tag{1.15}$$

As with f_s, the ALEPH experiment measured f_{baryon} by reconstructing $\overline{\Lambda}_b^0 \to \Lambda_c^- l^+ \nu X$ decays [50]. By combining their result with a similar measurement by the DELPHI experiment [51] and using the most recent world-average value of $\mathcal{B}(\Lambda_c^- \to \overline{p}K^+\pi^-) = (5.0 \pm 1.3)\%$, they obtain

$$f_{baryon} = (10.1^{+3.9}_{-3.1})\%. \tag{1.16}$$

It is possible to calculate the absolute branching fractions from the fragmentation fraction ratios by assuming

$$f_u + f_d + f_s + f_{baryon} = 1. \tag{1.17}$$

This assumption is expected to be reasonable since B_c production is known to be small [52] and bottom-strange baryon production is expected to be significantly smaller than $\overline{\Lambda}_b^0$ production. With this assumption, a combination of the average of the latter two f_s results with the f_{baryon} result yields the values

$$f_u = f_d = (39.7^{+1.8}_{-2.2})\%. \tag{1.18}$$

The b-quark fragmentation fractions yield information about the relative frequency

of pair creation of the light quarks from the vacuum. Creation of an $s\overline{s}$ pair is expected to be suppressed over $u\overline{u}$ and $d\overline{d}$ creation due to the heavier mass of the strange quark. Past experiments have probed this strangeness suppression by measuring light quark fragmentation, where the spectator quark in the fragmentation is either a u or a d quark. The strangeness suppression factor λ is defined as

$$\lambda \;=\; \frac{2\mathcal{P}(s\overline{s})}{\mathcal{P}(u\overline{u})+\mathcal{P}(d\overline{d})}, \tag{1.19}$$

with $\mathcal{P}$ being the pair creation probability. Bocquet *et al.* [53] used kaon and pion production rates in 630-GeV $\overline{p}p$ collisions to determine $\lambda = (29 \pm 2 \pm 1)\%$. In the same paper, a compilation of past measurements of strangeness suppression in $\bar{p}p$, pp and e^+e^- collisions shows only a slight trend to increase with increasing effective centre-of-mass energy, $\sqrt{\hat{s}_{eff}}$, of the initial state. Within the uncertainties of the experimental measurements, there is no evidence of a dependence on the spectator quark production mechanism.

The CDF experiment reported a measurement of strange meson production in $\overline{p}p$ collisions [54]. They measured $\lambda = (40 \pm 20)\%$ and $\lambda = (40 \pm 5)\%$ for $\overline{p}p$ collisions at $\sqrt{s} = 630$ GeV and $\sqrt{s} = 1800$ GeV, respectively.

New Measurements of Fragmentation Fractions

In this dissertation, we present a measurement of the relative B-hadron production rates in 1.8-TeV $\overline{p}p$ collisions. The measurement is performed by reconstructing B-hadron semileptonic decays to electrons and charmed hadrons. The ratios of the b-quark fragmentation fractions for weakly-decaying B hadrons, namely

$$\begin{gathered} f_d/f_u, \\ f_s/(f_u+f_d) \text{ and} \\ f_{baryon}/(f_u+f_d), \end{gathered} \tag{1.20}$$

are determined from the B-hadron production ratios.

We explicitly include in these fragmentation fractions contributions from produc-

B^+	$\to e^+\nu X$	$\overline{D}^0$	
		$\hookrightarrow$	$K^+\pi^-$
B^0	$\to e^+\nu X$	D^{*-}	
		$\hookrightarrow$	$\overline{D}^0\pi^-$
			$\hookrightarrow K^+\pi^-$
B^0	$\to e^+\nu X$	D^-	
		$\hookrightarrow$	$K^+\pi^-\pi^-$
B_s^0	$\to e^+\nu X$	D_s^-	
		$\hookrightarrow$	$\phi\pi^-$
			$\hookrightarrow K^+K^-$
$\overline{\Lambda}_b^0$	$\to e^+\nu X$	Λ_c^-	
		$\hookrightarrow$	$\overline{p}K^+\pi^-$

Table 1.2: B-hadron semileptonic decay channels studied in this dissertation. The electrons are identified and the charmed hadrons are reconstructed by identifying their daughter particles.

tion of heavier B hadrons that decay into final states containing a B^+, B^0, B_s^0 meson or $\overline{\Lambda}_b^0$ baryon. The advantage of measuring a ratio of fragmentation fractions is that many of the reconstruction efficiencies, such as the electron identification efficiency, cancel in the ratio.

Five B-hadron semileptonic decay channels, shown in Table 1.2, and their charge conjugates are investigated. We identify the electrons and fully reconstruct the charmed hadrons by identifying their decay products. We exploit the charge-correlation between the electron and the charmed-hadron daughter particles in the B-hadron decays to reduce the combinatorial backgrounds in the analysis.

If the decays shown in Table 1.2 were the only source of the electron–charmed-hadron final states that we reconstruct, the ratios of the b-quark fragmentation fractions could be determined from the B-hadron production ratios, as in the following

example:

$$\frac{f_s}{f_u + f_d} = \frac{N(l^+ D_s^-)}{\mathcal{B}(B_s^0 \to D_s^- l^+ \nu) \cdot \mathcal{B}(D_s^- \to \phi\pi^-) \cdot \mathcal{B}(\phi \to K^+K^-) \cdot \varepsilon(D_s^-)}$$

$$\cdot \left[\frac{N(l^+ \overline{D}^0)}{\mathcal{B}(B^+ \to \overline{D}^0 l^+ \nu) \cdot \mathcal{B}(\overline{D}^0 \to K^+\pi^-) \cdot \varepsilon(\overline{D}^0)} + \right.$$

$$\left. \frac{N(l^+ D^-)}{\mathcal{B}(B^0 \to D^- l^+ \nu) \cdot \mathcal{B}(D^- \to K^+\pi^-\pi^-) \cdot \varepsilon(D^-)} \right]^{-1}, \qquad (1.21)$$

where $N(l^+ D_s^-)$, $N(l^+ \overline{D}^0)$ and $N(l^+ D^-)$ refer to the number of D_s^-, $\overline{D}^0$ and D^- candidates we reconstruct in our lepton sample, respectively, and $\varepsilon(D_s^-)$, $\varepsilon(\overline{D}^0)$ and $\varepsilon(D^-)$ are the corresponding charmed-hadron reconstruction efficiencies. However, each electron–charmed-meson final state that we reconstruct comes from several B-meson species. For example, D^- mesons are produced in the following B^0, B^+ and B_s^0 decays:

$$B^0 \to e^+\nu \quad D^-$$

$$B^+ \to e^+\nu \quad \overline{D}^{**0}$$
$$\qquad\qquad\quad \big\lfloor\!\!\longrightarrow \quad D^-\pi^+$$

$$B_s^0 \to e^+\nu \quad D_s^{**-}$$
$$\qquad\qquad\quad \big\lfloor\!\!\longrightarrow \quad D^-K^0$$

The resulting "cross contamination" between samples must be taken into account. Since we cannot separate "feed-down" charmed hadrons from directly-produced hadrons, we also have to account for this effect, using the known branching fractions for each source of charmed hadrons. Furthermore, the reconstruction efficiency for events in each electron–charmed-hadron final state depends on the source and must be determined for each decay chain into the given final state. We determine these reconstruction efficiencies using Monte Carlo calculations employing a phenomenological

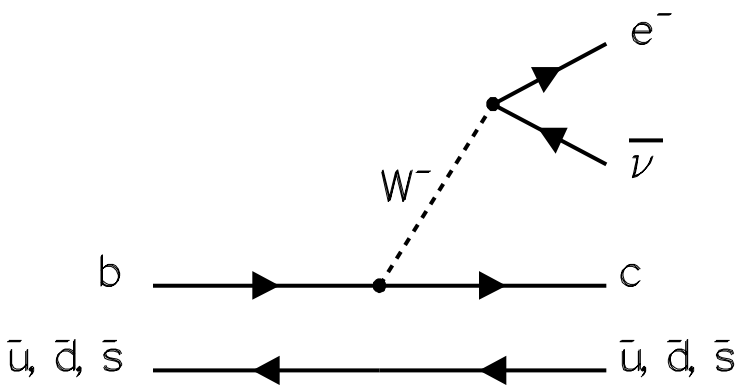

Figure 1.4: The Feynman diagram depicting the semileptonic decay of a $\overline{B}$ meson into an electron and a charmed meson.

model of semileptonic B-hadron decay.

1.3.4 Semileptonic B-Hadron Decay

Semileptonic decays of B hadrons [55], i.e.,

$$\overline{B} \to X l^- \overline{\nu}_l, \tag{1.22}$$

offer several advantages for studying the fragmentation properties of bottom quarks. A B hadron decays semileptonically via the weak force. As indicated in the Feynman diagram for semileptonic B-meson decay in Figure 1.4, the virtual $W^\pm$ decay is governed by a purely electroweak interaction. The less well understood QCD processes associated with the strong interaction binding the quarks inside the hadron are treated independently from the virtual $W^\pm$ decay. At typical branching fractions of 10%, the B-hadron semileptonic decay rates are reasonably high. For this reason, large data samples of these decays are available.

The matrix elements for $\overline{B} \to X e^- \overline{\nu}_e$ semileptonic decays are given by the product of the leptonic and hadronic $V - A$ currents [56]:

$$\mathcal{M} = \overline{u}_e \gamma^\mu (1 - \gamma^5) v_\nu \, \langle X | j_\mu | B \rangle \tag{1.23}$$

$$= \overline{u}_e \gamma^\mu (1 - \gamma^5) v_\nu \, \langle X | \gamma_\mu (C_V - C_A \gamma^5) | B \rangle, \tag{1.24}$$

where the first and second terms represent the leptonic and hadronic currents, respectively. The quantities C_V and C_A in the hadronic current are determined by the bound state properties of the initial and final state hadrons. They can be expressed in terms of form factors. For a pseudoscalar B meson decaying into a pseudoscalar meson X and leptons, one finds from Lorentz invariance the form factor decomposition

$$\langle X|j_\mu|B\rangle = f_+(q^2)(P+p)_\mu + f_-(q^2)(P-p)_\mu, \tag{1.25}$$

where q^2 is the four-momentum transfer squared between the B and the X hadrons, and P and p are the four-vectors of the B and X hadrons, respectively. Since $\overline{u}_e\gamma^\mu(1-\gamma^5)v_\nu(P-p)_\mu$ is the charged lepton mass squared, the second term is negligible for semileptonic decays to electrons. Therefore, a single form factor is all that is required to describe pseudoscalar B decays into pseudoscalar D hadrons and electrons. For a pseudoscalar B meson decaying into a vector meson X^* and leptons, three independent form factors are required.

The form factors represent the effects of the strong interaction in the decay. Since perturbative techniques cannot be used to calculate them, several phenomenological models using nonperturbative techniques have been suggested. We use the *Isgur-Scora-Grinstein-Wise* (ISGW) form factor model.

Semileptonic Decay Models

From Figure 1.4, it is clear why the light quark in the semileptonic B-meson decay is called the spectator quark; it can be viewed as simply "coming along for the ride." This motivates the "spectator model," in which the light quark does not participate in the b-quark decay. In this model, the weak decay of a free heavy quark Q into a lighter quark q is represented as

$$Q \;\rightarrow\; qe^-\overline{\nu}_e. \tag{1.26}$$

The decay rate for this process (ignoring radiative corrections) is given by

$$, _{free}(Q \to q e^- \overline{\nu}_e) = \frac{G_F^2 m_Q^5}{192\pi^3} |V_{qQ}|^2 f(m_q/m_Q), \quad (1.27)$$

where

$$f(x) \equiv 1 - 8x^2 + 8x^6 - x^8 - 24x^4 \ln x \quad (1.28)$$

is the phase space factor. In B hadron decays, however, the bottom quark is always confined to a hadron (meson or baryon) and thus is accompanied by either one or two extra quarks. Equation 1.27 holds if and only if the final state evolves independently of the spectator quarks in the hadron and so corrections have to be made to accommodate these strong interaction effects.

The semileptonic branching fractions for the B^+ and B^0 mesons have been measured relatively precisely, but no such measurements exist for the B_s^0 meson or $\overline{\Lambda}_b^0$ baryon. We therefore use the spectator model to estimate these. The spectator model predicts that the inclusive semileptonic decay widths for the various B hadrons are equal, e.g.,

$$, (B_s^0 \to e^+ \nu_e X) = , (B \to e^+ \nu_e X), \quad (1.29)$$

where the right hand side is independent of B meson flavour. These widths are related to the branching fractions by the lifetimes of the B hadrons, so that

$$\mathcal{B}(B_s^0 \to e^+ \nu_e X) = \frac{\tau(B_s^0)}{\langle \tau(B) \rangle} \mathcal{B}(B \to e^+ \nu_e X), \quad (1.30)$$

where B refers to the same admixture of B^+ and B^0 mesons as used to determine the mean B meson lifetime, $\langle \tau(B) \rangle$. A similar relationship is obtained for the $\overline{\Lambda}_b^0$ baryon semileptonic decay width.

From the spectator model, we also expect the exclusive partial widths to be equal, e.g.,

$$, (B^+ \to \overline{D}^0 e^+ \nu_e) = , (B^0 \to D^- e^+ \nu_e) = , (B_s^0 \to D_s^- e^+ \nu_e). \quad (1.31)$$

We can therefore calculate the branching fractions for the exclusive B_s^0 semileptonic decays.

N. Isgur, D. Scora, B. Grinstein and M. Wise note that the semileptonic B-meson decay rate is known experimentally to be dominated by decays to two exclusive final states, $Dl^-\overline{\nu}_l$ and $D^*l^-\overline{\nu}_l$ [57, 58]. The ISGW form factor model, therefore, determines the form factors describing the B meson decay from an explicit summation of the spectra of contributing hadronic resonances in semileptonic B decays (i.e., $\overline{B} \to (D, D^*, D^{**})l^-\overline{\nu}_l$). For the calculation, the nonrelativistic quark potential model [59] is used, a phenomenological approach to QCD in the nonperturbative regime. These authors have expressed the form factors of the hadronic current in terms of bound state wave functions. For these, they use Schrödinger wave functions representing the motion of a valence quark in a Coulomb plus linear potential.

There are no adjustable parameters in the ISGW model. A comparison of its prediction for the inclusive lepton energy spectrum to the spectrum observed in $\Upsilon(4S)$ decays by the CLEO experiment [60] showed that the ISGW model predicts a much smaller D^{**} contribution to the semileptonic width than is indicated by the data. By increasing the D^{**} contribution in the ISGW model, CLEO was able to find a good fit to the data except for the lepton energy endpoint region.

1.4 Dissertation Overview

We have motivated the measurement of b-quark fragmentation fractions in $\overline{p}p$ collisions and have described several of the existing phenomenological models of heavy quark fragmentation and semileptonic B-hadron decay. The remainder of this dissertation will describe the measurement itself.

The experimental apparatus used to perform the measurement is described in Chapter 2. In Chapter 3, the electron identification criteria are explained. Chapter 4 discusses the techniques used to reconstruct charmed hadrons. The charmed hadron signal distributions are presented and the event yields are provided. In Chapter 5, the Monte Carlo methods used to calculate the reconstruction efficiencies are outlined.

Chapter 6 explains the method used to yield the ratios of fragmentation fractions. A calculation of the absolute fragmentation fractions and the associated uncertainties is presented. Finally, conclusions are presented and discussed in Chapter 7.

Chapter 2

Experimental Apparatus

The experiment discussed in this thesis was performed at the Tevatron Collider at the Fermi National Accelerator Laboratory (FNAL). Fermilab, as it is commonly called, is situated in Batavia, Illinois, USA. The data used for this study were recorded during the Tevatron Run 1, in the years 1992 through 1995. Run 1 comprises two separate data-taking periods: Run 1A and Run 1B. Run 1A commenced on August 26, 1992 and ended on May 30, 1993. Run 1B ran from January 18, 1994 to July 24, 1995. The time-integrated luminosities of Run 1A and Run 1B are (19.5 ± 1.0) pb^{-1} and (89 ± 4) pb^{-1}, respectively.

2.1 The Fermilab Tevatron $\overline{p}p$ Collider

The Fermilab Tevatron Collider, shown schematically in Figure 2.1, is a circular proton-antiproton collider 6.3 km in circumference. The centre-of-mass energy, $\sqrt{s}$, of the $\overline{p}p$ collisions is 1.8 TeV. There are several processes required to generate such high energy $\overline{p}p$ collisions. First, H^- ions are produced from gaseous hydrogen and then subjected to a 750-keV electrostatic potential. The H^- ions are then accelerated to 400 MeV by a linear accelerator called the Linac and passed through a carbon foil, where the electrons are stripped off. The resulting protons are injected into a circular alternating gradient synchrotron called the Booster. The Booster accelerates the protons to 8 GeV, after which they are transferred to the Main Ring synchrotron.

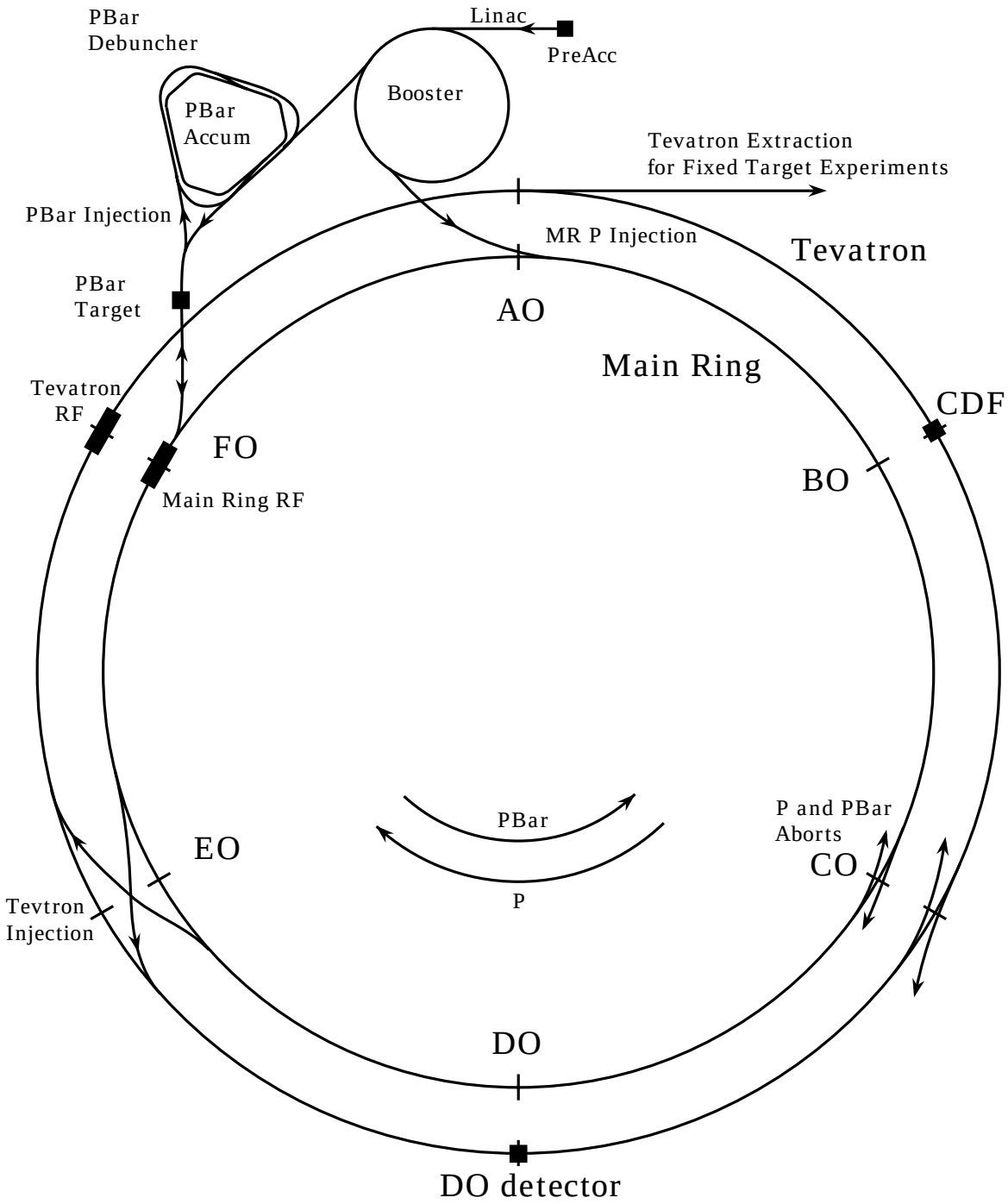

Figure 2.1: The Fermilab Tevatron $\overline{p}p$ Collider. The various elements are not drawn to scale.

In the Main Ring, the protons are accelerated to approximately 120 GeV, at which point a fraction of them are extracted from the Main Ring and aimed at a nickel target. Collisions with the target produce antiprotons, which are selected and injected into a storage ring called the Debuncher, where they undergo stochastic cooling [61, 62, 63], a process by which their transverse momentum distribution is reduced. They are then stored in the Accumulator ring, a second storage ring concentric to the Debuncher. When enough antiprotons are stored (approximately 10^{11}) they are injected into the Main Ring and accelerated to 150 GeV.

Once the protons and antiprotons in the Main Ring reach energies of 150 GeV, six 30-cm long bunches of protons and six similar bunches of antiprotons are injected into the Tevatron. The protons and antiprotons travel in opposite directions in the high magnetic fields produced by the Tevatron's superconducting dipole magnets and are simultaneously accelerated to 900 GeV. When the beams reach this energy, they are focussed to a transverse cross section with a radius of 35 μm and aligned to intersect at the interaction point near the centre of the CDF detector. This interaction point, BØ, is one of the six places in the Tevatron where collisions can occur. The time between proton and antiproton bunch crossings at BØ is 3.5 μs.

2.2 The Collider Detector at Fermilab

The Collider Detector at Fermilab (CDF) [64] is a 5000-ton multipurpose detector capable of identifying many different kinds of particles produced in high energy $\overline{p}p$ collisions. The detector, shown in Figure 2.2, is composed of several specialized devices, each designed to identify a certain class of particle or to measure to high precision a specific property of those particles. Its capabilities include charged particle tracking, high resolution momentum measurement and finely segmented electromagnetic and hadronic calorimetry. Figure 2.3 shows the placement of each detector component.

CDF is a cylindrical detector, axially surrounding the Tevatron beampipe. The cartesian coordinate system used by CDF is such that the x and y axes lie in the plane perpendicular to the beamline and the z axis lies along the proton beam direction.

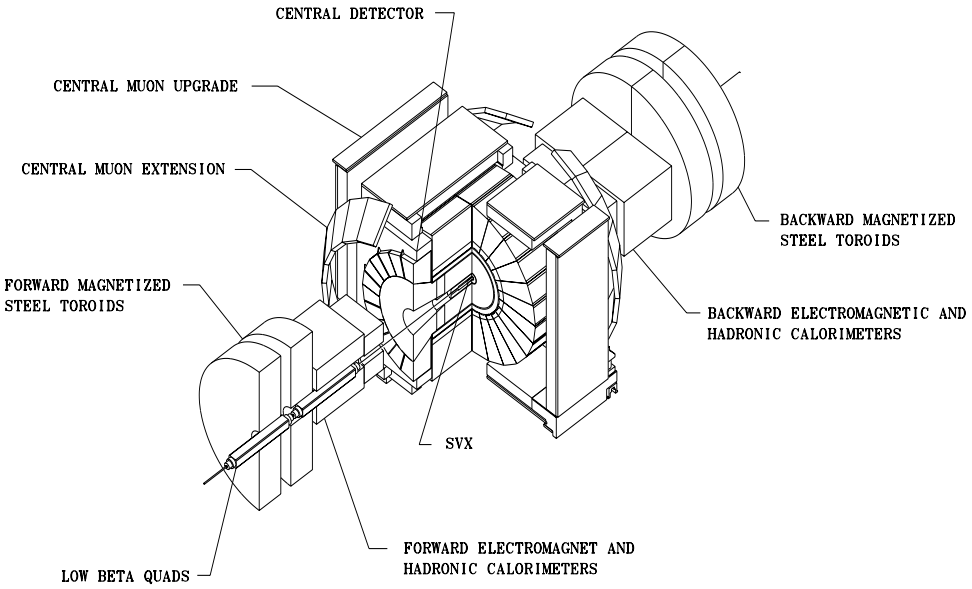

Figure 2.2: An isometric view of the Collider Detector at Fermilab with one quadrant cut away.

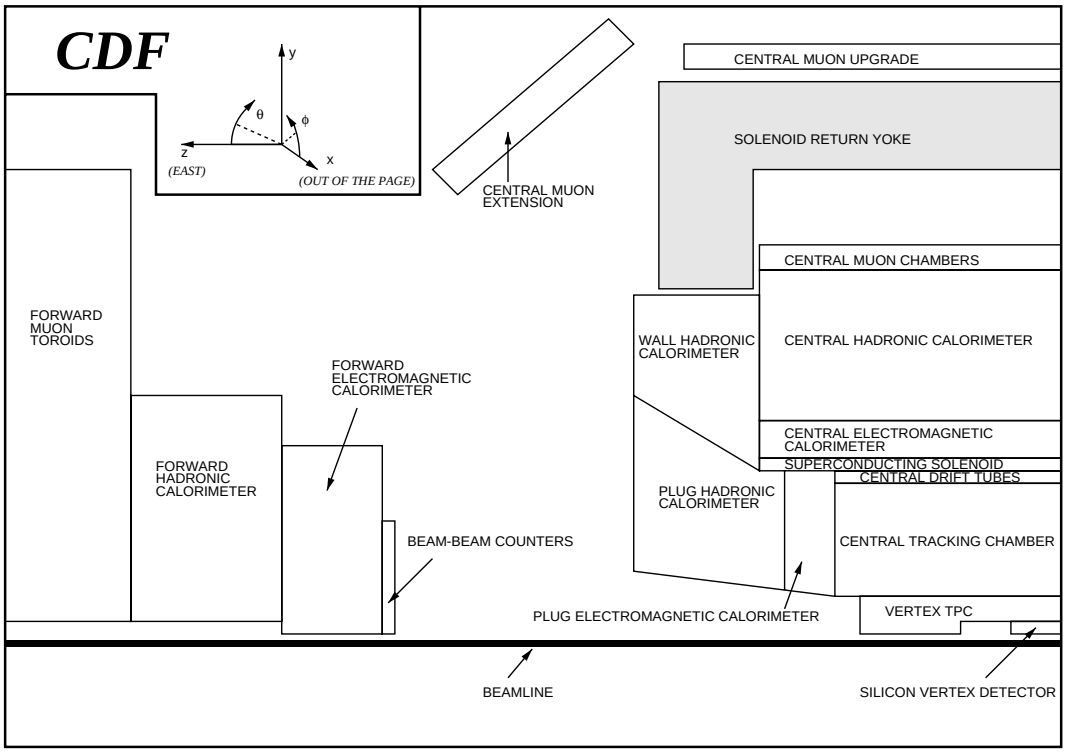

Figure 2.3: A schematic side-view of one quadrant of the Collider Detector at Fermilab.

The polar angle θ is measured from the proton beam axis and the azimuthal angle ϕ is determined with respect to the plane of the Tevatron. Pseudorapidity is a unit often used by CDF; it is defined as $\eta \equiv -\ln(\tan(\theta/2))$.

The central detector ($|\eta| < 1.1$) consists of both tracking and calorimeter subsystems. The tracking is provided by the silicon vertex detector (SVX), the vertex drift chamber (VTX), and the central tracking chamber (CTC), all enclosed within a 1.41-Tesla solenoidal superconducting magnet. Electromagnetic calorimeters, hadronic calorimeters and muon detectors lie outside the magnet. The entire structure lies inside a steel yoke that supports the superconducting coil and acts as the magnet flux return.

Neither the CDF plug calorimeters that cover the regions $1.1 < |\eta| < 2.4$, the forward/backward calorimeters that cover $2.4 < |\eta| < 4.2$, nor any of the muon detectors are used in the analysis described in this thesis and so will not be discussed further here. The detector components relevant to this analysis are described in more detail below.

2.2.1 Tracking Detectors

The CDF tracking system comprises three detectors: the silicon vertex detector, the vertex drift chambers and the central tracking chamber.

Silicon Microstrip Vertex Detector

A 51-cm long cylindrical silicon microstrip vertex detector [27] surrounds the 1.9-cm radius beryllium beampipe. The SVX was designed to allow for the precise extrapolation in the $r - \phi$ plane of tracks into the uninstrumented region of the beampipe, enabling one to identify vertices of non-prompt tracks from secondary decays[1].

The SVX, shown in Figure 2.4, is constructed of four concentric layers of silicon microstrip detectors, located at radii of 3.0, 4.2, 5.7 and 7.9 cm from the beamline. Each layer is segmented into twelve axial "ladders", each subtending 30° in azimuth.

[1]We refer to tracks that originate from the proton-antiproton interaction point as prompt tracks.

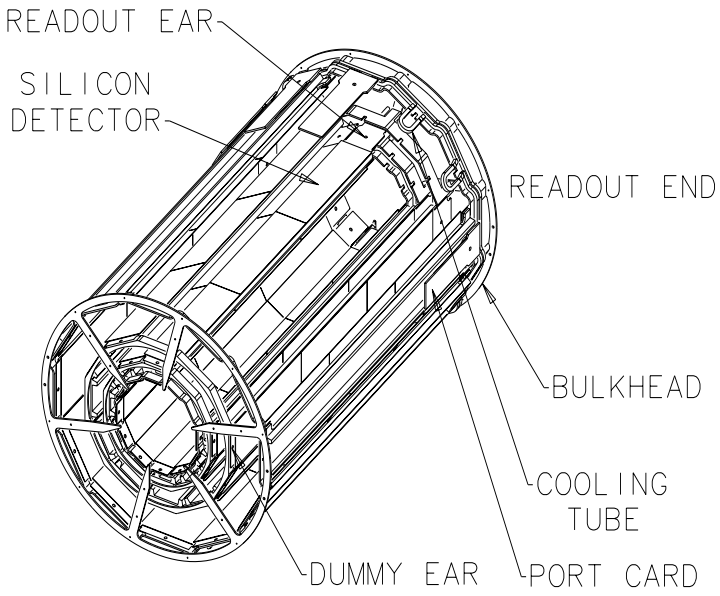

Figure 2.4: An isometric view of an SVX barrel. One barrel lies on either side of the $z = 0$ position inside the CDF detector.

Six 8.5-cm long silicon microstrip sensors are mounted on each ladder module, with each sensor consisting of a 300-μm thick silicon crystal. When a charged particle passes through a silicon microstrip detector, it ionizes the silicon atoms and the drift of the resulting electrons produces a detectable signal. These electronic signals are picked up by copper strips on the surface of the sensors. The silicon strip separation is 60 μm for the inner three layers and 55 μm for the outer layer, resulting in a 13 μm transverse spatial resolution.

The length of the Tevatron bunch produces $\overline{p}p$ interactions that have a Gaussian distribution in the z direction with an RMS width of ~ 30 cm, so the proton-antiproton interaction region has a length of over 60 cm, distributed around the $z = 0$ position in the CDF detector. Since the SVX only encloses 51 cm of the interaction region, it has a geometric acceptance of about 60%.

A lower-noise, more radiation-hard version of the SVX, called the SVX$'$ [65], was installed in CDF for the duration of Run 1B. In other respects the SVX$'$ was similar to the SVX, except that the inner layer radius was 2.9 cm rather than 3.0 cm, resulting in a 11.6 μm transverse spatial resolution.

Vertex Drift Chamber

The SVX is enclosed by the vertex drift chamber, a device used to measure the z position of the proton-antiproton interaction (called the primary vertex) and to aid in charged particle detection. The 22-cm radius VTX extends to ± 132 cm in z from the centre of the detector. The VTX comprises 28 drift modules azimuthally segmented into octants. Sense wires oriented tangentially to the beamline in each module allow the measurement of track coordinates in the $r - z$ plane. This information is used to assemble particle tracks into primary vertices. The z resolution for primary vertices is 2 mm. During high instantaneous luminosity running periods, several $\overline{p}p$ interactions can occur during a single bunch crossing.

Central Tracking Chamber

Outside the VTX lies the central tracking chamber [66], a cylindrical drift chamber with an inner radius of 0.28 m, an outer radius of 1.38 m and a length of 3.20 m. The CTC provides precise momentum determination of charged particles through the measurement of the track curvature in the 1.41-Tesla magnetic field. The chamber volume is filled with an argon-ethane-alcohol gas mixture that is subjected to an electric field provided by sets of field-shaping wires strung through the chamber. When a high momentum charged particle passes through the chamber, it ionizes the gas molecules and the liberated electrons travel under the influence of the electric field toward sense wires. The drift time of these ionization electrons is used to measure the spatial position of the ionizing particle. The large number of sense wires in the chamber (6 156 in total) allow for the precise reconstruction of the track associated with the passage of the charged particle through the chamber.

The CTC sense wires are arranged in nine "superlayers", five of which contain twelve layers of axial (i.e., parallel to the beamline) sense wires and four of which contain six layers of stereo sense wires tilted $\pm 3^\circ$ relative to the beam direction. These superlayers are divided into drift cells such that the maximum drift distance in any cell is less than 40 mm (corresponding to a maximum drift time of about

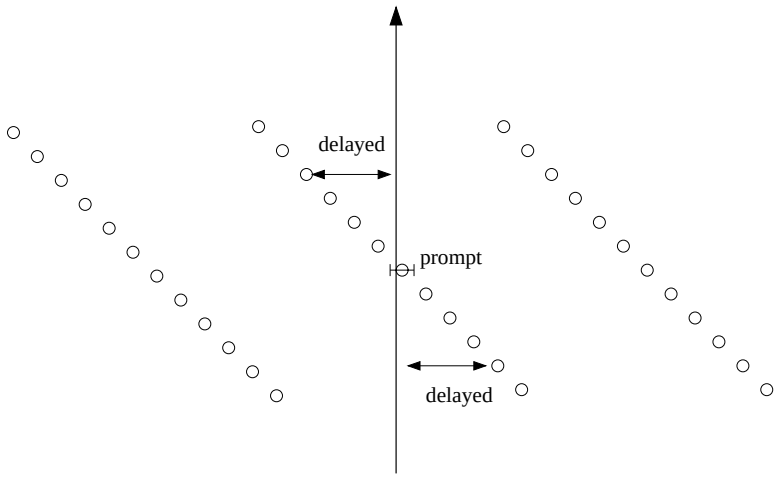

Figure 2.5: Schematic of three axial-layer drift cells. The circles represent the sense wires in the cells. The 45° tilt of the cells with respect to the radial direction is visible. The vertical arrow represents a stiff track passing through the cells. The sense wire closest to the track registers a "prompt" hit. The wires further away from the track register "delayed" hits due to the drift time of the ionization electrons. The patterns of prompt and delayed hits are used in the Level 2 CFT trigger to perform rapid pattern recognition.

800 ns). Figure 2.5 shows three axial layer cells. The axial layer cells allow for pattern recognition in the $r-\phi$ view. The stereo cells provide $r-z$ tracking information. Both types of cells are tilted 45° with respect to the radial direction from the beamline so that the drift trajectories are approximately azimuthal when the $E \times B$ electrostatic force is taken into account.

Figure 2.6 shows a drawing of one end plate of the CTC. The nine superlayers are visible as is the 45° tilt of the cells. The spatial resolution in the transverse plane is between 125 and 200 μm, depending on the location in the chamber, and is 1 mm in the z direction. The momentum resolution of the CTC when operating in a 1.41-T magnetic field is

$$\delta P_T/P_T^2 < 0.002\ (\mathrm{GeV/c})^{-1}, \tag{2.1}$$

where $P_T = P \sin\theta$ is the transverse momentum. The momentum resolution of the combined SVX-CTC system is

$$\delta P_T/P_T = \left[(0.0009 P_T)^2 + (0.0066)^2\right]^{1/2}, \tag{2.2}$$

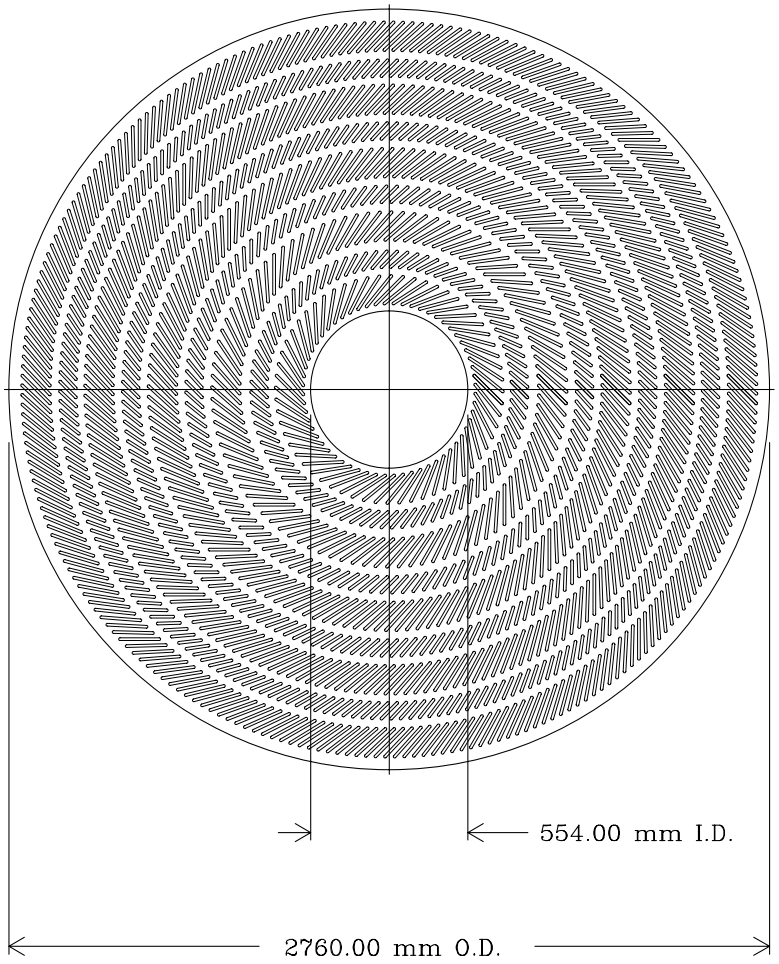

Figure 2.6: Schematic of one end plate of the CTC showing the slots for the rows of sense wires in each super cell.

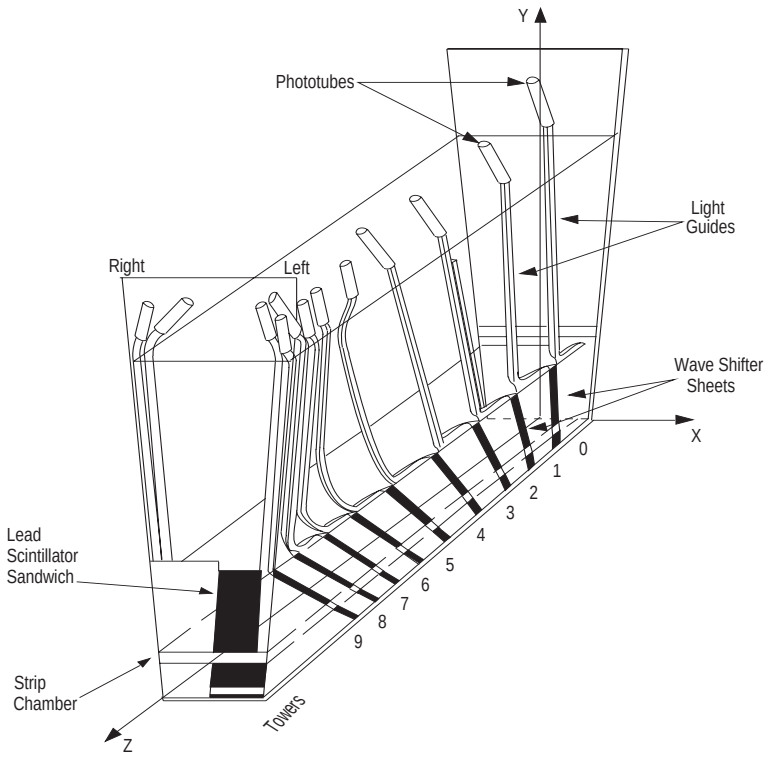

Figure 2.7: Schematic of a central electromagnetic calorimeter module.

where P_T is in units of GeV/c.

2.2.2 Calorimeters

The CDF central calorimeter ($|\eta| < 1.1$) [67] is composed of an electromagnetic calorimeter (CEM) placed just outside the solenoid and a hadronic calorimeter placed outside the CEM. Both calorimeters are constructed from 48 wedge-shaped modules, each subtending 15° in ϕ. Each 2.5-m long wedge is divided into ten projective towers of width 0.1 in pseudorapidity that point at the interaction region.

Central Electromagnetic Calorimeter

Each CEM module is constructed of thirty passive layers of 3.2-mm lead sheets sandwiched between thirty-one active layers of 5-mm thick polystyrene scintillator. The layers are stacked on an aluminum base plate and assembled into ten projective towers, as shown in Figure 2.7. The lead sheets are clad in 0.38-mm aluminum plate.

The scintillator pieces are wrapped in two layers of 0.038-mm vellum drawing paper.

The radiation length of material in the CEM presented to a particle produced at $z = 0$ as a function of polar angle is made approximately constant by substituting increasing amounts of acrylic for lead in specific layers of towers as a function of η. The total depth of the CEM is 34.5 cm, corresponding to eighteen radiation lengths or one hadronic interaction length. Three-millimeter thick acrylic wavelength shifters affixed to the sides of each tower collect the scintillator light, which then propagates to phototubes via light guides.

The average energy resolution, $\sigma(E)/E$, of the CEM is $13.7\%/\sqrt{E_T} \oplus 2\%$, where $E_T = E \sin\theta$ is the energy transverse to the beamline in units of GeV and $\oplus$ signifies that the constant term is added in quadrature.

Central Electromagnetic Strip Chamber

The central electromagnetic strip chamber detector (CES) [68] is used to identify the position and transverse development of electromagnetic showers near shower maximum in the CEM. For this reason, it is placed between the eighth lead layer and the ninth scintillator layer of the CEM, a depth corresponding to about 5.9 radiation lengths (refer to Figure 2.7). The shower position and transverse development are measured by proportional wire chambers with orthogonal cathode strips and anode wires, as shown in Figure 2.8.

A CES module is composed of an aluminum base with ribs that both define the sides of the 64 cells and support the strips. A gold-plated tungsten wire is centred in each cell and runs the length of the chamber. The wires are cleaved in the longitudinal centre of the chamber, providing independent signals for read-out at both ends. Neighbouring wires are read out in pairs for a total of 64 read-out channels.

Electromagnetic shower profiles are largely confined to a few channels, with 93% of the pulse height contained in three channels in the wire view and 87% contained in three channels in the strip view. The pulse height sharing in the three channels is used to determine the shower position. The CES has a position resolution of

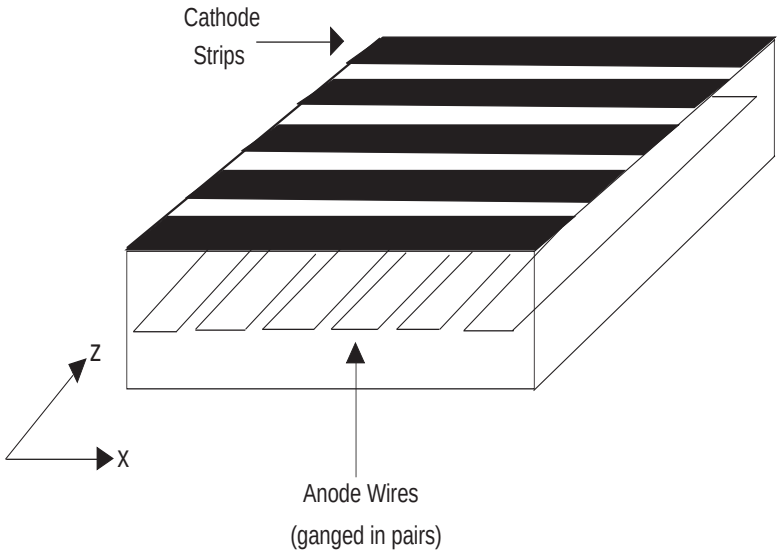

Figure 2.8: Schematic of the cross section of a CES strip chamber module (not to scale). The widths of the strips are either 1.67 cm for the 69 strips nearest $\eta = 0$ or 2.01 cm for the remaining 59 strips. The wire separation is 0.61 cm.

2 mm for 50 GeV/c electrons. The energy resolution for electrons above 20 GeV/c is 25%. These resolutions degrade somewhat for lower energy showers, due to the larger fluctuations in the shower development.

Central Hadronic Calorimeter

The central hadronic calorimeter [69] comprises 48 central modules ($|\eta| < 0.9$) and 48 endwall modules ($0.7 < |\eta| < 1.3$). The central modules (CHA) are located in the wedges and the endwall modules (WHA) are attached to the solenoid yoke. The term "CHA" refers to both the CHA and the WHA throughout the rest of this thesis. Thirty alternating layers of plastic scintillator sheets and steel plates (fifteen for the endwall modules) are constructed in a tower geometry, similar to that of the CEM. A central module contains nine towers and its corresponding endwall module contains six towers. Three towers are shared in the interface between the CHA and WHA. The total depth of the CHA is about 4.5 hadronic interaction lengths.

2.2.3 The Trigger Systems

CDF uses a three-level trigger system [64, 70] to select the small fraction of interesting physics events from the large number of $\overline{p}p$ interactions produced by the Tevatron. With a $\overline{p}p$ inelastic cross section of 50 mb at $\sqrt{s} = 1.8$ TeV [71][2] and a typical instantaneous luminosity of $\mathcal{L} = 10^{31}$ cm^{-2}s^{-1}, the interaction rate is about 500 kHz. The trigger system identifies and filters the interesting events, thereby reducing this rate to less than 10 Hz, the rate at which the data can be effectively processed by the offline reconstruction systems. The trigger decision and the data acquisition process require time during which the CDF detector is not capable of considering subsequent $\overline{p}p$ interactions. The trigger system is designed to keep this "dead-time" fraction to at most 10%. A general description of this trigger system is provided below. A more detailed description of the electron trigger is given in Section 3.2.

Level 1

The Level 1 trigger is composed of FASTBUS-based electronics, which process the analog output of the photomultiplier tubes instrumenting the electromagnetic and hadronic calorimeters. This information is summed into towers of $(\Delta\eta = 0.2) \times (\Delta\phi = 15^\circ)$. Note that two CEM towers of $\Delta\eta = 0.1$ are combined into a single "trigger tower." The triggers relevant to the study described in this dissertation require the presence of a single trigger tower containing more than 8 GeV of electromagnetic energy at Level 1.

Events satisfying a reduced electromagnetic energy threshold of 4 GeV are accepted at a rate of one in twenty or forty, during Run 1A and Run 1B, respectively. Such interesting yet highly probable events would saturate the data acquisition throughput, thereby reducing the yield of rarer processes due to an increase in dead-time. The application of an acceptance rate factor, called a "prescale", allows experimenters to record only a given fraction of these common events for further study.

[2]The total $\overline{p}p$ cross section including diffractive interactions is 80 mb.

The Level 1 trigger also accepts events in which one or two muon candidates satisfying specific transverse momentum requirements are detected in the muon identification system. The average Level 1 acceptance rate was approximately 1 kHz.

The Level 1 trigger decision is available in less than 3.5 μs, the time between beam crossings. When a positive Level 1 decision occurs, the Level 2 trigger is allowed 20 μs to choose whether to accept or reject the event. During this time, the five subsequent beam crossings are ignored.

Level 2

The Level 2 trigger, also implemented on FASTBUS cards, combines tracking information with more detailed calorimeter information.

A hardware calorimeter cluster finder looks for clusters of transverse energy in neighbouring electromagnetic and hadronic calorimeter towers that fulfill "seed" and "shoulder" threshold requirements. An electromagnetic cluster is formed when a trigger tower contains sufficient electromagnetic energy to satisfy the seed threshold. Adjacent trigger towers with transverse EM energy exceeding the shoulder threshold are then included in the cluster. Electromagnetic calorimeter clusters are differentiated from hadronic clusters by requiring that the hadronic energy fraction in the two primary trigger towers not exceed 12.5%.

The Central Fast Tracker (CFT) is a hardware track processor that uses crude timing information from the five axial layers of the CTC. Wires with hits occuring within 80 ns after the beam crossing (i.e., prompt hits) are situated close to the particle trajectory whereas wires with hits occuring 500-650 ns later (delayed hits) are situated further away from the track (refer to Figure 2.5). The CFT uses this information to reconstruct the particle trajectory. The track is then matched to patterns in a look-up table to identify which one of eight P_T ranges the track should be assigned to. The CFT momentum resolution is $\delta P_T \approx 0.035 \times P_T$.

Clusters of electromagnetic energy with $E_T > 5$ GeV are spatially matched to CFT tracks to form electron candidates. More stringent requirements on the E_T and P_T quantities are applied to certain trigger streams. Hits in the muon chambers are

spatially matched to CFT tracks to form muon candidates.

An additional hardware trigger was available at Level 2 in Run 1B. The XCES shower-maximum trigger uses information in the CES to locate the CEM cluster position in the cluster seed tower. The XCES then identifies showers with a CFT track spatially matched to the CES cluster position.

The average Level 2 acceptance rate was about 12 Hz, including the inclusive electron trigger as well as triggers from other sources.

Level 3

Events passing the Level 2 trigger are processed in more detail at Level 3 [72]. Several events are analyzed in parallel using a farm of 64 commercial Silicon Graphics processors[3]. The Level 3 trigger reduced the Level 2 rate by a factor between two and three.

Sophisticated FORTRAN software algorithms essentially identical to those used in the subsequent offline analysis are used to reconstruct the digitized data. Most of the processing time at Level 3 is spent on three-dimensional track reconstruction in the CTC. The Level 3 inclusive electron trigger requires the shower profile information in the CEM and the CES to be consistent with that of an electromagnetic shower, as described in Chapter 3. A match requirement between a reconstructed CTC track and the CES cluster is also imposed. At Level 3 the muon candidate reconstruction is refined and a match between the muon chamber hits and a CTC track is required.

[3]Only 48 processors were available during Run 1A.

Chapter 3

Electron Identification

The most readily identifiable product of semileptonic B-hadron decays at CDF is the lepton. High energy leptons (i.e., electrons and muons) leave distinctive signatures in the detector such that they can be efficiently selected by the trigger. By imposing more stringent criteria to those events, a relatively pure sample of lepton candidates associated with B-hadron decays can be obtained. The hadronic decay products from the semileptonic B-hadron decay are then identified, as discussed in Chapter 4.

In this thesis, we consider only semileptonic decays to electrons. An analysis of the muon channel was well beyond the scope of this study, and semileptonic B decays to τ leptons are not readily identifiable by the CDF detector.

3.1 Electron Properties

We select the electron identification criteria for our measurement to ensure that the majority of the electron candidates in the final data sample are well measured and are likely to be products of semileptonic B-hadron decays. At the same time, we attempt to maintain a high efficiency (better than 50%) for real electrons to maximize the statistical power of our measurement.

A bottom hadron produced in a $\overline{p}p$ collision is embedded within the cluster of particles resulting from the fragmentation process. Furthermore, a B hadron that decays into a high-energy electron is boosted in the lab frame such that the corresponding

charmed hadron is produced in the vicinity of the electron. The electron from the B hadron semileptonic decay is, therefore, not well isolated from other particles. However, the electron identification criteria impose implicit isolation requirements on the electron candidates.

High-energy electrons arise from sources other than B-hadron decay. Photon conversions and $W^{\pm}$ and Z^0 boson decays are three such sources. Electron candidates likely to be associated with these sources are removed from the B-hadron decay electron sample. The efficiency for removal, however, is less than 100%, therefore, there are residual electron candidates from these sources in the final sample.

We take advantage of the characteristic signatures discussed below that indicate the presence of electrons in the CDF detector. We therefore use a set of criteria to define a sample of electron candidates. The resulting electron candidate sample contains backgrounds from various sources, including residual photon conversions and pion-photon overlaps. We estimate that the B-hadron decay electron candidate sample consists of about 70% real electrons [73].

3.1.1 Fiducial Requirements

We use only electron candidates in the central detector ($|\eta| < 1.1$), where the charged particle reconstruction is excellent and the electron identification scheme is best understood. Furthermore, we impose the additional fiducial constraint that the electron track not enter cracks (i.e., uninstrumented regions) or poorly-understood regions of the central detector. Overall, approximately 88% of the solid angle in the central detector lies within this fiducial region.

3.1.2 Electromagnetic Energy

High energy electrons deposit most of their energy in the electromagnetic calorimeter. The CEM is designed such that an electromagnetic shower does not propagate across the ϕ boundaries between wedges. Since electromagnetic showers are generally only a few centimeters in diameter, they are usually well contained within a single calorime-

ter tower[1], unlike hadronic showers, which tend to span several towers. Therefore, the primary signature of an electron is a large deposit of energy in a single electromagnetic calorimeter tower where the lateral leakage (i.e., the energy deposited in the neighbouring electromagnetic calorimeter towers) is comparatively small. We require that the transverse energy E_T in the electromagnetic cluster be $E_T > 8.0$ GeV.

3.1.3 Lateral Shower Profile

The pattern of energy sharing, or leakage, between towers adjacent in η, called the lateral shower profile, is used to separate real electrons from candidates arising from an accidental overlap between a charged pion and a neutral hadron that showers electromagnetically (e.g., $\pi^0 \rightarrow \gamma\gamma$). The lateral shower profile for a cluster of electromagnetic energy is required to be consistent with that measured using 50 GeV/c electron test beam data [74]. This agreement is quantified by the variable L_{shr}, defined as

$$L_{shr} = 0.14 \sum_{k=1}^{3} \frac{M_k - P_k}{\sqrt{0.14^2 E_T + (\Delta P_k)^2}}, \tag{3.1}$$

where E_T is the electromagnetic energy in the cluster of three neighbouring towers k, M_k is the measured energy in the tower k and P_k is the predicted energy in the tower, determined by using the z component of the CES shower position and the z position of the primary vertex. The quantity $0.14\sqrt{E_T}$ represents the resolution in E_T and ΔP_k represents the resolution in P_k. We require $L_{shr} < 0.2$.

3.1.4 Hadronic Energy Fraction

In contrast to electrons and photons, which deposit most of their energy in the electromagnetic calorimeter, hadrons typically deposit a small amount of their energy in the electromagnetic calorimeter and deposit the remaining energy in the hadronic calorimeter. Therefore, electromagnetic showers can be differentiated from hadronic showers by requiring that the longitudinal leakage (i.e., the fraction of cluster en-

[1]This is not the case when the electron lands near the boundary in η between two towers.

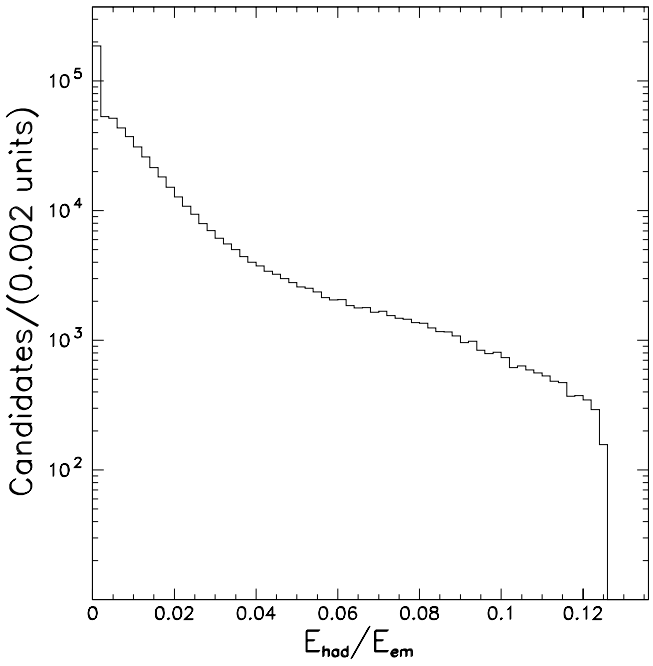

Figure 3.1: E_{had}/E_{em} distribution for electron candidates. The trigger requirement, $E_{had}/E_{em} < 0.125$, is evident.

ergy deposited in the hadronic calorimeter) in an electromagnetic cluster is low. The hadronic energy fraction, E_{had}/E_{em}, for electron candidates is shown in Figure 3.1. The trigger requirement, $E_{had}/E_{em} < 0.125$ in a single trigger tower, is evidenced by the cut-off at this value. To further improve the purity of the electron sample, we require that E_{had}/E_{em} in the seed tower and two neighbouring towers be less than 4%.

3.1.5 High-P_T Charged Track

Since an electron usually leaves a track in the CTC, we require the presence of a CTC track pointing to the calorimeter energy cluster. This criterion rejects most of the EM clusters produced by high energy photons. To ensure that the efficiency of the E_{had}/E_{em} requirement is independent of other charged particles in proximity to the electromagnetic clusters, we require that only one track be pointing at the towers in which the electromagnetic energy is deposited. The requirement that the track

be spatially matched in x and z to the EM cluster position as determined by the CES further reduces backgrounds from random track-shower overlaps. We require $|z_{CES} - z_{CTC}| < 3.0$ cm, where z_{CES} is the position of the electromagnetic cluster as measured by the strip chamber and z_{CTC} is the position of the CTC track extrapolated to the radius of the CES. Similarly, we require $|x_{CES} - x_{CTC}| < 1.5$ cm, where x is the position in the strip chamber perpendicular to the z direction.

Since the rest mass of the electron is so small, the associated track will have a transverse momentum consistent with the transverse energy measured in the electromagnetic calorimeter. We do not explicitly impose a minimum P_T requirement on the track associated with the electron but we require that the ratio of transverse energy to transverse momentum, E_T/P_T, be in the range $0.75 < E_T/P_T < 1.40$.

3.1.6 Strip and Wire Chamber Profiles

The transverse shower profiles in the x and z directions (refer to Figures 2.7 and 2.8) typically created by an electron were measured for the wire and strip chamber signals, respectively, using 50 GeV/c electron test beam data [74]. The wire and strip chamber profiles for clusters of electromagnetic energy are required to be consistent with those measured using the test beam data. Either eleven wires or strips are examined in the vicinity of each cluster. The χ^2 describing the comparison between the measured strip profile and that determined using the test beam data is required to be less than 10.0. Similarly, the χ^2 for the wire profile is required to be less than 15.0[2]. The number of degrees of freedom for the fit depends on the width of the cluster but can be as large as nine.

3.2 Trigger Criteria

The events used in the study discussed in this dissertation were selected by a three level trigger system, described in Chapter 2. We now describe in more detail the

[2]This value was used for historical reasons. It should be noted that a tighter cut of 10.0 was used in the Run 1 Level 3 trigger.

criteria used to identify electron triggers. Events fulfilling the calorimeter energy requirement at Level 1 were considered at Level 2.

3.2.1 Level 2

The Level 2 inclusive electron trigger is an online trigger that takes advantage of some of the properties described in Section 3.1 to identify whether an event is likely to contain an electron.

The Run 1A Level 2 trigger required the presence of a cluster of energy of at least 9 GeV in the electromagnetic calorimeter with at least 9 GeV in the seed tower. Any neighbouring towers with at least 7 GeV of electromagnetic energy were included in the cluster. A CFT track with a transverse momentum of at least 9.2 GeV/c pointing at the same ϕ wedge containing the electromagnetic calorimeter cluster was also required. The hadronic energy in the cluster was required to be less than 12.5% of the electromagnetic component.

The Run 1B Level 2 trigger required the presence of a cluster of energy of at least 8 GeV in the electromagnetic calorimeter with at least 8 GeV in the seed tower. Any neighbouring towers with at least 7 GeV of electromagnetic energy were included in the cluster. A CFT track with a transverse momentum of at least 7.5 GeV/c pointing at the same ϕ wedge containing the electromagnetic calorimeter cluster was also required. The hadronic energy in the cluster was required to be less than 12.5% of the electromagnetic component.

The XCES shower-maximum trigger, implemented in Run 1B, required a match between the CFT track and the CES cluster position to within ± 2.5 cm. The XCES trigger reduced the Level 2 trigger rate by a factor of two while being 90% efficient for real electrons [75], thereby allowing the reduction in the E_T threshold from 9 GeV to 8 GeV.

The Level 2 inclusive electron trigger was dynamically prescaled as a function of instantaneous luminosity during the high instantaneous luminosity data-taking late in Run 1B.

$E_T >$	8.0 GeV
$P_T >$	6.0 GeV/c
$L_{shr} <$	0.2
$E_{had}/E_{em} <$	12.5%
$\lvert x_{CES} - x_{CTC} \rvert <$	3.0 cm
$\lvert z_{CES} - z_{CTC} \rvert <$	5.0 cm
χ^2(strip profile) $<$	10.0
χ^2(wire profile) $<$	10.0

Table 3.1: Level 3 inclusive electron trigger requirements.

3.2.2 Level 3

The Level 3 inclusive electron trigger did not require any particular Level 2 trigger as a prerequisite so all events that passed any Level 2 trigger were considered for the Level 3 inclusive electron trigger. More than 80% of the events passing the Level 3 inclusive electron trigger passed the Level 2 requirements described above [76]. The remaining events were accepted by Level 2 triggers with less stringent requirements but with higher prescale factors.

The Level 3 trigger used software reconstruction algorithms similar to those used in the offline reconstruction but imposed less stringent requirements than those presented in Section 3.1. The Level 3 trigger required that at least one electron candidate with the properties presented in Table 3.1 exist in the event.

The L_{shr} and E_{had}/E_{em} requirements were similar to those described in Sections 3.1.3 and 3.1.4, except that only two adjacent towers were considered by the online trigger.

3.3 Non-B Decay Electrons

The criteria described above are sufficient for selecting a sample of well-measured electron candidates. However, some fraction of these are real electrons associated with processes other than semileptonic B-hadron decay. We discuss three of the largest sources of these candidates and the criteria used to veto them.

3.3.1 Photon Conversions

Photon conversion electrons comprise approximately 30% [77, 78] of the electron candidates fulfilling the selection criteria described above. The electron selection criteria fail to reject photon conversions because they are in fact real electrons that are being detected. Fortunately, photon conversions in the CDF detector can be identified with two independent techniques.

The first technique requires the presence of a partner track within $\pm 90^\circ$ in ϕ and with a charge opposite to that of the high-P_T electron candidate. Since the opening angle θ_c of a e^+e^- conversion pair is $\theta_c \approx m_e c^2/E_\gamma$, the partner track is expected to have an opening angle such that $\Delta \cot \theta_c$ is small.

Of the tracks satisfying the above requirements, the track with the minimum θ_c is selected and the circle separation of the two partner tracks in the $r - \phi$ plane at the point at which the two helices are parallel is calculated.[3] The track pair is identified as a photon conversion event if both quantities, $\Delta \cot \theta_c$ and circle separation S, are small. The criteria $S < 0.2$ cm and $\Delta \cot \theta_c < 0.06$ are used for the study described in this thesis.

Photons can convert anywhere in the detector but are most likely to convert in the denser material of the SVX, VTX or inner wall of the CTC. Photons that convert after passing through the VTX do not leave a charged track in the SVX or VTX. The second technique for identifying photon conversions takes advantage of this property. The electron candidate track is extrapolated back to the beamline and the number of hits expected from the track in the VTX is determined. The ratio of the expected number of hits to the actual number of hits, called the "VTX response," or V_{res}, is calculated. When this fraction is below 20%, the electron candidate is classified as coming from a photon conversion.

The radius of conversion, R_c, is defined to be the distance from the beamline to the conversion point (taken to be the midpoint of the line S separating the track circles). Figure 3.2 shows the conversion radius distribution for electrons identified as photon

[3]The circle separation S is defined as $S = D - |\rho_1| - |\rho_2|$, where D is the distance between circle centres and ρ_1 and ρ_2 are the circle radii of curvature.

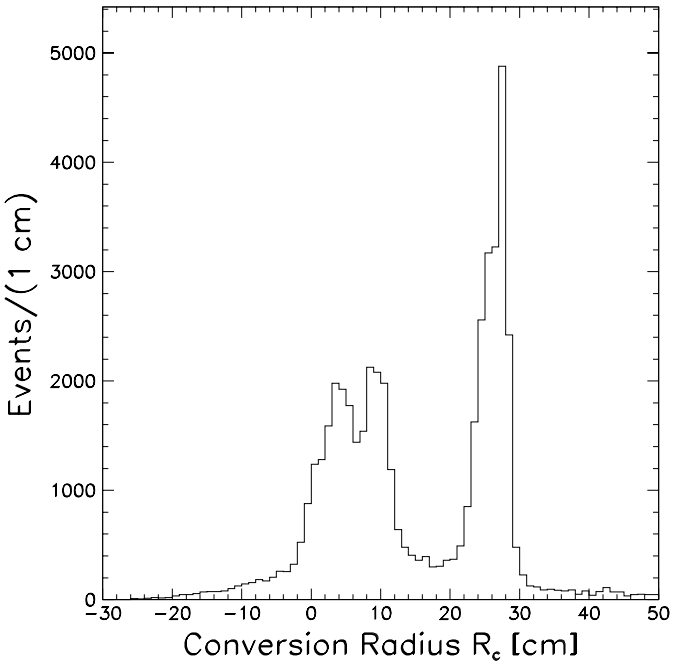

Figure 3.2: Photon conversion radius distribution. The first peak near $R_c = 4$ cm is associated with the SVX, the second peak near 10 cm is due to the VTX inner wall and the peak at 28 cm is due to the inner wall of the CTC.

conversion candidates. From the figure, one can differentiate the regions of high mass density in the CDF detector. Approximately 40% of these photon conversions occur in the CTC inner wall at a radius of approximately 28 cm. This conversion rejection algorithm is 72% efficient at identifying real conversion electrons and reduces the conversion contamination to 11% of the sample [79].

3.3.2 $W^{\pm}$ and Z^0 Boson Decays

Electrons from $W^{\pm}$ and Z^0 boson decays ($W^+ \to e^+\nu_e$ and $Z^0 \to e^+e^-$) also form a significant background to the semileptonic B-decay electron candidates. Figure 3.3 shows a semilogarithmic plot of the P_T distribution of candidate electrons in the inclusive electron sample after the electron selection criteria described above have been applied. The steeply falling P_T spectrum is characteristic of that expected from B-hadron semileptonic decays at Tevatron energies. The shoulder at 30-40 GeV/c results from the presence of characteristically higher P_T electrons from $W^{\pm}$ and Z^0

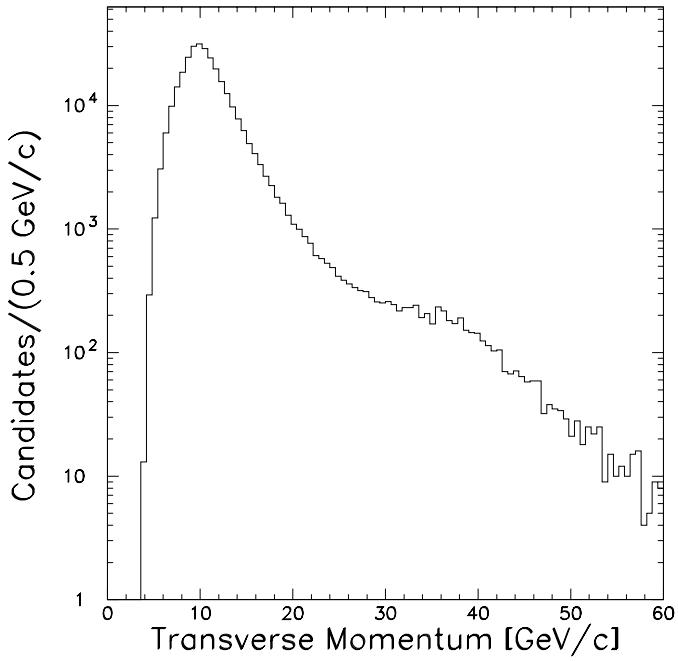

Figure 3.3: Transverse momentum distribution of candidate electrons prior to $W^{\pm}$ and Z^0 boson removal. The shoulder at 30 GeV/c arises from the characteristically higher P_T electrons from $W^{\pm}$ and Z^0 bosons.

boson decays.

Z^0 Boson Removal

Although electrons from Z^0-boson decays do not constitute a large background to the semileptonic B-hadron decay electron sample, it is relatively straightforward to efficiently remove them. For $Z^0 \rightarrow e^+e^-$ events, one or both of the electrons may pass the selection criteria described above. It is possible, however, that the second electron overlaps a jet from the underlying event. In this case, the electron will likely fail the E_{had}/E_{em} cut and possibly the E_T/P_T and L_{shr} requirements. To identify the second electron from Z^0-boson decays, we look for calorimeter energy clusters in the event that contain a large percentage of electromagnetic energy. All clusters (other than the cluster containing the "good" electron) where at least 90% of the cluster energy is electromagnetic in nature are examined. The invariant mass of the electron candidate and the high EM fraction cluster is shown in Figure 3.4. The shoulder above

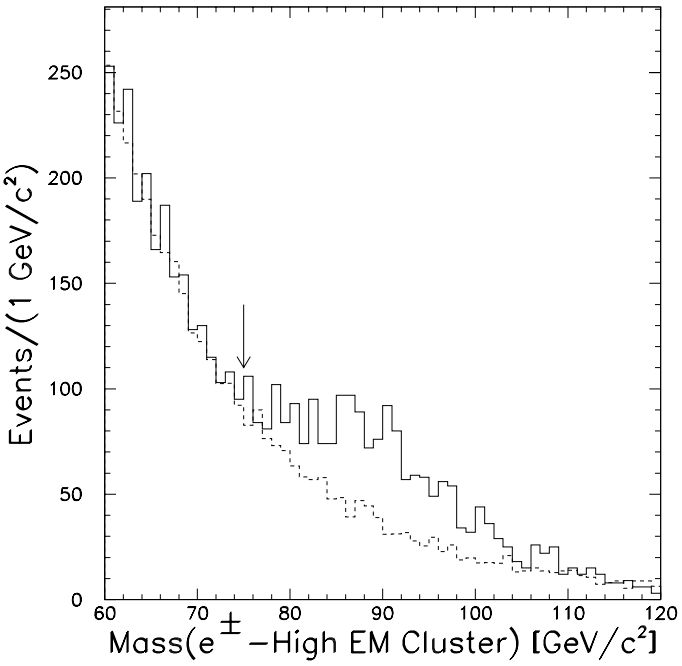

Figure 3.4: Distribution of the invariant mass of the candidate electron and the high EM fraction cluster. The overlaid dashed line shows the scaled distribution for the invariant mass of the candidate electron and low EM fraction clusters. The arrow indicates the value below which B-hadron decay candidates were accepted.

80 GeV/c^2 is due to $Z^0 \to e^+e^-$ decays. The scaled distribution for the invariant mass of the candidate electron and low EM fraction clusters is also shown in the figure for comparison. By subtracting the scaled distribution for low EM fraction clusters from that for high EM fraction clusters, we obtain the background-subtracted distribution in Figure 3.5, which results in a signal peak that agrees well with the Z^0 boson mass of 91 GeV/c^2 [49]. Based on these observations, we reject an event if the invariant mass of the electron and the high EM fraction cluster is greater than 75 GeV/c^2.

W$^\pm$ Boson Removal

The CDF detector cannot detect the neutrino from the two-body $W^+ \to e^+\nu_e$ decay but the transverse component of the neutrino momentum can be inferred from a measurement of the transverse energy imbalance in the calorimeters. This yields the

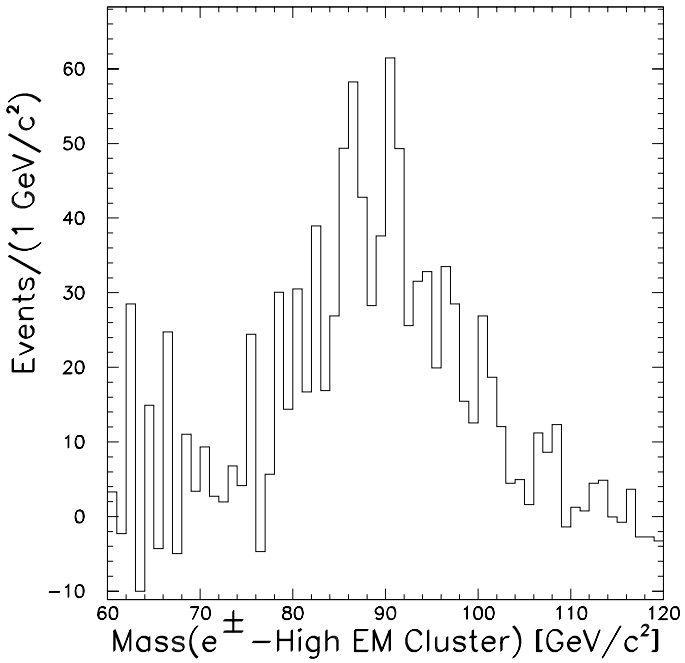

Figure 3.5: Background-subtracted distribution of the invariant mass of the candidate electron and the high EM fraction cluster.

transverse energy of the neutrino $E_T^{\nu} = \not\!\!E_T$, where

$$\not\!\!E_T \equiv |\Sigma \vec{E}_{Ti}| \tag{3.2}$$

is the missing transverse energy and $\vec{E}_{Ti}$ is a vector that points from the interaction vertex to calorimeter tower i and has a magnitude equal to the tower E_T. The sum is over all the towers in the calorimeter with $|\eta| < 3.6$. $W^{\pm}$ bosons can be isolated from the electron sample by looking for events with large missing transverse energy. Figure 3.6 shows the $\not\!\!E_T$ distribution in the inclusive electron sample. The shoulder at high $\not\!\!E_T$ is due to the presence of electrons from $W^{\pm}$ boson decays.

In order to remove $W^{\pm}$ bosons from the inclusive electron sample, we use a variable known as the "missing-E_T significance", $\not\!\!E_T/\sqrt{\Sigma E_T}$, where ΣE_T is the total energy deposited in all the calorimeters for each event. The distribution for $\not\!\!E_T/\sqrt{\Sigma E_T}$ is shown in Figure 3.7. The lower edge of the $W^{\pm}$ boson shoulder is clearly defined. We remove $W^{\pm}$ boson decay electrons by requiring that all candidate electron events

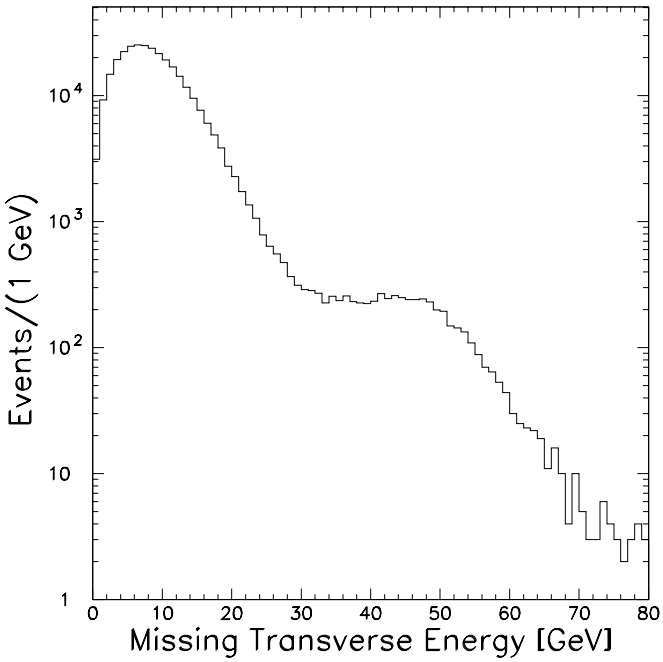

Figure 3.6: Missing transverse energy distribution in candidate electron events. The shoulder at high $\not\!\!E_T$ is due to the presence of electrons from $W^{\pm}$ boson decays.

have $\not\!\!E_T/\sqrt{\Sigma E_T} < 3.5$.

The transverse mass of the electron-neutrino system is given by

$$M_T = \sqrt{(E_T^e + E_T^\nu)^2 - [(E_x^e + E_x^\nu)^2 + (E_y^e + E_y^\nu)^2]},$$

where $E_T^\nu = \not\!\!E_T$ and the z component of the energy is taken to be zero[4]. Figure 3.8 shows the distribution of the transverse mass associated with the events that fail the $\not\!\!E_T$-significance requirement. The distribution is consistent with the transverse mass distribution expected for a $W^{\pm}$ boson of mass 80 GeV/c^2 [49].

Figure 3.9 shows the P_T distribution of the electron candidates after removal of Z^0 and $W^{\pm}$ bosons as described above. The high-P_T shoulder is no longer visible.

[4]Only the transverse mass can be determined because CDF is not capable of measuring the longitudinal component of the $W^{\pm}$ boson momentum.

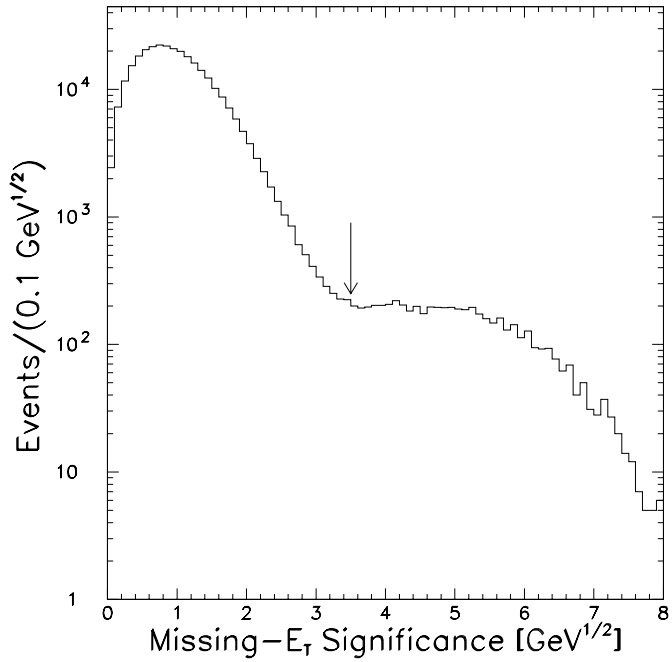

Figure 3.7: Distribution of the ratio of missing transverse energy to the square root of the total transverse energy in candidate electron events. The arrow indicates the value below which B-hadron decay electron candidates were accepted.

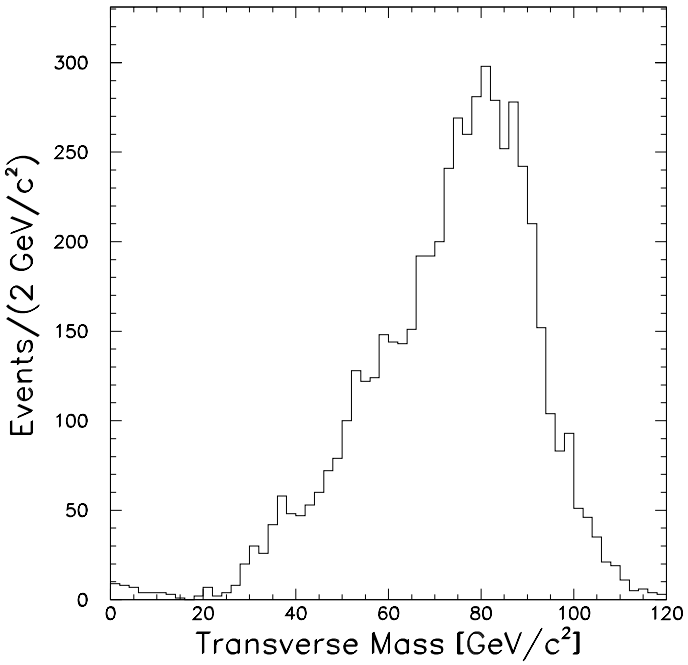

Figure 3.8: Transverse mass distribution for candidate electrons that fail the $\not\!\!E_T$-significance requirement.

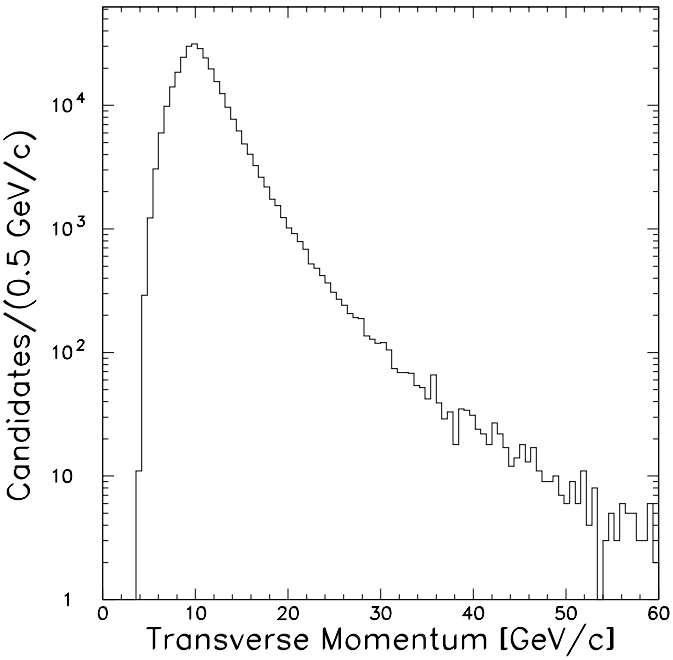

Figure 3.9: Transverse momentum distribution of candidate electrons after the removal of Z^0 and $W^{\pm}$ bosons. The high-P_T shoulder seen in Figure 3.3 is now absent.

3.3.3 Charm Decay Electrons

Electrons are also produced in semileptonic decays of charmed hadrons. However, the kinematics of charm quark fragmentation differs from those of b-quark fragmentation [43] such that the transverse energy spectrum of electrons from charm semileptonic decay is much softer than that associated with B-hadron semileptonic decay electrons. Monte Carlo calculations predict that the fraction of observed electrons with $E_T > 10$ GeV coming from charm semileptonic decay is 10% [80]. In this study, this fraction is further reduced by the reconstruction of a charmed hadron in the vicinity of the electron, as discussed in Chapter 4. We therefore assume that charm semileptonic decay electrons represent a negligible background contribution in this measurement.

Electron Identification		
$\|\eta\|$	$<$	1.1
Fiducial cut		
E_T	$>$	8.0 GeV
L_{shr}	$<$	0.2
E_{had}/E_{em}	$<$	0.04
N(3D tracks)	$=$	1
$\|z_{CES} - z_{CTC}\|$	$<$	3.0 cm
$\|x_{CES} - x_{CTC}\|$	$<$	1.5 cm
$0.75 < E_T/P_T < 1.4$		
χ^2(strip profile)	$<$	10.0
χ^2(wire profile)	$<$	15.0

Photon Conversion Rejection
$S < 0.2$ cm and $\Delta \cot\theta < 0.06$
or
$V_{res} < 0.2$

Z^0 Boson Rejection
Mass($e^{\pm}$ − high EM cluster) > 75 GeV/c^2

$W^{\pm}$ Boson Rejection
$\not\!\!E_T > 3.5\sqrt{\Sigma E_T}$

Table 3.2: Summary of electron identification criteria.

3.4 Electron Candidate Sample

Events in the Run 1 inclusive electron sample that had at least one electron candidate satisfying the criteria summarized in Table 3.4 were selected for further analysis. The final data sample consisted of three million electron candidates. Figure 3.10 depicts a graphical representation of a Run 1A electron candidate event, typical of the events in this sample.

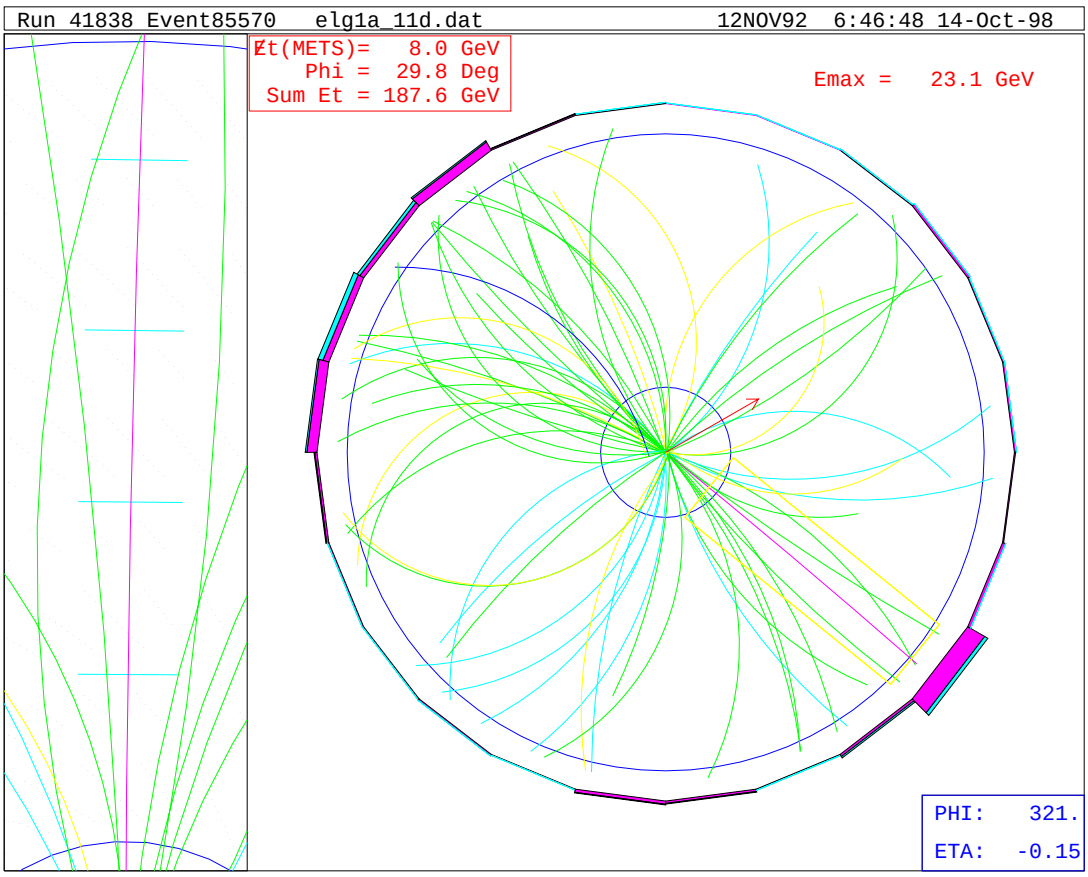

Figure 3.10: Graphical event display diagram depicting a typical electron event. The end view of the CDF detector is shown. The inner and outer circles represent the inner and outer walls of the CTC, respectively. The rectangular box locates the stiff track associated with the electron; a blow-up of the box is shown to the left. The shaded bars outside the outer wall of the CTC represent energy deposition in the calorimeter towers. Electromagnetic energy deposits are darkly shaded; hadronic energy deposits are shaded more lightly. The height of the bar represents the relative magnitude of energy deposition. The stiff track associated with the electron points to a calorimeter tower with a large deposit of electromagnetic energy (15.9 GeV). The arrow pointing away from the interaction region at the centre of the detector represents the $\not\!\!E_T$ direction; the magnitude is listed in the top-left corner.

Chapter 4

Charmed Hadron Identification

The charmed hadron from the semileptonic B-hadron decay appears in the vicinity of the electron, as depicted in Figure 4.1, due to the fact that the B hadron is boosted significantly from its decay frame to the lab frame. The charmed hadron decays with a relatively short lifetime (typically $10^{-12} - 10^{-13}$ s) into its daughter particles. We reconstruct the charmed hadron candidates by searching for combinations of charged tracks in a cone in $\eta - \phi$ space with radius $R_{cone} = \sqrt{\Delta\eta^2 + \Delta\phi^2} = 1.0$ around the electron candidate. Calculations show that the B decay daughters all fall into this cone at least 82% of the time.

The charge of the electron is known and is correlated with the charge of the partner charmed hadron (and with its daughters). Since the CDF detector is not capable of distinguishing between kaon and pion candidates, all tracks with the appropriate charge are considered as candidates of either species. The mass of the hypothesized daughter particle is assigned to the track candidate and the invariant mass of the charmed-hadron candidate is formed. When the daughter assignments are correct, the charmed-hadron resonance appears as a peak in the invariant mass distribution of the charmed-hadron candidates. The combinations with incorrect mass assignments contribute to a combinatorial background on which the resonance peak sits.

In principle, the same charge correlation could be mimicked by $c\overline{c}$ production via gluon splitting, where one c quark fragments into one of the charmed hadrons we reconstruct in this analysis and the other decays semileptonically. The kinematics of

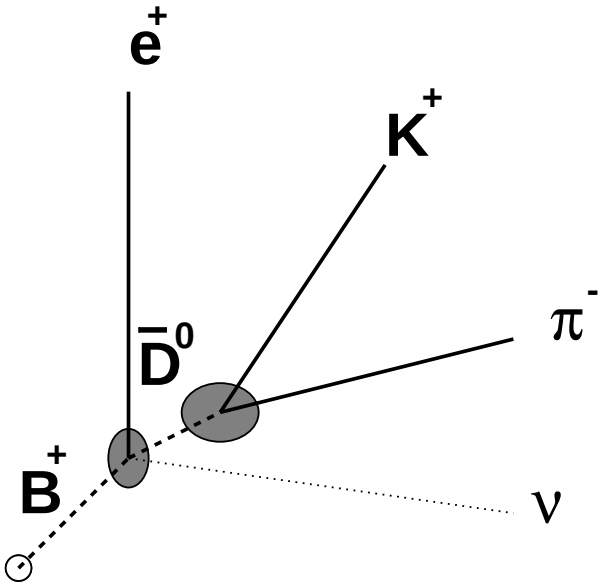

Figure 4.1: Schematic diagram depicting the semileptonic decay of a B^+ meson and the subsequent hadronic decay of the $\overline{D}^0$ meson.

this type of event are such that its contribution to our final sample is negligible after the application of the E_T and P_T criteria to the electron candidates [80].

4.1 Common Selection Criteria

This measurement is primarily a counting experiment to determine the relative number of events in each B hadron channel. Therefore, a single comprehensive data sample with a minimum of biases between different decay modes is needed. We choose kinematical cuts so as to keep the selections in the various channels as similar as possible. In order to reduce the statistical uncertainties of these measurements, we choose hadron selection criteria that maximize the signal significance, $N_s/\sigma(N_s)$, in the majority of channels, where the signal N_s is the observed number of candidate events and $\sigma(N_s)$ is determined by the maximum likelihood fit to the signal distribution. The quantity $\sigma(N_s)$ is related to the statistical uncertainties on the yields of the signal and the background under the signal. The requirements imposed on the hadron tracks in each channel are discussed in later sections.

4.1.1 Track Quality Criteria

To reduce the combinatorial background arising from poorly-measured tracks in the CDF detector, we impose several track-quality criteria. For each event, we require that at least two axial CTC layers have at least four wire hits and at least two stereo CTC layers have at least two wire hits. Furthermore, the hadron tracks are required to have three or more SVX hits. The χ^2_{SVX} per hit, defined to be the increase in the χ^2 of the track fit per SVX hit with the addition of SVX hit information in the CTC track fit, is required to be less than six.

The hadronic daughter tracks are required to satisfy several transverse momentum criteria. The tracking efficiency of the CTC is effectively zero for tracks with P_T below 0.3 GeV/c and rises quickly with increasing P_T until about 0.4 GeV/c, where it approaches the plateau efficiency of 96% [81]. To ensure that the tracking efficiency for daughter tracks is well understood, we require that all daughters have a transverse momentum in excess of 0.4 GeV/c.

Each track considered in the charmed-hadron reconstruction is required to exit the CTC at a radius greater than 110 cm. This radius corresponds to the radial position of the outer edge of the second-outermost axial superlayer. This requirement ensures that the track crossed at least eight of the nine superlayers and deposited hits on a large number of wires, in turn ensuring a well-measured track [81].

We apply tighter P_T cuts on certain daughter particles to reduce the combinatorial background. These P_T cuts were selected by optimizing the signal significance in each channel. The optimal values we found were $P_T(K) > 1.2$ GeV/c, $P_T(\pi) > 0.5$ GeV/c and $P_T(p) > 2.0$ GeV/c. The P_T cut on the "bachelor" pion π_s produced in the decay $D^*(2010)^- \to \overline{D}^0\pi_s$ decay is relaxed to 0.4 GeV/c.[1]

[1]The phase space for the bachelor pion in the $D^*(2010)^- \to \overline{D}^0\pi_s^-$ decay is limited due to the similar masses of the $D^*(2010)^-$ and $\overline{D}^0$ mesons. For this reason, the bachelor pion typically has a transverse momentum below 1.0 GeV/c.

4.1.2 Primary Vertex Selection

A proton-antiproton interaction in a given event yields a primary vertex, which is identified by the VTX. In any event, several primary vertices may be present along the z axis of the CDF detector. The VTX detector measures the z coordinate of each primary vertex on an event-by-event basis. The number of VTX hits associated with a primary vertex determines the quality of that primary vertex. The $x - y$ position of a primary vertex is constrained by the transverse circular beam spot size and the slope of the beam in the z direction.

Two quantities used in the charmed-hadron reconstruction require knowledge of the primary vertex in which the B hadron was produced: the daughter-track impact parameter, d_0, and the apparent transverse decay length of the charmed hadron, L_{xy}, as we discuss in the next sections. To ensure that the appropriate primary vertex is used for the calculation of these quantities, all high quality vertices are examined and the vertex closest in z to the charmed-hadron decay vertex is chosen as the primary vertex for each event.

4.1.3 Charmed-Hadron Decay Vertex

The daughter particles of the charmed-hadron decay are constrained to come from a common vertex. This is done by performing a least-squares fit of the daughter-track-candidate helix parameters and forcing the tracks to originate from a common point in space. In the fit, the track parameters measured using the combined CTC and SVX information are adjusted to minimize the χ^2 of the helix parameters consistent with the vertex constraint. The confidence level, CL, associated with the χ^2 of the fit is available as an additional selection criterion.

Bottom hadrons have a relatively long lifetime and therefore travel some distance from their production point before decaying semileptonically into an electron, a charmed hadron and a neutrino (refer to Figure 4.1). The charmed hadron travels further before decaying into its daughter hadrons. The charmed-hadron decay vertex is therefore expected to be displaced from the primary vertex and from the electron

trajectory. We define the apparent transverse decay length, L_{xy}, of the charmed hadron as the transverse distance between the primary vertex and the charm decay vertex. To reduce the combinatorial background in each channel, we require that L_{xy} be inconsistent with zero. In particular, we demand $L_{xy}/\sigma(L_{xy}) > 1.0$, where $\sigma(L_{xy})$ is the uncertainty in L_{xy} determined by the least-squares fit of the decay vertex position. The mean value of $\sigma(L_{xy})$ is about 65 μm.

4.1.4 Track Impact Parameter

The impact parameter, d_0, for each hadron track is determined with respect to the selected primary vertex. The daughter-track impact parameter can be used to distinguish between prompt tracks coming directly from the primary vertex and displaced tracks produced in the secondary decay of the charmed hadron. Prompt tracks have an impact parameter consistent with zero within measurement uncertainties whereas tracks from the secondary decay vertex have impact parameters typically displaced from the primary vertex. Therefore, by requiring that each daughter track have an impact parameter inconsistent with zero as determined by the uncertainty $\sigma(d_0)$ calculated from the results of the least-squares fit, we reduce much of the combinatorial background from prompt tracks while maintaining a high efficiency for tracks from secondary decays. We apply the criterion $|d_0|/\sigma(d_0) > 1.5$ for all the daughters of the charmed-hadron decays.[2]

In principle, one could require that the impact parameter be on the side of the primary vertex consistent with the direction of travel of the particle. We examined the effectiveness of this additional constraint and found that it did not improve the significance of the signals. Therefore, this measurement uses an unsigned impact parameter cut.

[2]The only exception is the bachelor pion π_s^- in the $D^*(2010)^- \to \overline{D}^0\pi_s^-$ decay to which no impact parameter criterion is applied.

4.1.5 B-Hadron Mass Cut

The invariant mass of the electron–charmed-hadron system must be less than the mass of the parent B hadron. Since the B mesons all have similar masses, we require that the mass of the electron–charmed-meson systems be less than 5.0 GeV/c^2. Since the $\overline{\Lambda}_b^0$ baryon is heavier, we relax this threshold to 5.3 GeV/c^2 for the e^+–Λ_c^- system.

4.2 Charmed-Hadron Signals

In this section, we describe the detailed requirements for the reconstruction of each charmed hadron. The method of determining the signal yield is the same for all channels except for the $D^*(2010)^-$ reconstruction, which is described in detail below. For the other channels, we plot the invariant mass of the daughter candidates of the charmed hadron decay and fit a Gaussian distribution to the signal peak. In principle, the combinatorial background distributions in these channels are associated with an exponential decay, but a linear fit to the background describes the data equally well in all channels except for the $\overline{D}^0 \to K^+\pi^-$ decay. We allow the resonance mass and width to float in the fits. The signal yield is determined from the area of the Gaussian fit. The uncertainty in the signal yield is obtained from the fit.

4.2.1 $\overline{D}^0$ Meson Reconstruction

The $\overline{D}^0$ meson candidates are identified by looking for the products of the $\overline{D}^0 \to K^+\pi^-$ decay. The common selection criteria described above are applied. No attempt is made to reject $D^{*-} \to \overline{D}^0\pi^-$ candidates from the $\overline{D}^0$ sample. The $\overline{D}^0$ candidate invariant mass distribution is shown in Figure 4.2. The $\overline{D}^0$ signal contains 1848 ± 58 $\overline{D}^0$ decays. The fitted mass and width are 1.8633 ± 0.0003 GeV/c^2 and 9.7 ± 0.3 MeV/c^2, respectively. The mass is consistent with the world average $\overline{D}^0$ mass of 1.8646 ± 0.0005 GeV/c^2 [49].

To verify that the reconstructed $\overline{D}^0$ mesons come from $B^+ \to \overline{D}^0 e^+ \nu_e X$ decays, we reconstruct $\overline{D}^0$ mesons in events with electrons of the wrong charge, that is, we

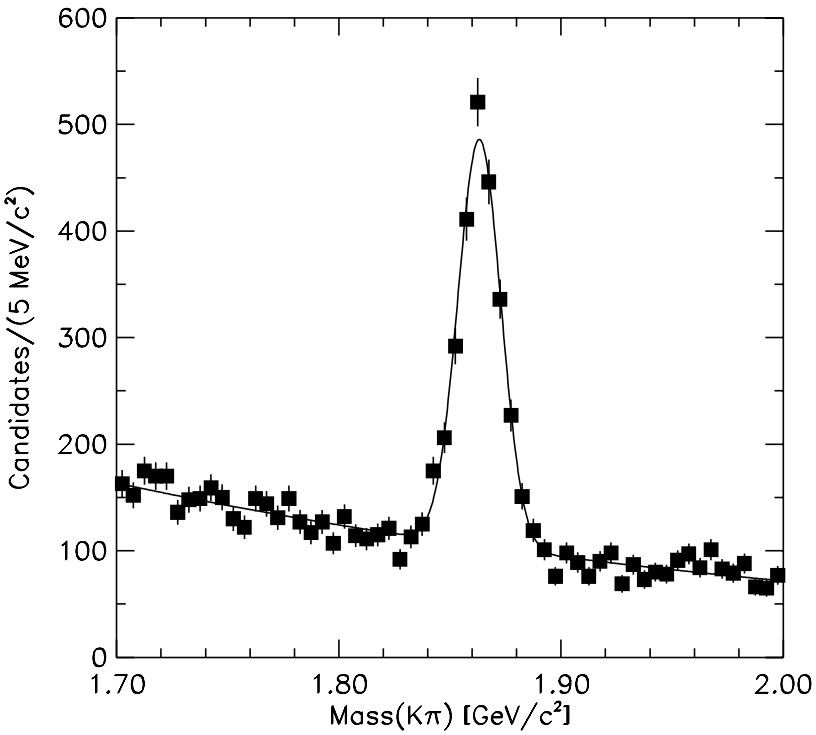

Figure 4.2: Invariant mass distribution of $\overline{D}^0$ meson candidates in 110 pb^{-1} of Run 1 inclusive electron data. The curve is the result of a fit to the data using a Gaussian signal distribution and an exponential background.

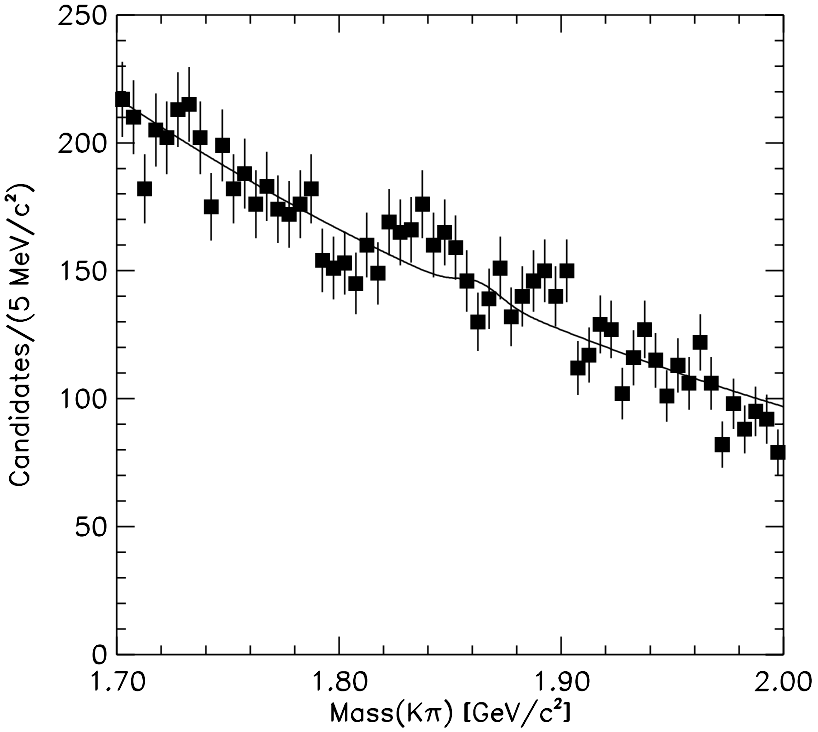

Figure 4.3: Invariant mass distribution of $\overline{D}^0$ meson candidates in 110 pb^{-1} of wrong-sign Run 1 inclusive electron data. The curve is the result of a fit to the data using a Gaussian signal distribution and an exponential background.

reconstruct $K^+\pi^-$ candidates in e^- events.[3] The invariant mass distribution of $K\pi$ candidates in the wrong-sign electron sample is shown in Figure 4.3. A fit to a Gaussian signal distribution on an exponential background indicates an insignificant $\overline{D}^0$ signal of 26 ± 34 candidates. Therefore, we take the charmed-hadron yield in the right-sign electron sample to represent the parent B-hadron semileptonic decay yield.

4.2.2 $D^*(2010)^-$ Meson Reconstruction

The $D^*(2010)^-$ meson candidates are identified by looking for the products of the $D^*(2010)^- \to \overline{D}^0\pi_s^-$ decay, where $\overline{D}^0 \to K^+\pi^-$ and π_s^- represents the "bachelor" pion. The $\overline{D}^0$ meson is first reconstructed according to the method described above. We ensure that the mass of the $K\pi$ system be consistent with that of the $\overline{D}^0$ meson by

[3]Similarly, we reconstruct $K^-\pi^+$ candidates in e^+ events.

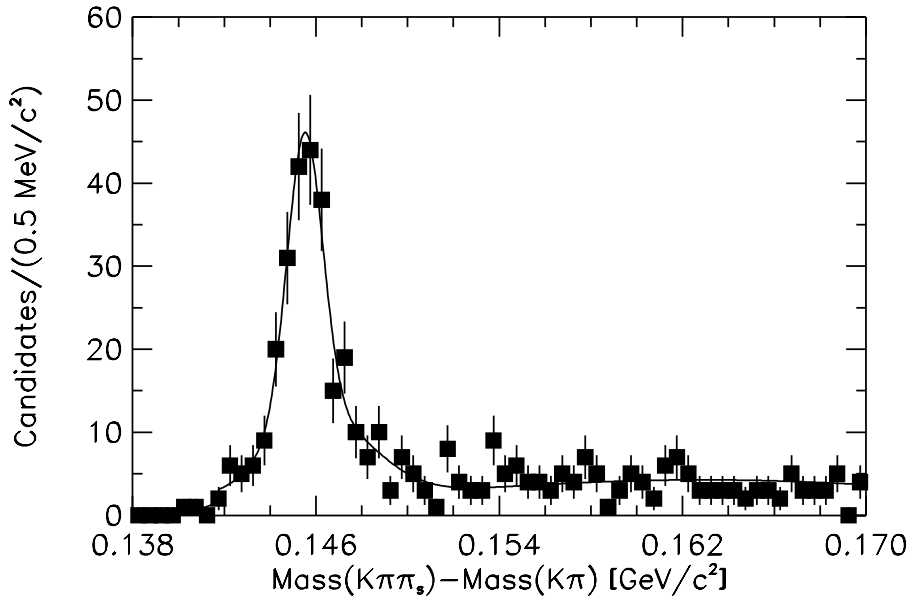

Figure 4.4: Mass difference distribution, $\Delta M = M(K\pi\pi_s) - M(K\pi)$, for $D^*(2010)^-$ candidates in 110 pb^{-1} of Run 1 inclusive electron data. The curve is the result of a fit described in the text.

requiring $1.80 < \text{Mass}(K\pi) < 1.95$ GeV/c^2. Finally, we search for the bachelor pion from the $D^*(2010)^- \to \overline{D}^0\pi_s^-$ decay by considering as a π_s candidate every remaining particle with charge opposite to that of the electron with $P_T > 0.4$ GeV/c.

The mass difference distribution, $\Delta M = \text{Mass}(K\pi\pi_s) - \text{Mass}(K\pi)$, is shown in Figure 4.4 and illustrates a clear peak near threshold typical of the $D^*(2010)^- \to \overline{D}^0\pi_s^-$ decay. The momentum resolution of the bachelor pion is reduced compared to that of the higher P_T tracks from the $\overline{D}^0$ decay, yielding a characteristic double-Gaussian shape for the signal peak in the ΔM distribution. The background shape is modeled using a threshold function, which is not well constrained by the data in Figure 4.4. We constrain the shape of the background by reconstructing the "wrong-sign" charge combinations, $K^+\pi^-\pi_s^+$, where the $K^+\pi^-$ pair associated with a real $\overline{D}^0$ candidate is combined with a bachelor pion of the wrong charge. No $D^*(2010)^-$ signal peak is evident in the wrong-sign mass difference distribution, shown in Figure 4.5. A fit to the sum of two Gaussian distributions on the threshold background of the signal sample performed simultaneously to a fit to the threshold background only in the

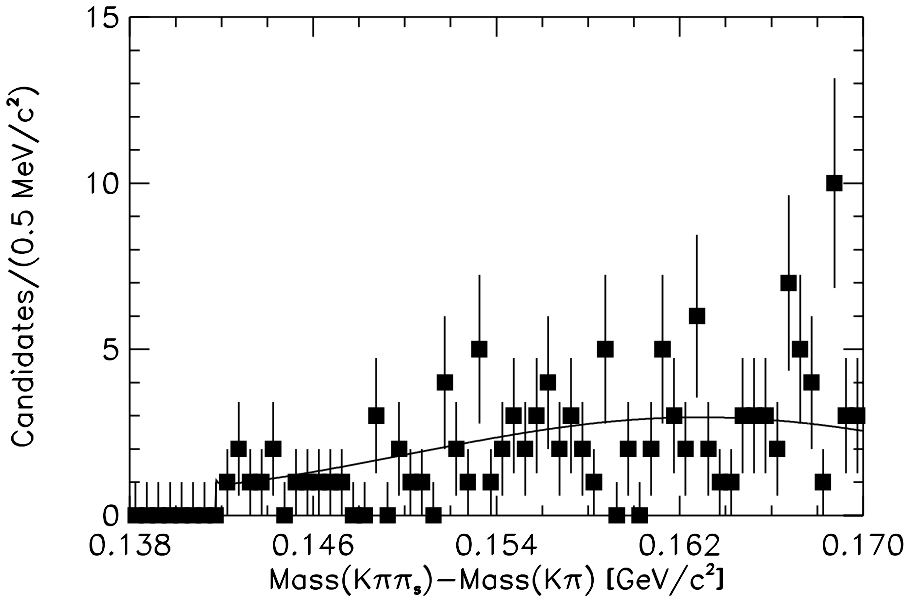

Figure 4.5: Mass difference distribution, $\Delta M = M(K\pi\pi_s) - M(K\pi)$, for wrong-sign $K^+\pi^-\pi_s^+$ candidates in 110 pb^{-1} of Run 1 inclusive electron data. The curve is the result of a fit described in the text.

wrong-sign sample indicates that the $D^*(2010)^-$ signal contains 249 ± 19 $D^*(2010)^-$ decays. The fitted resonance mass is 0.1455 ± 0.0001 GeV/c^2, consistent with the world average $D^*(2010)^-/\overline{D}^0$ mass difference of 0.145397 ± 0.000030 GeV/c^2 [49].

4.2.3 D^- Meson Reconstruction

The D^- meson is identified by looking for the products of the $D^- \to K^+\pi^-\pi^-$ decay. The common selection criteria described above are applied. The D^- candidate invariant mass distribution is shown in Figure 4.6. The D^- signal contains 736 ± 62 D^- decays. The fitted mass and width are 1.8673 ± 0.0009 GeV/c^2 and 10.0 ± 1.0 MeV/c^2, respectively. The mass is consistent with the world average D^- mass of 1.8693 ± 0.0005 GeV/c^2 [49]

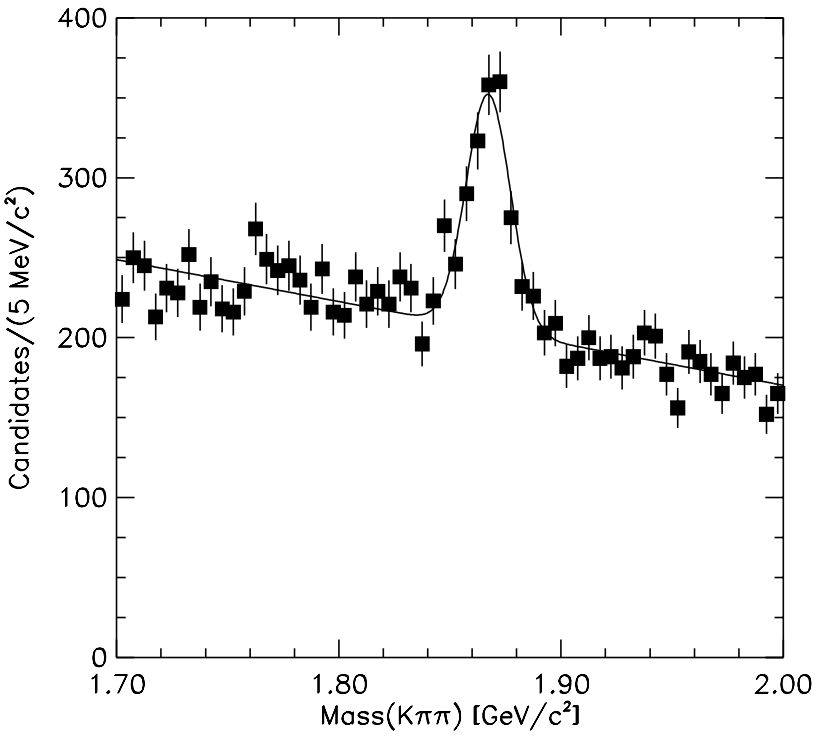

Figure 4.6: Invariant mass distribution of D^- meson candidates in 110 pb^{-1} of Run 1 inclusive electron data. The curve is the result of a fit to the data using a Gaussian signal distribution and a linear background.

4.2.4 D_s^- Meson Reconstruction

The D_s^- meson candidates are identified by looking for the products of the $D_s^- \to \phi\pi^-$ decay where $\phi \to K^+K^-$. The common selection criteria described above are applied. The lifetime of the ϕ meson is very short so both kaons and the pion are required to come from a common vertex.

In this channel, there are two additional criteria that are highly efficient for signal decays and effective at rejecting combinatorial backgrounds. The first requirement is a ϕ mass cut. We require that the mass of the dikaon system be within 10 MeV/c^2 of the world average ϕ mass of of 1.019413 ± 0.000008 GeV/c^2 [49]. The second requirement takes advantage of the difference between the angular distribution of $D_s^- \to \phi\pi^-$ decays and that of random combinations. The $\cos\psi$ distribution for $D_s^- \to \phi\pi^-$ decays is proportional to $\cos^2\psi$, where ψ is the angle between the K and D_s candidates in the ϕ rest frame. The $\cos\psi$ distribution for random combinations is approximately flat. We require that each kaon satisfy the criterion $|\cos\psi| > 0.4$.

The D_s^- candidate invariant mass distribution is shown in Figure 4.7. The D_s^- signal contains 59 ± 10 D_s^- decays. The fitted mass and width are 1.967 ± 0.002 GeV/c^2 and 7.0 ± 1.6 MeV/c^2, respectively. The mass is consistent with the world average D_s^- mass of 1.9685 ± 0.0006 GeV/c^2 [49]. To improve the quality of the fit, we include a second Gaussian signal to account for the Cabibbo-suppressed $D^- \to \phi\pi^-$ decays at 1.87 GeV/c^2. We obtain a $D^- \to \phi\pi^-$ yield of 9 ± 5 events which, although not a statistically significant observation, is consistent with the known branching fraction for this decay.

The D_s^- candidates in the signal peak in Figure 4.7 are associated with resonant $\phi \to K^+K^-$ decays, as shown in Figure 4.8. To obtain this plot, the ϕ mass window is increased to 40 MeV/c^2 in the D_s^- reconstruction. The K^+K^- invariant mass is plotted for D_s^- candidates with Mass($KK\pi$) within 25 MeV/c^2 of the world average D_s^- mass of 1.9685 GeV/c^2 [49]. The ϕ signal contains 46 ± 12 ϕ decays. The fitted mass and width are 1.0209 ± 0.0006 GeV/c^2 and 2.5 ± 0.8 MeV/c^2, respectively. The mass is consistent with the world average ϕ mass. The fitted ϕ event yield is consistent

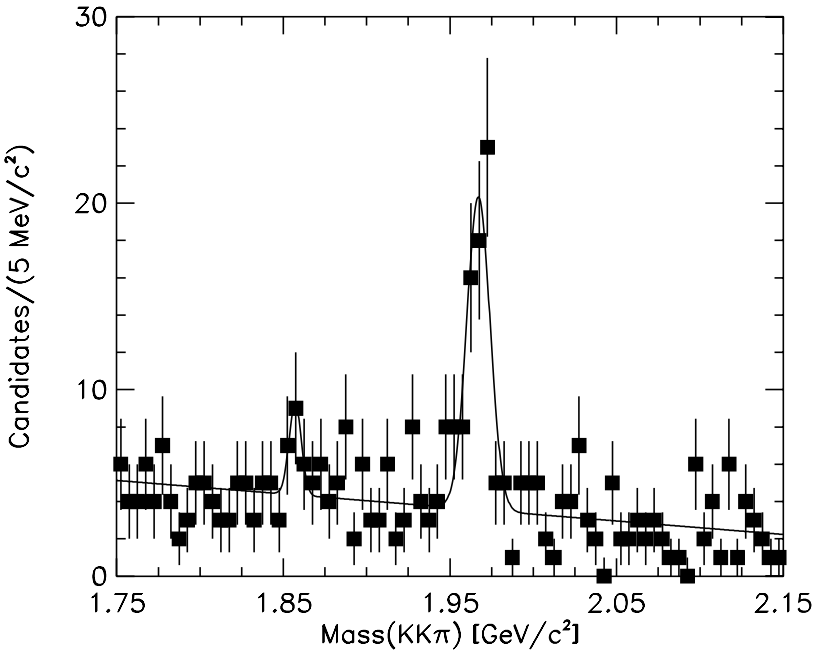

Figure 4.7: Invariant mass distribution of D_s^- meson candidates in 110 pb^{-1} of Run 1 inclusive electron data. The curve is the result of a fit to the data using two Gaussian signal distributions, one for D_s^- candidates and one for D^- candidates, and a linear background.

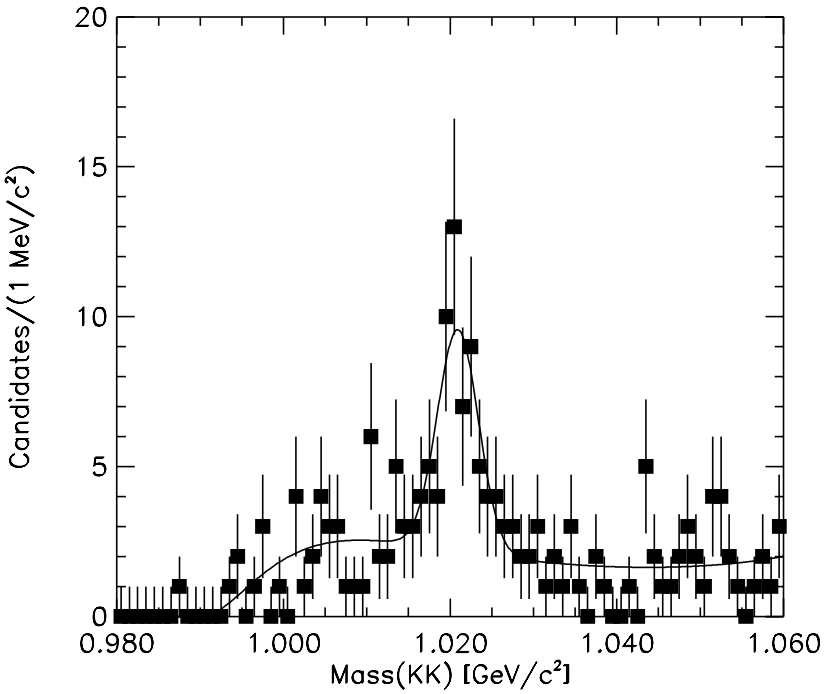

Figure 4.8: Invariant mass distribution of ϕ meson candidates in 110 pb^{-1} of Run 1 inclusive electron data. The curve is the result of a fit to the data using a Gaussian signal distribution and a threshold background.

with the D_s^- event yield of 59 ± 10, given the large statistical uncertainties in the KK invariant mass distribution.

4.2.5 Λ_c^- Baryon Reconstruction

The Λ_c^- baryon candidates are identified by looking for the products of the $\Lambda_c^- \to \overline{p}K^+\pi^-$ decay. The common selection criteria described above are applied. Since the Λ_c^- signal is relatively small on top of a large combinatorial background, we apply two additional criteria to improve the significance of this measurement.

The confidence level of the Λ_c^- decay vertex fit is required to be greater than 1%. This requirement is not imposed on the vertex fits in the other channels due to the difficulty in determining its efficiency, an issue we discuss in Chapter 5.

The majority of the combinatorial background in the charmed-baryon candidate sample is associated with pions being misidentified as proton or kaon candidates.

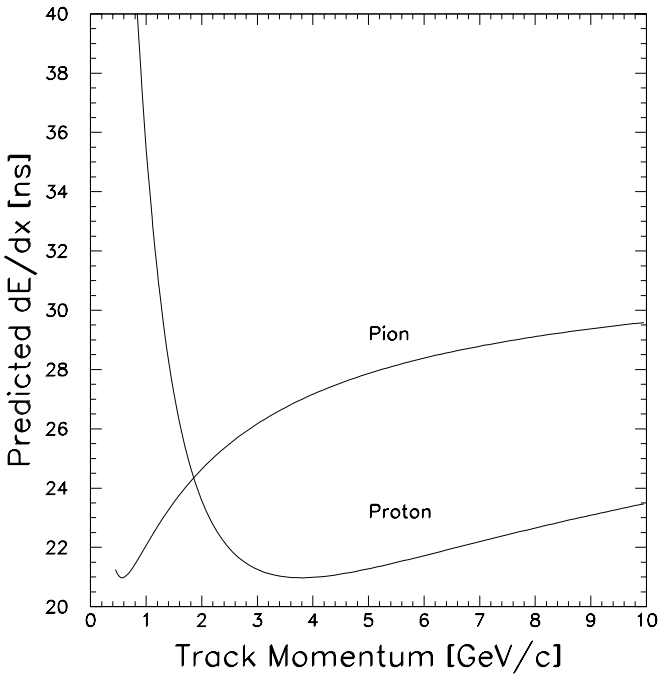

Figure 4.9: Expected dE/dx distribution as a function of momentum in the CTC for pions and protons. dE/dx is in units of nanoseconds.

The CDF detector is incapable of differentiating between pions and kaons but protons, which are significantly heavier than pions or kaons, can be distinguished by examining the ionization deposited by the charged particle in the CTC as a function of the distance traveled. We call this quantity dE/dx. Each particle of a particular mass has a given mean dE/dx value as a function of momentum in the CTC. Figure 4.9 shows the expectation for this distribution for protons and pions. At CDF, dE/dx is measured in nanoseconds, as the ionization yield is determined from the average time-over-threshold of the CTC signal. The dE/dx measurement uncertainties are large. In order to ensure high efficiency for this selection criterion, we apply a significance cut, $(dE/dx_{meas} - dE/dx_{pred})/\sigma(dE/dx) < 1.0$, to all proton candidates, where $\sigma(dE/dx)$ is the uncertainty in the dE/dx measurement. The cut is one-sided, since the dE/dx distribution for protons always lies below that for pions for tracks above a candidate momentum of 2 GeV/c.

The resulting Λ_c^- candidate invariant mass distribution is shown in Figure 4.10. The Λ_c^- signal contains 79 ± 17 Λ_c^- decays. The fitted mass and width are 2.285 ± 0.001

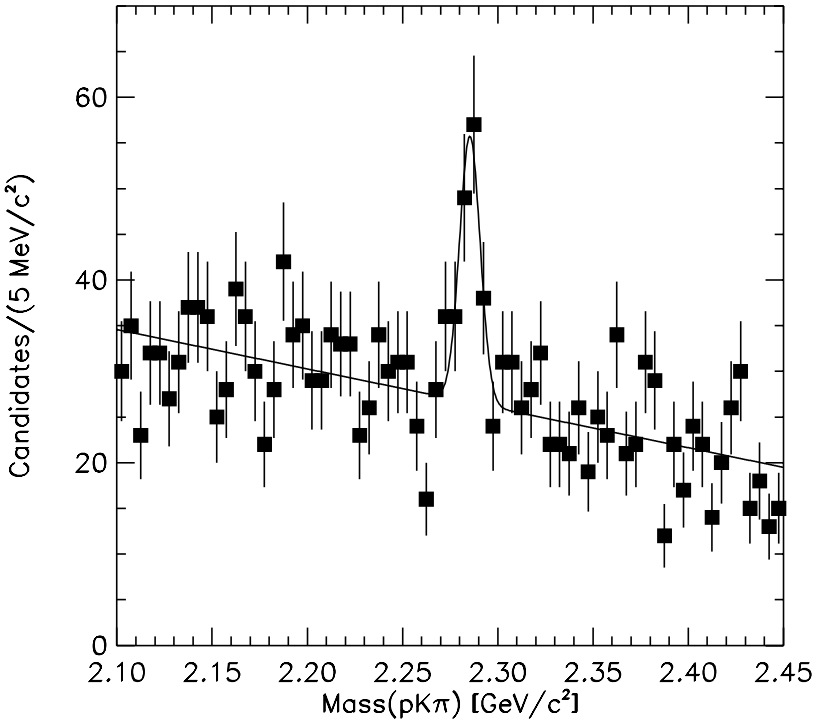

Figure 4.10: Invariant mass distribution of Λ_c^- baryon candidates in 110 pb^{-1} of Run 1 inclusive electron data. The curve is the result of a fit to the data using a Gaussian signal distribution and a linear background.

GeV/c^2 and 5.4 ± 1.5 MeV/c^2, respectively. The mass is consistent with the world average Λ_c^- mass of 2.2849 ± 0.0006 GeV/c^2 [49].

4.2.6 Summary

We have reconstructed charmed hadron candidates in five channels, summarized in Table 4.1. We have shown that no charmed hadron signal is evident in the wrong-sign electron sample and conclude that each charmed-hadron candidate is associated with a B hadron decay.

Channel	Signal Yield (events)	Central Value ($\mathrm{GeV/c^2}$)	Width ($\mathrm{MeV/c^2}$)
$\overline{D}^0 \to K^+\pi^-$	1848 ± 58	1.8633 ± 0.0003	9.7 ± 0.3
$D^{*-} \to \overline{D}^0\pi^-$	249 ± 19	0.1455 ± 0.0001	N/A
$D^- \to K^+\pi^-\pi^-$	736 ± 62	1.8673 ± 0.0009	10.0 ± 1.0
$D_s^- \to \phi\pi^-$	59 ± 10	1.967 ± 0.002	7.0 ± 1.6
$\Lambda_c^- \to \overline{p}K^+\pi^-$	79 ± 17	2.285 ± 0.001	5.4 ± 1.5

Table 4.1: Summary of charmed-hadron signal fits.

Chapter 5

Efficiency Calculations

In this chapter, we discuss the corrections associated with the overall acceptances and reconstruction efficiencies for each decay channel. Kinematic and geometric cuts are associated with "acceptances" and identification criteria are associated with "efficiencies". It is not always easy to differentiate between an acceptance and an efficiency (as in the trigger study discussed in Section 5.3.2) but we try to separate the two components as much as possible in this chapter.

The advantage of measuring a ratio of fragmentation fractions is that we can expect many of the reconstruction efficiencies to cancel in the ratio. These include

- the plateau Level 2 electron trigger efficiency,
- the electron identification efficiency,
- the conversion removal efficiency and
- two-track finding efficiency.

Several efficiencies, unfortunately, do not cancel in principle and their ratios must be estimated. Some of these efficiencies can be measured in the data, such as the trigger efficiency and vertexing efficiencies. For other efficiencies, we use a Monte Carlo calculation with a detector simulation, as described below.

5.1 Sample Cross Contamination

To address the issue of cross-contamination in the final state samples, we account for all contributions to each sample using either known or estimated branching fractions in our calculations. Tables 5.1, 5.2 and 5.3 list the branching fractions for the contributions to the B^+, B^0 and B_s^0 decay channels we consider in this study. We assume that all of the semileptonic decays proceed through one of the three decay modes

$$\begin{aligned} B &\rightarrow De^+\nu_e \\ B &\rightarrow D^*e^+\nu_e, \text{and} \\ B &\rightarrow D^{**}e^+\nu_e, \end{aligned}$$

and denote the branching fractions for these three decays to be g, g^*, and g^{**}. We also assume separate branching fractions for the three B mesons, denoted by g_+, g_+^*, and g_+^{**} for the B^+-meson decays, g_0, g_0^*, and g_0^{**} for the B^0-meson decays and g_s, g_s^*, and g_s^{**} for the B_s^0-meson decays.

The branching fractions g_0, g_+, g_0^* and g_+^* in Tables 5.1, 5.2 and 5.3 are experimentally-determined world average values, as are the subsequent daughter branching fractions [49]. On the other hand, the g^{**} branching fractions have not been measured for any of the B meson species. The g^{**} branching fractions given in Tables 5.1, 5.2 and 5.3 are determined by requiring the sums of the three branching fractions to equal the measured world average total semileptonic branching fractions, i.e.,

$$\begin{aligned} g_0^{tot} &= g_0 + g_0^* + g_0^{**}, \\ g_+^{tot} &= g_+ + g_+^* + g_+^{**}. \end{aligned}$$

We calculate the following values:

$$\begin{aligned} g_0^{**} &= (3.85 \pm 0.42)\%, \\ g_+^{**} &= (3.29 \pm 0.89)\%. \end{aligned}$$

Decay Channel	Individual Branching Fraction (%)	Combined Branching Fraction (%)	Destination Sample
$B^+ \to \overline{D}^0 e^+ \nu_e$	1.86 ± 0.33	1.86 ± 0.33	$\overline{D}^0 e^+$
$B^+ \to \overline{D}^*(2007)^0 e^+ \nu_e$	5.3 ± 0.8		
$\to \overline{D}^0 \pi^0/\gamma$	100	5.3 ± 0.8	$\overline{D}^0 e^+$
$B^+ \to \overline{D}^{**}({}^3P_0)^0 e^+ \nu_e$	0.089 ± 0.030		
$\to D^- \pi^+$	67	0.060 ± 0.020	$D^- e^+$
$\to \overline{D}^0 \pi^0$	33	0.029 ± 0.010	$\overline{D}^0 e^+$
$B^+ \to \overline{D}^{**}({}^3P_1)^0 e^+ \nu_e$	0.089 ± 0.030		
$\to \overline{D}^*(2007)^0 \pi^0$	33		
$\to \overline{D}^0 \pi^0/\gamma$	100	0.029 ± 0.010	$\overline{D}^0 e^+$
$\to D^*(2010)^- \pi^+$	67		
$\to \overline{D}^0 \pi^-$	68.3 ± 1.4	0.041 ± 0.014	$\overline{D}^0 e^+ / D^{*-} e^+$
$\to D^- \pi^0/\gamma$	31.7 ± 2.5	0.019 ± 0.006	$D^- e^+$
$B^+ \to \overline{D}^{**}({}^1P_1)^0 e^+ \nu_e$	0.98 ± 0.3		
$\to \overline{D}^*(2007)^0 \pi^0$	33		
$\to \overline{D}^0 \pi^0/\gamma$	100	0.32 ± 0.11	$\overline{D}^0 e^+$
$\to D^*(2010)^- \pi^+$	67		
$\to \overline{D}^0 \pi^-$	68.3 ± 1.4	0.45 ± 0.15	$\overline{D}^0 e^+ / D^{*-} e^+$
$\to D^- \pi^0/\gamma$	31.7 ± 2.5	0.21 ± 0.07	$D^- e^+$
$B^+ \to \overline{D}^{**}({}^3P_2)^0 e^+ \nu_e$	0.98 ± 0.3		
$\to \overline{D}^0 \pi^0$	0.229	0.22 ± 0.07	$\overline{D}^0 e^+$
$\to \overline{D}^*(2007)^0 \pi^0$	0.103		
$\to \overline{D}^0 \pi^0/\gamma$	100	0.10 ± 0.03	$\overline{D}^0 e^+$
$\to D^- \pi^+$	0.459	0.45 ± 0.15	$D^- e^+$
$\to D^*(2010)^- \pi^+$	0.209		
$\to \overline{D}^0 \pi^-$	68.3 ± 1.4	0.14 ± 0.05	$\overline{D}^0 e^+ / D^{*-} e^+$
$\to D^- \pi^0/\gamma$	31.7 ± 2.5	0.065 ± 0.022	$D^- e^+$
$B^+ \to \overline{D}^{**}(NR)^0 e^+ \nu_e$	1.2 ± 0.4		
$\to \overline{D}^0 \pi^0$	0.112	0.13 ± 0.04	$\overline{D}^0 e^+$
$\to \overline{D}^*(2007)^0 \pi^0$	0.222		
$\to \overline{D}^0 \pi^0/\gamma$	100	0.26 ± 0.09	$\overline{D}^0 e^+$
$\to D^- \pi^+$	0.222	0.26 ± 0.09	$D^- e^+$
$\to D^*(2010)^- \pi^+$	0.444		
$\to \overline{D}^0 \pi^-$	68.3 ± 1.4	0.35 ± 0.12	$\overline{D}^0 e^+ / D^{*-} e^+$
$\to D^- \pi^0/\gamma$	31.7 ± 2.5	0.16 ± 0.06	$D^- e^+$
$B \to l^+ \nu X$	10.45 ± 0.21	10.45 ± 0.21	

Table 5.1: Branching fractions for semileptonic B^+-meson decays.

Decay Channel	Individual Branching Fraction (%)	Combined Branching Fraction (%)	Destination Sample
$B^0 \to D^- e^+ \nu_e$	2.00 ± 0.25	2.00 ± 0.25	$D^- e^+$
$B^0 \to D^*(2010)^- e^+ \nu_e$	4.60 ± 0.27		
$\to \overline{D}^0 \pi^-$	68.3 ± 1.4	3.14 ± 0.20	$\overline{D}^0 e^+ / D^{*-} e^+$
$\to D^- \pi^0 / \gamma$	31.7 ± 2.5	1.46 ± 0.14	$D^- e^+$
$B^0 \to D^{**}({}^3P_0)^- e^+ \nu_e$	0.10 ± 0.02		
$\to \overline{D}^0 \pi^-$	67	0.070 ± 0.011	$\overline{D}^0 e^+$
$\to D^- \pi^0$	33	0.034 ± 0.006	$D^- e^+$
$B^0 \to D^{**}({}^3P_1)^- e^+ \nu_e$	0.10 ± 0.02		
$\to \overline{D}^*(2007)^0 \pi^-$	67		
$\to \overline{D}^0 \pi^0 / \gamma$	100	0.070 ± 0.011	$\overline{D}^0 e^+$
$\to D^*(2010)^- \pi^0$	33		
$\to \overline{D}^0 \pi^-$	68.3 ± 1.4	0.023 ± 0.004	$\overline{D}^0 e^+ / D^{*-} e^+$
$\to D^- \pi^0 / \gamma$	31.7 ± 2.5	0.011 ± 0.002	$D^- e^+$
$B^0 \to D^{**}({}^1P_1)^- e^+ \nu_e$	1.1 ± 0.2		
$\to \overline{D}^*(2007)^0 \pi^-$	67		
$\to \overline{D}^0 \pi^0 / \gamma$	100	0.77 ± 0.12	$\overline{D}^0 e^+$
$\to D^*(2010)^- \pi^0$	33		
$\to \overline{D}^0 \pi^-$	68.3 ± 1.4	0.26 ± 0.04	$\overline{D}^0 e^+ / D^{*-} e^+$
$\to D^- \pi^0 / \gamma$	31.7 ± 2.5	0.12 ± 0.02	$D^- e^+$
$B^0 \to D^{**}({}^3P_2)^- e^+ \nu_e$	1.1 ± 0.2		
$\to \overline{D}^0 \pi^-$	0.459	0.53 ± 0.08	$\overline{D}^0 e^+$
$\to \overline{D}^*(2007)^0 \pi^-$	0.209		
$\to \overline{D}^0 \pi^0 / \gamma$	100	0.24 ± 0.04	$\overline{D}^0 e^+$
$\to D^- \pi^0$	0.229	0.26 ± 0.04	$D^- e^+$
$\to D^*(2010)^- \pi^0$	0.103		
$\to \overline{D}^0 \pi^-$	68.3 ± 1.4	0.081 ± 0.013	$\overline{D}^0 e^+ / D^{*-} e^+$
$\to D^- \pi^0 / \gamma$	31.7 ± 2.5	0.037 ± 0.007	$D^- e^+$
$B^0 \to D^{**}(NR)^- e^+ \nu_e$	1.4 ± 0.2		
$\to \overline{D}^0 \pi^-$	0.222	0.30 ± 0.04	$\overline{D}^0 e^+$
$\to \overline{D}^*(2007)^0 \pi^-$	0.444		
$\to \overline{D}^0 \pi^0 / \gamma$	100	0.60 ± 0.09	$\overline{D}^0 e^+$
$\to D^- \pi^0$	0.112	0.15 ± 0.02	$D^- e^+$
$\to D^*(2010)^- \pi^0$	0.222		
$\to \overline{D}^0 \pi^-$	68.3 ± 1.4	0.21 ± 0.03	$\overline{D}^0 e^+ / D^{*-} e^+$
$\to D^- \pi^0 / \gamma$	31.7 ± 2.5	0.095 ± 0.017	$D^- e^+$
$B \to l^+ \nu X$	10.45 ± 0.21	10.45 ± 0.21	

Table 5.2: Branching fractions for semileptonic B^0-meson decays.

Decay Channel	Individual Branching Fraction (%)	Combined Branching Fraction (%)	Destination Sample
$B_s^0 \to D_s^- e^+ \nu_e$	1.87 ± 0.21	1.87 ± 0.21	$D_s^- e^+$
$B_s^0 \to D_s^{*-} e^+ \nu_e$	4.48 ± 0.33		
$\to D_s^- \gamma$	100	4.48 ± 0.33	$D_s^- e^+$
$B_s^0 \to D_s^{**}(^3P_0)^- e^+ \nu_e$	0.099 ± 0.017		
$\to \overline{D}^0 K^-$	50	0.049 ± 0.009	$\overline{D}^0 e^+$
$\to D^- K^0$	49	0.048 ± 0.008	$D^- e^+$
$\to D_s^- \gamma$	1	0.001 ± 0.000	$D_s^- e^+$
$B_s^0 \to D_s^{**}(^3P_1)^- e^+ \nu_e$	0.099 ± 0.017		
$\to \overline{D}^*(2007)^0 K^-$	50		
$\to \overline{D}^0 \pi^0/\gamma$	100	0.049 ± 0.009	$\overline{D}^0 e^+$
$\to D^*(2010)^- K^0$	49		
$\to \overline{D}^0 \pi^-$	68.3 ± 1.4	0.033 ± 0.006	$\overline{D}^0 e^+ / D^{*-} e^+$
$\to D^- \pi^0/\gamma$	31.7 ± 2.5	0.015 ± 0.003	$D^- e^+$
$\to D_s^- \gamma$	1	0.001 ± 0.000	$D_s^- e^+$
$B_s^0 \to D_s^{**}(^1P_1)^- e^+ \nu_e$	1.09 ± 0.18		
$\to \overline{D}^*(2007)^0 K^-$	35		
$\to \overline{D}^0 \pi^0/\gamma$	100	0.380 ± 0.063	$\overline{D}^0 e^+$
$\to D^*(2010)^- K^0$	35		
$\to \overline{D}^0 \pi^-$	68.3 ± 1.4	0.259 ± 0.043	$\overline{D}^0 e^+ / D^{*-} e^+$
$\to D^- \pi^0/\gamma$	31.7 ± 2.5	0.120 ± 0.022	$D^- e^+$
$\to D_s^{*-} \gamma$	25		
$\to D_s^- \gamma$	100	0.271 ± 0.045	$D_s^- e^+$
$\to D_s^- \gamma$	5	0.054 ± 0.009	$D_s^- e^+$
$B_s^0 \to D_s^{**}(^3P_2)^- e^+ \nu_e$	1.09 ± 0.18		
$\to \overline{D}^0 K^-$	30	0.326 ± 0.054	$\overline{D}^0 e^+$
$\to D^- K^0$	30	0.326 ± 0.054	$D^- e^+$
$\to \overline{D}^*(2007)^0 K^-$	20		
$\to \overline{D}^0 \pi^0/\gamma$	100	0.217 ± 0.036	$\overline{D}^0 e^+$
$\to D^*(2010)^- K^0$	19		
$\to \overline{D}^0 \pi^-$	68.3 ± 1.4	0.141 ± 0.023	$\overline{D}^0 e^+ / D^{*-} e^+$
$\to D^- \pi^0/\gamma$	31.7 ± 2.5	0.065 ± 0.011	$D^- e^+$
$\to D_s^- \gamma$	1	0.011 ± 0.002	$D_s^- e^+$
$B_s^0 \to D_s^{**}(NR)^- e^+ \nu_e$	1.28 ± 0.22		
$\to \overline{D}^0 K^-$	0.222	0.285 ± 0.050	$\overline{D}^0 e^+$
$\to \overline{D}^*(2007)^0 K^-$	0.444		
$\to \overline{D}^0 \pi^0/\gamma$	100	0.569 ± 0.098	$\overline{D}^0 e^+$
$\to D^- K^0$	0.112	0.144 ± 0.025	$D^- e^+$
$\to D^*(2010)^- K^0$	0.222		
$\to \overline{D}^0 \pi^-$	68.3 ± 1.4	0.194 ± 0.033	$\overline{D}^0 e^+ / D^{*-} e^+$
$\to D^- \pi^0/\gamma$	31.7 ± 2.5	0.090 ± 0.015	$D^- e^+$
$B_s^0 \to l^+ \nu X$	10.0 ± 0.5	10.0 ± 0.5	

Table 5.3: Branching fractions for semileptonic B_s^0-meson decays.

To determine estimates of the B_s^0-meson semileptonic branching fractions, we exploit the spectator model prediction that semileptonic decay widths for the various B hadrons are equal, i.e.,

$$\begin{aligned}\mathcal{B}(B_s^0 \to e^+\nu_e X) &= \frac{\tau(B_s^0)}{\langle\tau(B)\rangle}\mathcal{B}(B \to e^+\nu_e X) \\ &= (10.0 \pm 0.5)\%,\end{aligned}$$

where B refers to the admixture of B^+ and B^0 mesons used to determine the average B semileptonic branching fraction $\mathcal{B}(B \to e^+\nu_e X)$ and the average lifetime $\langle\tau(B)\rangle$. We use $\mathcal{B}(B \to e^+\nu_e X) = (10.45 \pm 0.21)\%$, $\tau(B_s^0) = 1.54 \pm 0.07$ ps and $\langle\tau(B)\rangle = 1.605 \pm 0.028$ ps. The latter value is the world average of the B^+ and B^0 lifetimes [49].

The spectator model predictions for the partial widths agree with the measured branching fractions for the B^+ and B^0 mesons, and so we use the latter to determine g_s and g_s^*, taking the weighted average of the world average values of the $g^{(*)}$ branching fractions for the non-strange B mesons. We obtain the following branching fractions for the B_s^0-meson semileptonic decay:

$$\begin{aligned}g_s &= (1.87 \pm 0.21)\%, \\ g_s^* &= (4.48 \pm 0.33)\%.\end{aligned}$$

Finally, using the formula $g_s^{tot} = g_s + g_s^* + g_s^{**}$ and $g_s^{tot} = (10.0 \pm 0.5)\%$, we calculate the value $g_s^{**} = (3.65 \pm 0.63)\%$.

We also use the spectator model to predict the total semileptonic decay rate of $\overline{\Lambda}_b^0$ baryons to the Λ_c^- final state. We obtain

$$\begin{aligned}\mathcal{B}(\overline{\Lambda}_b^0 \to \Lambda_c^- e^+\nu_e) &= \frac{\tau(\Lambda_b^0)}{\langle\tau(B)\rangle}\mathcal{B}(B \to e^+\nu_e X) \\ &= (7.94 \pm 0.39)\%,\end{aligned}$$

where we have used $\tau(\Lambda_b^0) = 1.22 \pm 0.05$ ps.

5.2 Monte Carlo Calculation Parameters

We use a B-hadron event generation program called BGENERATOR [82] to generate single b quarks that then fragment into a single B hadron. This calculation uses the following parameters:

- Mass(b quark)= 4.75 GeV/c^2,
- $P_T(b \text{ quark}) > 9.0$ GeV/c,
- Rapidity $|y(b \text{ quark})| < 1.5$,
- Peterson fragmentation parameter $\epsilon_b = 0.006$, and
- the Nason, Dawson and Ellis calculation for $d^2\sigma/dydP_T$ [38, 39] with the MRSD0 parton distribution functions and normalization scale $\mu = \mu_0$,

where the MRSD0 parton distribution function is a parametrization of the probability distributions for finding a parton q with a momentum fraction x inside the proton [83]. This parametrization is based on empirical measurements of the parton distributions from data on electron and neutrino deep inelastic scattering.

We use the Monte Carlo program developed by the CLEO collaboration called QQ [84] to model the B-hadron semileptonic decay into electrons and charmed hadrons. The ISGW matrix element is used for the B^0, B^+ and B_s^0 semileptonic decays. Although Isgur, Scora, Grinstein and Wise [58] restrict their discussion to semileptonic decays of B mesons, Scora developed a similar model for $\overline{\Lambda}_b^0$ baryons [85]. This model of $\overline{\Lambda}_b^0$ semileptonic decays is used for our $\overline{\Lambda}_b^0$ reconstruction efficiency calculations. The charmed hadrons are forced to decay into the daughters that we reconstruct in this analysis. After the decay, we require the resulting electrons to have a generated $P_T > 7.0$ GeV/c. We use the detector simulation program QFL$'$ [86], an algorithm that utilizes parametrizations to model the detector response.

The values for the P_T and y generation parameters were selected to avoid biasing the efficiencies of the nominal threshold values applied later in this analysis while at

the same time maintaining high generation efficiency. Two million events were generated for each channel[1], with approximately 100 000 events passing the acceptance cuts listed above.

5.3 Reconstruction Efficiencies

The electron identification efficiencies are expected to cancel in this study. Thus, the only selection criteria applied to the simulated electron are the following kinematic and geometric cuts:

- $E_T(e) > 8.0$ GeV,
- $|\eta| < 1.1$,
- $N_{trk} \equiv 1$, where N_{trk} is the number of charged particle tracks pointing to the electromagnetic energy cluster, and
- the detector fiducial region requirement.

The charmed hadron reconstruction used in the analysis of the data is then applied to the simulated events passing the above criteria. The fraction of the two million events in a particular decay chain passing the reconstruction is taken to be the acceptance for the particular decay channel. Tables 5.4 and 5.5 show the geometric acceptances and reconstruction efficiencies for each direct decay chain.

The reconstruction efficiencies shown in Tables 5.4 and 5.5 are for the directly-produced charmed hadrons. Tables 5.6 and 5.7 show the reconstruction efficiencies for $\overline{D}^0$ mesons from sources that involve higher mass meson resonances. It is clear in the latter two tables that the efficiency depends on the source of the charmed meson. In particular, the acceptance for charmed mesons from higher mass vector meson decay is higher than from direct decays or decays involving even higher mass mesons.

Tables 5.8 and 5.9 show the reconstruction efficiencies for charmed mesons from other sources of the final state mesons.

[1]Four million $\overline{\Lambda}_b^0$ semileptonic decay events were generated to reduce the relatively large Monte Carlo statistical uncertainty.

	Event Yields After Analysis Stages		
	$B^+ \to \overline{D}^0 e^+ \nu_e$ $\to K^+\pi^-$	$B^0 \to D^- e^+ \nu_e$ $\to K^+\pi^-\pi^-$	$B^0 \to D^{*-} e^+ \nu_e$ $\to \overline{D}^0 \pi^-$
$P_T(b) > 9$ GeV/c, $\lvert y\rvert < 1.5$	2 000 000	2 000 000	2 000 000
$P_T(e) > 7.0$ GeV/c	104 801	104 704	141 949
$E_T(e) > 8.0$ GeV, $\lvert\eta\rvert < 1.1$, $N_{trk} = 1$, Fiducial cut	29 598	27 795	37 729
Track requirements, $P_T > 400$ MeV/c (events)	21 921	15 770	15 171
Vertex (candidates)	19 686	14 229	26 001
Track reconstruction	$18\ 164^{+135}_{-271}$	$12\ 476^{+240}_{-440}$	$22\ 356^{+792}_{-1416}$
Selection cuts	4706	2467	3061
L2 trigger	2926^{+55}_{-47}	1562^{+30}_{-25}	2035^{+40}_{-38}
	Acceptances and Efficiencies in Percentages		
	$B^+ \to \overline{D}^0 e^+ \nu_e$ $\to K^+\pi^-$	$B^0 \to D^- e^+ \nu_e$ $\to K^+\pi^-\pi^-$	$B^0 \to D^{*-} e^+ \nu_e$ $\to \overline{D}^0 \pi^-$
Acceptance	1.0961	0.78850	0.75855
Tracking efficiency	92.3 ± 1.4	87.7 ± 3.1	86.0 ± 5.4
L2 trigger efficiency	62.2 ± 1.2	63.3 ± 1.2	66.5 ± 1.3
Acceptance & efficiency	0.1463 ± 0.0044	0.0781 ± 0.0037	0.1018 ± 0.0071
σ(Track)	± 0.0022	± 0.0028	± 0.0064
σ(Trigger)	± 0.0027	± 0.0015	± 0.0020
σ(Stat)	± 0.0027	± 0.0020	± 0.0023

Table 5.4: Acceptances and reconstruction efficiencies for directly-produced charmed hadrons in semileptonic B-hadron decays.

	Event Yields After Analysis Stages	
	$B_s^0 \to D_s^- e^+ \nu_e$ $\to \phi\pi^-$	$\overline{\Lambda}_b^0 \to \Lambda_c^- e^+ \nu_e$ $\to K^+ \overline{p}\pi^-$
$P_T(b) > 9$ GeV/c, $\lvert y\rvert < 1.5$	2 000 000	4 000 000
$P_T(e) > 7.0$ GeV/c	103 078	236 725
$E_T(e) > 8.0$ GeV, $\lvert\eta\rvert < 1.1$, $N_{trk} = 1$, Fiducial cut	25 520	58 020
Track requirements, $P_T > 400$ MeV/c (events)	18 080	37 738
Vertex (candidates)	32 178	67 904
Track reconstruction	$28\ 419^{+402}_{-823}$	$59\ 936^{+966}_{-1916}$
Selection cuts	1648	3693
L2 trigger	1032^{+14}_{-28}	2376^{+37}_{-43}
	Acceptances and Efficiencies in Percentages	
	$B_s^0 \to D_s^- e^+ \nu_e$ $\to \phi\pi^-$	$\overline{\Lambda}_b^0 \to \Lambda_c^- e^+ \nu_e$ $\to K^+ \overline{p}\pi^-$
Acceptance	0.90400	0.94345
Tracking efficiency	88.3 ± 2.6	88.3 ± 2.8
L2 trigger efficiency	62.6 ± 1.7	64.3 ± 1.2
$CL > 0.01$ efficiency		88.2 ± 4.5
dE/dx efficiency		84.135
Acceptance & efficiency	0.0516 ± 0.0026	0.0441 ± 0.0029
σ(Track)	± 0.0015	± 0.0014
σ(Trigger)	± 0.0014	± 0.0008
σ(Stat)	± 0.0016	± 0.0009

Table 5.5: Acceptances and reconstruction efficiencies for directly-produced charmed hadrons in semileptonic B-hadron decays.

	Event Yields After Analysis Stages		
	$B^0 \to D^{*-}e^+\nu_e \to \overline{D}^0$	$B^+ \to D^{*0}e^+\nu_e \to \overline{D}^0$	$B^0 \to D^{**-}e^+\nu_e \to \overline{D}^0$
$P_T(b) > 9$ GeV/c, $\lvert y\rvert < 1.5$	2 000 000	2 000 000	2 000 000
$P_T(e) > 7.0$ GeV/c	141 949	142 987	88 028
$E_T(e) > 8.0$ GeV, $\lvert\eta\rvert < 1.1$, $N_{trk} = 1$, Fiducial cut	37 729	38 538	20 525
Track requirements, $P_T > 400$ MeV/c (events)	27 678	29 056	14 870
Vertex (candidates)	24 984	25 923	13 962
Track reconstruction	$23\ 119^{+143}_{-312}$	$23\ 958^{+155}_{-303}$	$12\ 882^{+89}_{-137}$
Selection cuts	6226	6374	3617
L2 trigger	3958^{+71}_{-65}	4053^{+71}_{-90}	2185^{+37}_{-47}
	Acceptances and Efficiencies in Percentages		
	$B^0 \to D^{*-}e^+\nu_e \to \overline{D}^0$	$B^+ \to D^{*0}e^+\nu_e \to \overline{D}^0$	$B^0 \to D^{**-}e^+\nu_e \to \overline{D}^0$
Acceptance	1.3839	1.4528	0.74350
Tracking efficiency	92.5 ± 1.2	92.4 ± 1.2	92.3 ± 1.0
L2 trigger efficiency	63.6 ± 1.1	63.6 ± 1.4	60.5 ± 1.3
Acceptance & efficiency	0.1979 ± 0.0054	0.2027 ± 0.0061	0.1093 ± 0.0035
σ(Track)	± 0.0027	± 0.0026	± 0.0012
σ(Trigger)	± 0.0036	± 0.0045	± 0.0024
σ(Stat)	± 0.0031	± 0.0032	± 0.0023

Table 5.6: Acceptances and reconstruction efficiencies for $\overline{D}^0$ mesons in semileptonic B-meson decays from higher mass charmed-meson intermediate states.

	Event Yields After Analysis Stages	
	$B^0 \to D^{**-} e^+ \nu_e$ $\to D^{*-} \to \overline{D}^0$	$B_s^0 \to D_s^{**-} e^+ \nu_e$ $\to \overline{D}^0$
$P_T(b) > 9$ GeV/c, $\lvert y \rvert < 1.5$	2 000 000	2 000 000
$P_T(e) > 7.0$ GeV/c	66 556	61 970
$E_T(e) > 8.0$ GeV, $\lvert \eta \rvert < 1.1$, $N_{trk} = 1$, Fiducial cut	15 473	14 158
Track requirements, $P_T > 400$ MeV/c (events)	11 411	10 155
Vertex (candidates)	10 659	9336
Track reconstruction	9822^{+64}_{-123}	8608^{+46}_{-98}
Selection cuts	2643	2392
L2 trigger	1558^{+35}_{-33}	1448^{+35}_{-22}
	Acceptances and Efficiencies in Percentages	
	$B^0 \to D^{**-} e^+ \nu_e$ $\to D^{*-} \to \overline{D}^0$	$B_s^0 \to D_s^{**-} e^+ \nu_e$ $\to \overline{D}^0$
Acceptance	0.57055	0.50775
Tracking efficiency	92.1 ± 1.2	92.2 ± 1.0
L2 trigger efficiency	58.9 ± 1.3	60.5 ± 1.5
Acceptance & efficiency	0.0779 ± 0.0028	0.0724 ± 0.0027
σ(Track)	± 0.0010	± 0.0008
σ(Trigger)	± 0.0018	± 0.0018
σ(Stat)	± 0.0020	± 0.0019

Table 5.7: Acceptances and reconstruction efficiencies for $\overline{D}^0$ mesons in semileptonic B-meson decays from higher mass charmed-meson intermediate states.

	Event Yields After Analysis Stages		
	$B^0 \to D^{*-}e^+\nu_e \to D^-$	$B^+ \to D^{**0}e^+\nu_e \to D^-$	$B_s^0 \to D_s^{**-}e^+\nu_e \to D^-$
$P_T(b) > 9$ GeV/c, $\|y\| < 1.5$	2 000 000	2 000 000	2 000 000
$P_T(e) > 7.0$ GeV/c	142 098	88 566	62 202
$E_T(e) > 8.0$ GeV, $\|\eta\| < 1.1$, $N_{trk} = 1$, Fiducial cut	35 969	19 385	14 127
Track requirements, $P_T > 400$ MeV/c (events)	21 066	12 743	9664
Vertex (candidates)	19 470	20 120	13 287
Track reconstruction	$17\ 143^{+327}_{-629}$	$17\ 644^{+326}_{-657}$	$11\ 645^{+276}_{-542}$
Selection cuts	3263	1772	1139
L2 trigger	2127^{+31}_{-36}	1110^{+29}_{-27}	749^{+17}_{-14}
	Acceptances and Efficiencies in Percentages		
	$B^0 \to D^{*-}e^+\nu_e \to D^-$	$B^0 \to D^{**-}e^+\nu_e \to D^-$	$B_s^0 \to D_s^{**-}e^+\nu_e \to D^-$
Acceptance	1.0533	0.63715	0.4832
Tracking efficiency	88.1 ± 3.2	87.7 ± 3.3	87.6 ± 4.1
L2 trigger efficiency	65.2 ± 1.1	62.6 ± 1.6	65.8 ± 1.5
Acceptance & efficiency	0.1064 ± 0.0049	0.0555 ± 0.0030	0.0375 ± 0.0024
σ(Track)	± 0.0039	± 0.0021	± 0.0017
σ(Trigger)	± 0.0018	± 0.0015	± 0.0009
σ(Stat)	± 0.0023	± 0.0017	± 0.0014

Table 5.8: Acceptances and reconstruction efficiencies for D^- mesons from semileptonic B-meson decays from higher mass charmed-meson intermediate states.

	Event Yields After Analysis Stages		
	$B_s^0 \to D_s^{*-} e^+ \nu_e$ $\to D_s^-$	$B^0 \to D^{**-} e^+ \nu_e$ $\to D^*(2010)^-$	$B_s^0 \to D_s^{**-} e^+ \nu_e$ $\to D^*(2010)^-$
$P_T(b) > 9$ GeV/c, $\lvert y \rvert < 1.5$	2 000 000	2 000 000	2 000 000
$P_T(e) > 7.0$ GeV/c	138 746	66 556	62 069
$E_T(e) > 8.0$ GeV, $\lvert \eta \rvert < 1.1$, $N_{trk} = 1$, Fiducial cut	32 284	15 473	14 866
Track requirements, $P_T > 400$ MeV/c (events)	23 401	7055	8354
Vertex (candidates)	42 011	21 721	23 912
Track reconstruction	$37\ 123^{+518}_{-1112}$	$18\ 558^{+703}_{-1149}$	$20\ 382^{+835}_{1344}$
Selection cuts	2065	1384	1338
L2 trigger	1332^{+24}_{-19}	864^{+13}_{-14}	735^{+14}_{-22}
	Acceptances and Efficiencies in Percentages		
	$B_s^0 \to D_s^{*-} e^+ \nu_e$ $\to D_s^-$	$B^0 \to D^{**-} e^+ \nu_e$ $\to D^*(2010)^-$	$B_s^0 \to D_s^{**-} e^+ \nu_e$ $\to D^*(2010)^-$
Acceptance	1.1701	0.3528	0.4177
Tracking efficiency	88.4 ± 2.6	85.4 ± 5.3	85.2 ± 5.6
L2 trigger efficiency	64.5 ± 1.2	62.4 ± 1.0	64.6 ± 1.9
Acceptance & efficiency	0.0666 ± 0.0030	0.0432 ± 0.0031	0.0368 ± 0.0030
σ(Track)	± 0.0020	± 0.0027	± 0.0024
σ(Trigger)	± 0.0012	± 0.0007	± 0.0011
σ(Stat)	± 0.0018	± 0.0015	± 0.0014

Table 5.9: Acceptances and reconstruction efficiencies for charmed mesons from semileptonic B-meson decays from higher mass charmed-meson intermediate states.

5.3.1 Tracking Efficiency

In this analysis, we have charmed hadrons decaying to two and three charged daughters. For this reason, and because of other topological differences between channels, we must assume that the tracking efficiencies do not cancel between channels. The Run 1 tracking efficiency parametrizations [87] are applied to the Monte Carlo sample before the charmed hadron identification criteria are applied.

5.3.2 L2 Trigger Efficiency

The physics of decays of pseudoscalar mesons to pseudoscalar mesons ($\mathcal{P} \to \mathcal{P}'$) differs from that of pseudoscalars decaying to vector mesons ($\mathcal{P} \to \mathcal{V}$) due to several factors, including the $V-A$ coupling, the quantum numbers of the daughter meson and the q^2 distribution for the decay [55]. As a consequence, the resulting electron P_T distribution for $\mathcal{P} \to \mathcal{V}$ decays is harder than for $\mathcal{P} \to \mathcal{P}'$ decays. For this reason, the Level 2 (L2) trigger efficiency for electrons with E_T near the trigger turn-on threshold does not cancel in this analysis and, hence, must be measured.

A parametrization for the Run 1A L2 inclusive electron trigger efficiency was measured using electron candidates accepted by a trigger with lower E_T and P_T requirements [88, 89]. We use the product of the E_T, P_T and trigger tower crack correction parametrizations in Ref. [89] to represent the Run 1A trigger efficiency. We performed a similar measurement of the Run 1B trigger efficiency [90]. We use the product of the CEM E_T, CFT P_T, XCES E_T and trigger tower crack correction parametrizations to represent the Run 1B trigger efficiency. Since the electron identification plateau efficiencies cancel in this measurement, we set the plateau efficiency at 100%.

The overall Run 1 trigger efficiency to be applied to the Monte Carlo samples is determined as follows. A random number is generated to signify whether or not the event is a Run 1A event or a Run 1B event. The events are expected to occur in a ratio consistent with the ratio of integrated luminosities for the two running periods. If the event is designated a Run 1A event, then the Run 1A efficiency is applied.

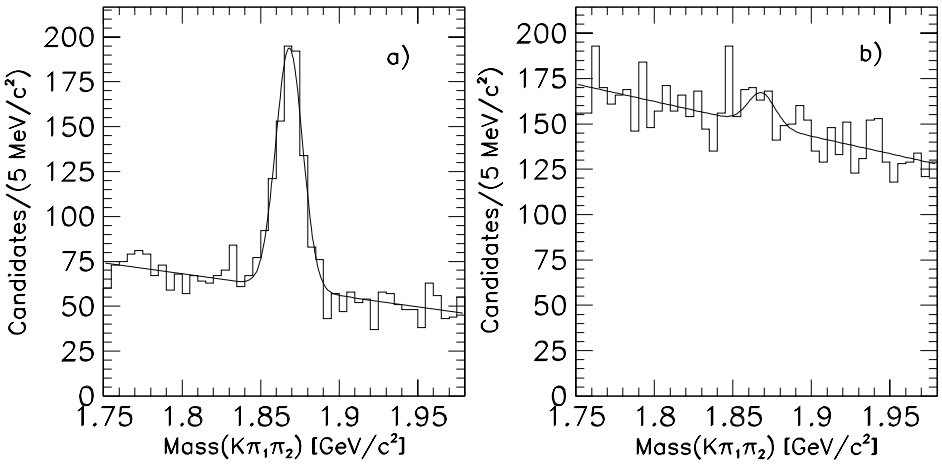

Figure 5.1: Invariant mass distributions of D^- candidates in 110 pb^{-1} of Run 1 inclusive electron data. a) Events that pass the $CL > 0.01$ requirement on the vertex fit. b) Events that fail the $CL > 0.01$ requirement on the vertex fit.

Conversely, if the event is designated a Run 1B event, then the Run 1B efficiency is applied. The overall trigger efficiencies are applied to the Monte Carlo sample after all the other cuts are made.

5.3.3 Vertex Constraint Efficiency

The confidence level requirement of $CL > 0.01$ is applied to the vertex fit in the case of the Λ_c^- vertex to further reduce the large combinatorial backgrounds in this channel. We use the D^- sample to measure the efficiency of the $CL > 0.01$ requirement since the topologies of the D^- and Λ_c^- decays are similar. In both channels, a three-track vertex is fitted and no prior mass constraints are applied (as is the case in the D^{*-} and D_s^- channels).

To measure the efficiency, we first apply all the cuts listed in Section 4.2.3 for the D^- reconstruction. Then we plot the D^- invariant mass for events passing the $CL > 0.01$ requirement and for events failing the requirement, as shown in Figure 5.1. Fitting both of these distributions simultaneously to a Gaussian signal on a linear background, we arrive at an efficiency of $(88.2 \pm 4.5)\%$. We take this to be the efficiency of the $CL > 0.01$ cut in the $\overline{\Lambda}_b^0 \to \Lambda_c^- e^+ \nu_e$ channel.

	Event Yields After Analysis Stages		
	$\epsilon_b = 0.004$	$\epsilon_b = 0.006$	$\epsilon_b = 0.008$
$P_T(b) > 9$ GeV/c, $\|y\| < 1.5$	4 000 000	4 000 000	4 000 000
$P_T(e) > 7.0$ GeV/c	254 565	236 725	224 264
$E_T(e) > 8.0$ GeV, $\|\eta\| < 1.1$, $N_{trk} = 1$, Fiducial cut	62 198	58 020	54 962
Track requirements, $P_T > 400$ MeV/c	40 240	37 738	35 623
	Acceptances in Percentages		
Acceptance	1.006 ± 0.005	0.943 ± 0.005	0.891 ± 0.005

Table 5.10: Acceptance dependence on Peterson fragmentation parameter ϵ_b for semileptonic $\overline{\Lambda}_b^0$ decays.

5.4 Acceptance Dependence on Fragmentation

We use the measured value $\epsilon_b = 0.006 \pm 0.002$ for the Peterson fragmentation parameter (refer to Chapter 1) in our efficiency calculations. We generate Monte Carlo samples using $\epsilon_b = 0.004$ and $\epsilon_b = 0.008$ and use the variation in the acceptance to determine the systematic uncertainty associated with the choice of ϵ_b. The results for the $\overline{\Lambda}_b^0 \to \Lambda_c^- e^+ \nu$ decay are given in Table 5.10. By taking half of the difference between the extremes (i.e., $(1.006 - 0.891)/2 = 0.058$) as a measure of the uncertainty, we obtain an uncertainty of $\sigma = 0.058/0.943 = 6.1\%$. Similar results are obtained for the other decay channels, as shown in Table 5.11. We assume that the Peterson fragmentation parameters for B^0 and B^+ mesons are correlated and therefore any systematic uncertainty associated with ϵ_b cancels in the f_d/f_u ratio. We relax this assumption for B_s^0 mesons and $\overline{\Lambda}_b^0$ baryons and assign a systematic uncertainty accounting for the fact that ϵ_b could be as much as ± 0.002 away from the value for B^+ and B^0 mesons. These uncertainties are listed in the right-hand column of Table 5.11.

Channel	Efficiency in Percentages			Fractional Uncertainty (%)	Assigned Systematic Uncertainty (%)
	$\epsilon_b = 0.004$	$\epsilon_b = 0.008$	Diff/2		
$B^+ \to \overline{D}^0 e^+ \nu_e$	1.185 ± 0.008	1.041 ± 0.007	0.072	± 6.6	± 0.0
$B^0 \to D^- e^+ \nu_e$	0.846 ± 0.006	0.738 ± 0.006	0.054	± 6.8	± 0.0
$B^0 \to D^{*-} e^+ \nu_e$	0.814 ± 0.006	0.717 ± 0.006	0.049	± 6.4	± 0.0
$B_s^0 \to D_s^- e^+ \nu_e$	0.970 ± 0.007	0.854 ± 0.007	0.058	± 6.4	± 6.4
$\overline{\Lambda}_b^0 \to \Lambda_c^- e^+ \nu_e$	1.006 ± 0.005	0.891 ± 0.005	0.058	± 6.1	± 6.1

Table 5.11: Peterson fragmentation parameter systematic uncertainties for semileptonic B-hadron decays.

5.5 $\overline{\Lambda}_b^0$ Polarization

There is no measurement of the $\overline{\Lambda}_b^0$ production polarization in $\overline{p}p$ collisions. Therefore, we calculate the dependence of the $\Lambda_c^- e^+$ reconstruction efficiency on the production polarization.

The angular distribution of the products of the $\overline{\Lambda}_b^0$ decay is parameterized by

$$\frac{dN}{d\cos\theta} \propto 1 + \mathcal{P}\cos\theta,$$

where $\mathcal{P}$ is the $\overline{\Lambda}_b^0$ production polarization times the asymmetry parameter of the weak decay and

$$\cos\theta = \frac{\vec{P}(\Lambda_c^-) \cdot \hat{n}}{|\vec{P}(\Lambda_c^-)|},$$

with momentum $\vec{P}(\Lambda_c^-)$ defined in the $\overline{\Lambda}_b^0$ rest frame and with

$$\hat{n} \equiv \frac{\vec{P}(p) \times \vec{P}(\overline{\Lambda}_b^0)}{|\vec{P}(p) \times \vec{P}(\overline{\Lambda}_b^0)|}$$

representing the polarization axis transverse to the beam proton–$\overline{\Lambda}_b^0$ production plane. We plot the $\cos\theta$ distribution of the events passing the electron acceptance criteria and find the distribution to be relatively flat, as shown in Figure 5.2. Therefore, we conclude that the electron acceptance is largely independent of the $\overline{\Lambda}_b^0$ polarization, and so we consider only the effect of polarization on the reconstruction efficiency of

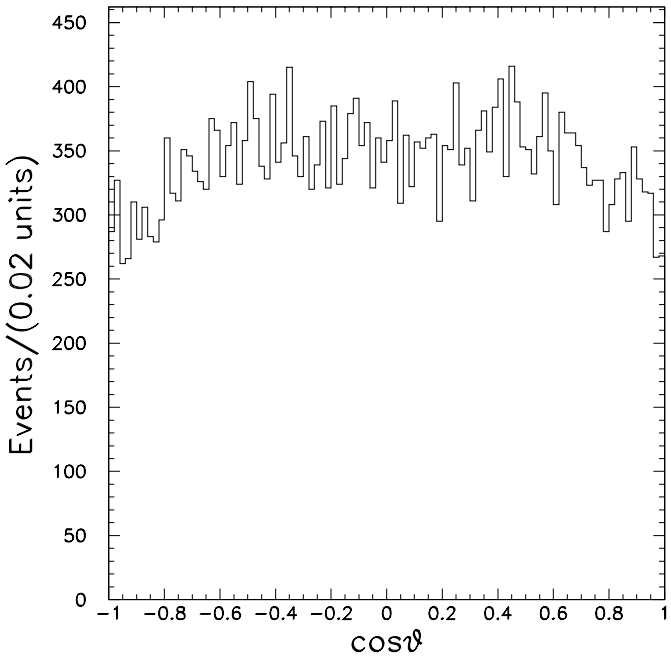

Figure 5.2: Distribution of $\cos\theta$ for Λ_c^- baryons from Λ_b^0 semileptonic decays determined using a Monte Carlo calculation.

the Λ_c^- baryon. We calculate $dN/d\cos\theta$ using different values of $\mathcal{P}$ for the $\overline{\Lambda}_b^0$ Monte Carlo events passing the acceptance cuts. A random number RN is generated and events with $RN < (1+\mathcal{P}\cos\theta)/(1+|\mathcal{P}|)$ are selected (refer to the "Candidates" row in Table 5.12). The reconstruction efficiency (i.e., the number of events passing the selection cuts divided by the number of candidates) as a function of $\mathcal{P}$ is obtained, as shown in Table 5.12.

By taking half of the efficiency difference for a possible polarization times asymmetry spanning the range $-1 < \mathcal{P} < +1$ (i.e., $(4.29 - 4.11)/2 = 0.090$) as a measure of the uncertainty, we obtain a systematic uncertainty of $\sigma = 0.090/4.23 = 2.1\%$.

We note that in this study we have neglected any effect due to the Λ_c^- decay polarization. Since the effects associated with the $\overline{\Lambda}_b^0$ production polarization are so small, we see no reason to believe that a non-vanishing Λ_c^- polarization will significantly increase the systematic uncertainty, particularly since the $\Lambda_c^- \to \overline{p}K^+\pi^-$ process is a three-body decay.

	Event Yields After Analysis Stages		
	$\mathcal{P} = -1.0000$	$\mathcal{P} = 0.0000$	$\mathcal{P} = +1.0000$
Candidates	34 083	67 904	33 912
Track Reconstruction	$30\ 100^{+472}_{-940}$	$59\ 936^{+966}_{-1916}$	$29\ 935^{+505}_{-986}$
Selection Cuts	2285	4459	2150
L2 Trigger	1463^{+24}_{-23}	2874^{+48}_{-50}	1393^{+24}_{-30}
	Efficiencies in Percentages		
	$\mathcal{P} = -1.0000$	$\mathcal{P} = 0.0000$	$\mathcal{P} = +1.0000$
Tracking Efficiency	88.3 ± 2.8	88.3 ± 2.8	88.3 ± 2.9
L2 Trigger Efficiency	64.0 ± 1.1	64.5 ± 1.1	64.8 ± 1.4
Efficiency	4.29 ± 0.19	4.23 ± 0.17	4.11 ± 0.19
σ(Track)	± 0.13	± 0.14	± 0.14
σ(Trigger)	± 0.07	± 0.07	± 0.09
σ(Stat)	± 0.11	± 0.08	± 0.11

Table 5.12: Reconstruction efficiency dependence on $\overline{\Lambda}_b^0$ production polarization times weak decay asymmetry $\mathcal{P}$.

5.6 Systematic Uncertainties

The systematic uncertainties associated with event reconstruction are summarized in Table 5.13. The uncertainty in the two-track tracking efficiency cancels in the calculation of the ratios of fragmentation fractions, therefore, we neglect the tracking uncertainty in the $\overline{D}^0 \to K^+\pi^-$ reconstruction and subtract that uncertainty from the uncertainties in the other decay channels. For the trigger efficiencies, only the differences in the uncertainties for each channel survive in the ratio calculation. The fractional uncertainties vary from 1.7% to 2.7%, therefore, we assign a 1.0% systematic uncertainty in the trigger efficiency to all decay channels. The total systematic uncertainty is the sum in quadrature of the individual uncertainties for each decay channel.

	Fractional Systematic Uncertainties in Percentages		
	$B^+ \to \overline{D}^0 e^+ \nu_e$ $\to K^+ \pi^-$	$B^0 \to D^- e^+ \nu_e$ $\to K^+ \pi^- \pi^-$	$B^0 \to D^{*-} e^+ \nu_e$ $\to \overline{D}^0 \pi^-$
Track Reconstruction	± 0.0	± 2.0	± 4.8
L2 Trigger	± 1.0	± 1.0	± 1.0
MC Statistics	± 1.8	± 2.5	± 2.2
ϵ_b	± 0.0	± 0.0	± 0.0
Total	± 2.1	± 3.4	± 5.4

	$B_s^0 \to D_s^- e^+ \nu_e$ $\to \phi \pi^-$	$\overline{\Lambda}_b^0 \to \Lambda_c^- e^+ \nu_e$ $\to K^+ \overline{p} \pi^-$
Track Reconstruction	± 1.4	± 1.7
L2 Trigger	± 1.0	± 1.0
MC Statistics	± 3.1	± 1.9
ϵ_b	± 6.4	± 6.1
$CL > 0.01$		± 5.1
$\overline{\Lambda}_b^0$ Polarization		± 2.1
Total	± 7.3	± 8.7

Table 5.13: Fractional systematic uncertainties, quoted in percentages, associated with an estimate of the event reconstruction efficiencies.

Chapter 6

Results

6.1 Fragmentation Fraction Fitting Program

6.1.1 Structure of the Fit

In order to determine the fragmentation fractions taking into account the cross contamination and feed-down that occurs due to the decay of B mesons into excited charmed hadrons, we fit the five observed event yields and their uncertainties to the three ratios of fragmentation fractions, taking into account the relative production of the different charmed meson species and their different detection efficiencies. We formulate the problem by defining a χ^2 function comparing the predicted with observed event yields, and including terms to accommodate the additional constraints discussed below.

The MINUIT fitting program [91] is used to perform a least-squares fit to the free parameters. The primary quantities of interest are the three ratios of fragmentation fractions, which we have expressed as

- f_d/f_u,
- $f_s/(f_u + f_d)$, and
- $f_{baryon}/(f_u + f_d)$.

The fit uses these to predict the relative number of B hadron species that are produced and that then decay via various channels into the final states we observe.

We identify for each of the five electron-charm final states the various decay channels that contribute to the given final state according to Tables 5.1, 5.2 and 5.3. We assume separate branching fractions for the B^+ and B^0 mesons, as described in Section 5.1 with the g_0, g_+, g_0^*, and g_+^* constrained to the measured values listed in Tables 5.1, 5.2 and 5.3. The branching fractions g_s and g_s^* are constrained to the values determined using the spectator quark model (also listed in Tables 5.1, 5.2 and 5.3). We constrain in the fit the three branching fractions, g, g^*, and g^{**} for each B-meson species to sum to the total semileptonic branching fractions listed in Tables 5.1, 5.2 and 5.3.

These constraints are taken into account by introducing into our fit as free parameters the nine branching fractions

- g_0, g_0^*, g_0^{**} for B^0 mesons,
- g_+, g_+^*, g_+^{**} for B^+ mesons,
- g_s, g_s^*, g_s^{**} for B_s^0 mesons,

and adding χ^2 terms of the form

$$\Delta\chi^2 = \left(\frac{g_{fit} - g_{PDG}}{\sigma_{PDG}}\right)^2 \tag{6.1}$$

for each g and g^*, where g_{fit} is the fit parameter, g_{PDG} is the world average value and σ_{PDG} is the uncertainty on the world average value. Each of the sums of the three branching fractions is also constrained by a similar χ^2 term. We include in the fit the number of produced B^+ mesons, $N(B^+)$, as a normalization term.

The observed event yields and their uncertainties are then fit to the predicted event yields, taking into account the contributions from each channel, and properly accounting for the total acceptance and efficiency for each channel.

6.1.2 Systematic Uncertainties

The simultaneous fit includes the various sources of systematic uncertainty on the predicted event yields in the different channels. The total uncertainty on the different channel acceptances and efficiencies are included for each channel by introducing an uncertainty in the predicted event yield for the given channel. These uncertainties are listed in Table 5.13. They include the Monte Carlo statistical uncertainty, the uncertainty in the tracking efficiency, the uncertainty in the trigger efficiency, the uncertainty associated with varying the Peterson parameter ϵ_b, the uncertainty in the Λ_c^- vertex confidence-level cut and the uncertainty associated with varying the $\overline{\Lambda}_b^0$ production polarization.

The predicted event yields also incorporate additional uncertainties resulting from the uncertainties in the daughter meson branching fractions. We use the world average values [49]

$$\begin{aligned}
\mathcal{B}(\overline{D}^0 \to K^+\pi^-) &= (3.85 \pm 0.09)\%, \\
\mathcal{B}(D^- \to K^+\pi^-\pi^-) &= (9.0 \pm 0.6)\%, \\
\mathcal{B}(D^{*-} \to \overline{D}^0\pi^-) &= (68.3 \pm 1.4)\%, \\
\mathcal{B}(\phi \to K^+K^-) &= (49.1 \pm 0.8)\%.
\end{aligned}$$

6.2 Determination of f_d/f_u

The fit prefers the values shown in Table 6.1 for the free parameters. Table 6.2 compares the fitted values for the semileptonic branching fractions to the measured values to which they are constrained. The fitted total semileptonic branching fractions g^{tot} are obtained from the sum of the exclusive semileptonic branching fractions for each B meson species.

The measurement of the ratio of f_d and f_u is an interesting one since it is normally impossible to do without making certain model-dependent assumptions. Previous measurements have either used predicted branching fractions or the total semileptonic

Parameter	Fitted Value
f_d/f_u	$(88 \pm 21)\%$
$f_s/(f_u + f_d)$	$(21.5 \pm 7.1)\%$
$f_{baryon}/(f_u + f_d)$	$(12.0 \pm 4.2)\%$
$N(B^+)$	$(2.0 \pm 0.3) \times 10^8$
g_+	$(1.85 \pm 0.17)\%$
g_0	$(2.03 \pm 0.24)\%$
g_s	$(1.87 \pm 0.21)\%$
g_+^*	$(5.22 \pm 0.77)\%$
g_0^*	$(4.58 \pm 0.27)\%$
g_s^*	$(4.48 \pm 0.33)\%$
g_+^{**}	$(3.39 \pm 0.87)\%$
g_0^{**}	$(3.84 \pm 0.42)\%$
g_s^{**}	$(3.65 \pm 0.64)\%$

Table 6.1: Results from the MINUIT least-squares fit to the free parameters.

Parameter	Input Value (%)	Fitted Value (%)
g_+	1.86 ± 0.33	1.85 ± 0.17
g_0	2.00 ± 0.25	2.03 ± 0.24
g_s	1.87 ± 0.21	1.87 ± 0.21
g_+^*	5.3 ± 0.8	5.22 ± 0.77
g_0^*	4.60 ± 0.27	4.58 ± 0.27
g_s^*	4.48 ± 0.33	4.48 ± 0.33
g_+^{tot}	10.45 ± 0.21	10.45 ± 1.17
g_0^{tot}	10.45 ± 0.21	10.45 ± 0.55
g_s^{tot}	10.0 ± 0.5	10.00 ± 0.75

Table 6.2: Comparison of results from the MINUIT least-squares fit for the semileptonic branching fractions to the measured values to which they are constrained. The fitted total semileptonic branching fractions g^{tot} are obtained from the sum of the exclusive semileptonic branching fractions for each B meson species.

branching fractions to determine this ratio. In our study, although we suffer from large cross-contamination in the final states that are sensitive to these two fractions, we can determine this ratio in part as a new measurement, and in part as a cross-check of our fitting techniques and method.

We find that the fit results in a value of

$$\frac{f_d}{f_u} = (88 \pm 21)\%, \tag{6.2}$$

where the uncertainty includes the statistical uncertainty on the event yields, the uncertainties on the reconstruction efficiencies and the uncertainties on all of the daughter branching fractions. The fact that the result is within one standard deviation of the expected value of unity gives us some confidence in the method we are using to derive $f_s/(f_u + f_d)$ and $f_{baryon}/(f_u + f_d)$.

As a cross-check, we use our fitting routine to determine the ratios of $\overline{D}^0$, D^- and D^{*-} production in semileptonic decays to electrons. We find the following ratios:

$$\begin{aligned} \frac{N(\overline{D}^0)}{N(\overline{D}^0) + N(D^-)} &= 0.75 \pm 0.01, \\ \frac{N(D^{*-})}{N(\overline{D}^0)} &= 0.37 \pm 0.01. \end{aligned}$$

These ratios are obtained by assuming the fitted values for the fragmentation fractions and the semileptonic decay branching fractions. We compare these to the ratios obtained using the world average values

$$\begin{aligned} \mathcal{B}(\overline{b} \to \overline{D}^0 e^+ X) &= (6.5 \pm 0.6)\%, \\ \mathcal{B}(\overline{b} \to D^- e^+ X) &= (2.02 \pm 0.29)\%, \text{ and} \\ \mathcal{B}(\overline{b} \to D^{*-} e^+ X) &= (2.76 \pm 0.29)\%. \end{aligned}$$

They are

$$\frac{N(\overline{D}^0)}{N(\overline{D}^0)+N(D^-)} = 0.76 \pm 0.03$$

$$\frac{N(D^{*-})}{N(\overline{D}^0)} = 0.42 \pm 0.06.$$

We find a D^{*-} fraction that is lower by about one standard deviation than the value predicted by previous measurements. This is consistent with our lower measured f_d/f_u ratio.

6.3 Measurement of $f_s/(f_u + f_d)$

Fitting to the observed yields results in the value

$$\frac{f_s}{f_u+f_d} \times \mathcal{B}(D_s^- \to \phi\pi^-) = 0.00772 \pm 0.00170, \tag{6.3}$$

where the uncertainty includes the statistical uncertainty on the event yields, the uncertainties on the reconstruction efficiencies and the uncertainties on all the branching fractions except $\mathcal{B}(D_s^- \to \phi\pi^-)$. Using $\mathcal{B}(D_s^- \to \phi\pi^-) = (3.6 \pm 0.9)\%$, we obtain

$$\frac{f_s}{f_u+f_d} = (21.5 \pm 4.7 \pm 5.4)\%, \tag{6.4}$$

where the first uncertainty includes the uncertainties listed above. The second uncertainty arises from the uncertainty on the $D_s^- \to \phi\pi^-$ branching fraction.

We can also make this measurement assuming $f_u \equiv f_d$, a typical assumption based on isospin symmetry. We do this by fixing $f_d/f_u \equiv 1$ in the fit. The results are

$$\frac{f_s}{f_u+f_d} \times \mathcal{B}(D_s^- \to \phi\pi^-) = 0.00782 \pm 0.00166, \tag{6.5}$$

and

$$\frac{f_s}{f_u + f_d} = (21.7 \pm 4.6 \pm 5.4)\%. \quad (6.6)$$

This illustrates that most of the uncertainty on this result comes from the statistical uncertainty on the number of reconstructed B_s^0 mesons and the uncertainty on $\mathcal{B}(D_s^- \to \phi\pi^-)$.

6.4 Measurement of $f_{baryon}/(f_u + f_d)$

Fitting to the observed yields results in the value

$$\frac{f_{baryon}}{f_u + f_d} \times \mathcal{B}(\Lambda_c^- \to \overline{p}K^+\pi^-) = 0.00599 \pm 0.00144, \quad (6.7)$$

where the uncertainty includes the statistical uncertainty on the event yields, the uncertainties on the reconstruction efficiencies and the uncertainties on all the branching fractions except $\mathcal{B}(\Lambda_c^- \to \overline{p}K^+\pi^-)$. Using $\mathcal{B}(\Lambda_c^- \to \overline{p}K^+\pi^-) = (5.0 \pm 1.3)\%$, we obtain

$$\frac{f_{baryon}}{f_u + f_d} = (12.0 \pm 2.9 \pm 3.1)\%, \quad (6.8)$$

where the first uncertainty includes the uncertainties listed above. The second uncertainty arises from the uncertainty on the $\Lambda_c^- \to \overline{p}K^+\pi^-$ branching fraction.

We can also make this measurement assuming $f_u \equiv f_d$, which results in the values

$$\frac{f_{baryon}}{f_u + f_d} \times \mathcal{B}(\Lambda_c^- \to \overline{p}K^+\pi^-) = 0.00605 \pm 0.00145, \quad (6.9)$$

and

$$\frac{f_{baryon}}{f_u + f_d} = (12.1 \pm 2.9 \pm 3.1)\%. \quad (6.10)$$

6.5 Absolute Fragmentation Fraction Values

We can determine the absolute fragmentation fraction values from our fits by assuming that the B^0, B^+, B_s^0 and $\overline{\Lambda}_b^0$ hadrons saturate the b-quark production rate[1], i.e.,

$$f_u + f_d + f_s + f_{baryon} \equiv 1 \tag{6.11}$$

$$\Rightarrow 1 + \frac{f_d}{f_u} + \frac{f_s}{f_u} + \frac{f_{baryon}}{f_u} = \frac{1}{f_u}. \tag{6.12}$$

We can relate the ratios on the left-hand side to our fit parameters using the relationships

$$\frac{f_s}{f_u + f_d} = \frac{f_s}{f_u}\left(\frac{1}{1+\frac{f_d}{f_u}}\right) \tag{6.13}$$

$$\Rightarrow \frac{f_s}{f_u} = \frac{f_s}{f_u + f_d}\left(1 + \frac{f_d}{f_u}\right). \tag{6.14}$$

The right-hand side in Equation 6.14 now includes the parameters determined in our fit. Similar relationships are obtained for the ratio f_{baryon}/f_u.

If we denote our fit parameters as

$$\beta_1 \equiv \frac{f_d}{f_u} \tag{6.15}$$

$$\beta_2 \equiv \frac{f_s}{f_u + f_d} \text{ and} \tag{6.16}$$

$$\beta_3 \equiv \frac{f_{baryon}}{f_u + f_d}, \tag{6.17}$$

and the ratios of fragmentation fractions as

$$\alpha_1 \equiv \frac{f_d}{f_u} = \beta_1 \tag{6.18}$$

$$\alpha_2 \equiv \frac{f_s}{f_u} = \beta_2(1 + \beta_1) \text{ and} \tag{6.19}$$

[1]This is a reasonable assumption in that the B_c meson production is known to be very small and the bottom-strange baryon production cross section is expected to be significantly smaller than the cross section for $\overline{\Lambda}_b^0$ production.

$$\alpha_3 \equiv \frac{f_{baryon}}{f_u} = \beta_3(1+\beta_1), \tag{6.20}$$

then the normalization relationship is

$$1+\alpha_1+\alpha_2+\alpha_3 = \frac{1}{f_u} \tag{6.21}$$

$$\Rightarrow f_u = \frac{1}{1+\alpha_1+\alpha_2+\alpha_3} \tag{6.22}$$

$$= \frac{1}{1+\beta_1+(\beta_2+\beta_3)(1+\beta_1)}. \tag{6.23}$$

This normalization relation could be employed regardless of what value we expect the four fragmentation fractions to sum to. However, the natural assumption is that they would sum to unity, and that is the assumption we make for the rest of this discussion.

With the relationship between the f_i and the fit parameters β_j, we can also calculate the uncertainties on the fragmentation fractions using the covariance matrix resulting from the simultaneous fit and the standard relationship

$$V^f_{nm} = \frac{\partial f_n}{\partial \beta_i}\frac{\partial f_m}{\partial \beta_j} V^\beta_{ij}, \tag{6.24}$$

where V^f_{nm} and V^β_{ij} are the covariance matrices for the four parameters $\{f_u, f_d, f_s, f_{baryon}\}$ and the fit parameters $\{\beta_1, \beta_2, \beta_3\}$, respectively. The diagonal elements of V^f_{nm} represent the uncertainties (squared) on the absolute fragmentation fractions.

This set of calculations results in the following values:

$$f_u = (39.8 \pm 5.4)\%, \tag{6.25}$$

$$f_d = (35.2 \pm 4.8)\%, \tag{6.26}$$

$$f_s = (16.1 \pm 4.5)\%, \tag{6.27}$$

$$f_{baryon} = (9.0 \pm 2.9)\%. \tag{6.28}$$

We can also make this measurement assuming $f_u \equiv f_d$, which results in the

following values:

$$f_u = (37.4 \pm 2.4)\%, \tag{6.29}$$

$$f_d = (37.4 \pm 2.4)\%, \tag{6.30}$$

$$f_s = (16.2 \pm 4.5)\%, \tag{6.31}$$

$$f_{baryon} = (9.0 \pm 2.9)\%. \tag{6.32}$$

Chapter 7

Conclusions

We have measured the b-quark fragmentation fractions in 1.8-TeV proton-antiproton collisions using the CDF detector. We have analyzed 110 pb^{-1} of $\overline{p}p$ data and identified the following semileptonic B hadron decays into electrons and charmed hadrons: $B^+ \to e^+\nu_e\overline{D}^0 X$, $B^0 \to e^+\nu_e D^{*-} X$, $B^0 \to e^+\nu_e D^- X$, $B_s^0 \to e^+\nu_e D_s^- X$ and $\overline{\Lambda}_b^0 \to e^+\nu_e \Lambda_c^- X$.

With these data, we measure the ratios of fragmentation fractions

$$\begin{aligned} f_d/f_u &= (88 \pm 21)\%, \\ f_s/(f_u + f_d) &= (21.5 \pm 7.1)\% \text{ and} \\ f_{baryon}/(f_u + f_d) &= (12.0 \pm 4.2)\%. \end{aligned}$$

The uncertainties in the $f_s/(f_u + f_d)$ and $f_{baryon}/(f_u + f_d)$ fragmentation fractions are dominated by the uncertainties in the corresponding charmed hadron branching fractions and by the statistical precision in the B_s^0 and $\overline{\Lambda}_b^0$ semileptonic decay yields.

Figure 7.1 compares the measured value of f_d/f_u to other existing measurements. Although our result for f_d/f_u is not as precise as obtained by others, it is based on different assumptions and is consistent with those obtained in e^+e^- collisions. Our measurement of $f_s/(f_u + f_d)$ is in good agreement with that obtained using sequential semimuonic decays in $\overline{p}p$ collisions, although our statistical and systematic uncertainties are slightly larger.

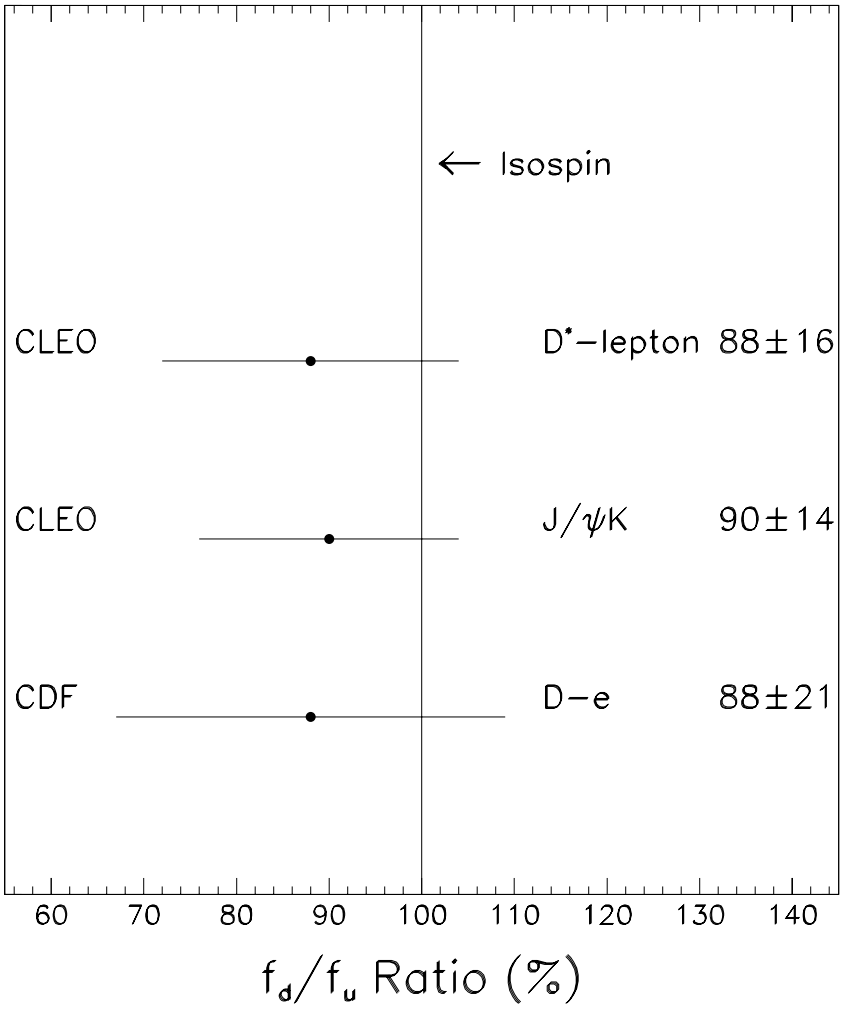

Figure 7.1: Comparison of the measured f_d/f_u ratio to other measurements described in Section 1.3.3.

Assuming $f_u + f_d + f_s + f_{baryon} \equiv 1$, we determine

$$\begin{aligned} f_u &= (39.8 \pm 5.4)\%, \\ f_d &= (35.2 \pm 4.8)\%, \\ f_s &= (16.1 \pm 4.5)\% \text{ and} \\ f_{baryon} &= (9.0 \pm 2.9)\%. \end{aligned}$$

The measured values for f_s and f_{baryon} are relatively insensitive to the f_d/f_u ratio. Figures 7.2 and 7.3 compare the measured values of f_s and f_{baryon} to other existing measurements. The measurement we obtain for f_s is competitive with similar semileptonic studies but is not as well constrained as the result obtained by inference from $B\overline{B}$ mixing measurements. The f_{baryon} result is measured with a similar precision to current LEP measurements.

All four fragmentation fractions are in agreement with previous theoretical and phenomenological interpretations, although the result for f_s is one standard deviation higher than the current world average value. It is possible, *a priori*, that different fragmentation fractions may arise in different b-quark production processes. However, the precision of the present measurements is only sufficient to exclude the existence of a large topology dependence.

These values for the fragmentation fractions constrain the CKM matrix elements V_{cb} and V_{ub} and the $B\overline{B}$ mixing parameters Δm_d and Δm_s. Other B physics quantities, such as B hadron lifetime and decay branching fractions, depend on the fragmentation fractions and can be updated to incorporate these new results.

7.1 Future Prospects

The Tevatron is currently being upgraded to provide instantaneous luminosities of up to 2×10^{32} cm^{-2}s^{-1}. Run 2 of the Tevatron, scheduled to begin in 2000, is expected to produce an integrated luminosity of 2 fb^{-1} of proton-antiproton collision data. The factor of twenty increase in statistics will allow much higher statistical precision for

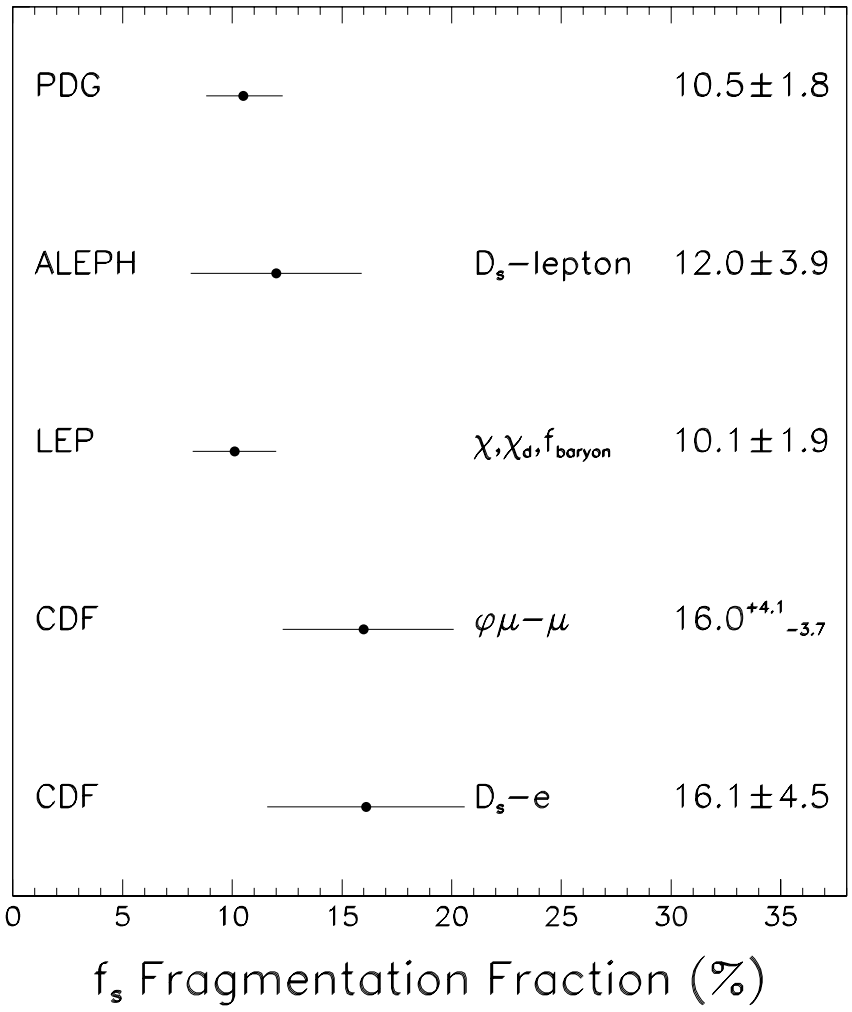

Figure 7.2: Comparison of the measured value for f_s to other measurements described in Section 1.3.3. The CDF $\phi\mu-\mu$ result for f_s is obtained by multiplying the $f_s/(f_u+f_d)$ result in Equation 1.13 by f_u+f_d, where the world average values $f_u = f_d = 39.7\%$ are used. The CDF $D_s - e$ result is the measurement presented in this thesis.

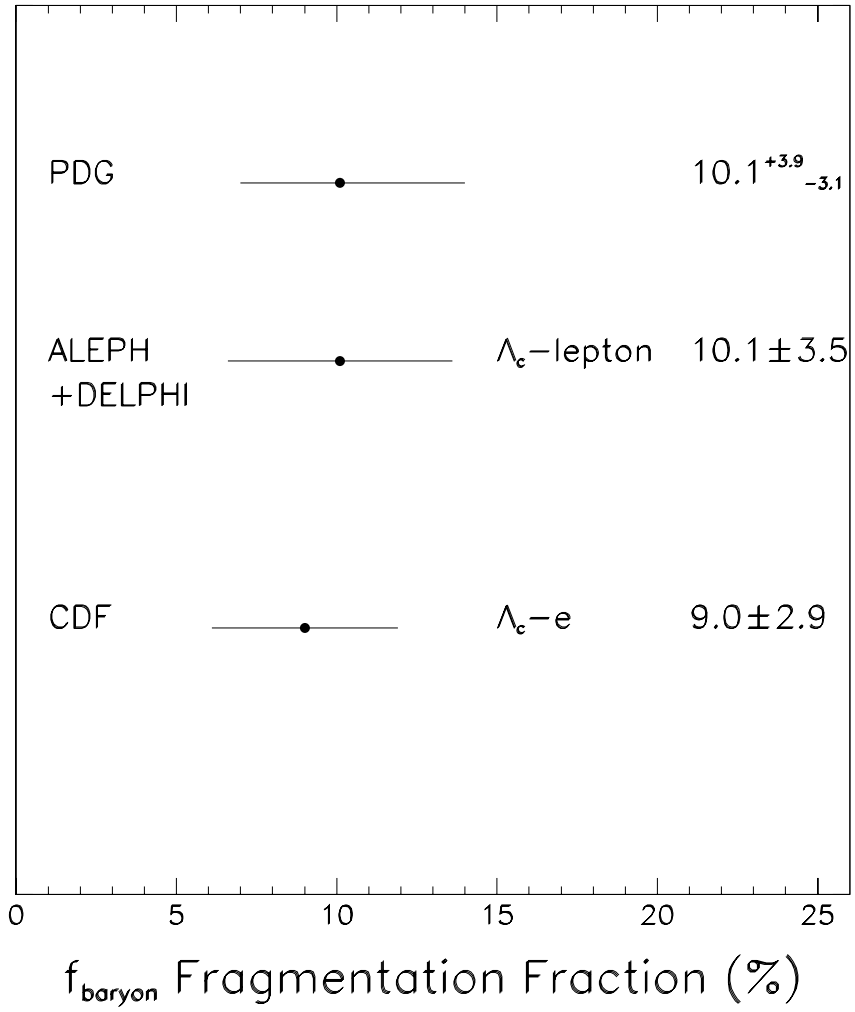

Figure 7.3: Comparison of the measured value for f_{baryon} to other measurements described in Section 1.3.3.

future measurements of the b quark fragmentation fractions. We note, however, that a similar measurement of the b quark fragmentation fractions in Run 2 would be subject to the same systematic uncertainties. Better measured values of the $D_s^- \to \phi\pi^-$ and $\Lambda_c^- \to \overline{p}K^+\pi^-$ branching fractions would be helpful for reducing these systematic uncertainties.

Appendix A

The CDF Collaboration

F. Abe,[17] H. Akimoto,[39] A. Akopian,[31] M. G. Albrow,[7] S. R. Amendolia,[27] D. Amidei,[20] J. Antos,[33] S. Aota,[37] G. Apollinari,[31] T. Arisawa,[39] T. Asakawa,[37] W. Ashmanskas,[5] M. Atac,[7] P. Azzi-Bacchetta,[25] N. Bacchetta,[25] S. Bagdasarov,[31] M. W. Bailey,[22] P. de Barbaro,[30] A. Barbaro-Galtieri,[18] V. E. Barnes,[29] B. A. Barnett,[15] M. Barone,[9] G. Bauer,[19] T. Baumann,[11] F. Bedeschi,[27] S. Behrends,[3] S. Belforte,[27] G. Bellettini,[27] J. Bellinger,[40] D. Benjamin,[35] J. Bensinger,[3] A. Beretvas,[7] J. P. Berge,[7] J. Berryhill,[5] S. Bertolucci,[9] S. Bettelli,[27] B. Bevensee,[26] A. Bhatti,[31] K. Biery,[7] C. Bigongiari,[27] M. Binkley,[7] D. Bisello,[25] R. E. Blair,[1] C. Blocker,[3] K. Bloom,[20] S. Blusk,[30] A. Bodek,[30] W. Bokhari,[26] G. Bolla,[29] Y. Bonushkin,[4] D. Bortoletto,[29] J. Boudreau,[28] A. Brandl,[22] L. Breccia,[2] C. Bromberg,[21] N. Bruner,[22] R. Brunetti,[2] E. Buckley-Geer,[7] H. S. Budd,[30] K. Burkett,[11] G. Busetto,[25] A. Byon-Wagner,[7] K. L. Byrum,[1] M. Campbell,[20] A. Caner,[27] W. Carithers,[18] D. Carlsmith,[40] J. Cassada,[30] A. Castro,[25] D. Cauz,[36] A. Cerri,[27] P. S. Chang,[33] P. T. Chang,[33] H. Y. Chao,[33] J. Chapman,[20] M. -T. Cheng,[33] M. Chertok,[34] G. Chiarelli,[27] C. N. Chiou,[33] F. Chlebana,[7] L. Christofek,[13] R. Cropp,[14] M. L. Chu,[33] S. Cihangir,[7] A. G. Clark,[10] M. Cobal,[27] E. Cocca,[27] M. Contreras,[5] J. Conway,[32] J. Cooper,[7] M. Cordelli,[9] D. Costanzo,[27] C. Couyoumtzelis,[10] D. Cronin-Hennessy,[6] R. Culbertson,[5] D. Dagenhart,[38] T. Daniels,[19] F. DeJongh,[7] S. Dell'Agnello,[9] M. Dell'Orso,[27] R. Demina,[7] L. Demortier,[31] M. Deninno,[2]

P. F. Derwent,[7] T. Devlin,[32] J. R. Dittmann,[6] S. Donati,[27] J. Done,[34] T. Dorigo,[25] N. Eddy,[13] K. Einsweiler,[18] J. E. Elias,[7] R. Ely,[18] E. Engels, Jr.,[28] W. Erdmann,[7] D. Errede,[13] S. Errede,[13] Q. Fan,[30] R. G. Feild,[41] Z. Feng,[15] C. Ferretti,[27] I. Fiori,[2] B. Flaugher,[7] G. W. Foster,[7] M. Franklin,[11] J. Freeman,[7] J. Friedman,[19] H. Frisch,[5] Y. Fukui,[17] S. Gadomski,[14] S. Galeotti,[27] M. Gallinaro,[26] O. Ganel,[35] M. Garcia-Sciveres,[18] A. F. Garfinkel,[29] C. Gay,[41] S. Geer,[7] D. W. Gerdes,[20] P. Giannetti,[27] N. Giokaris,[31] P. Giromini,[9] G. Giusti,[27] M. Gold,[22] A. Gordon,[11] A. T. Goshaw,[6] Y. Gotra,[28] K. Goulianos,[31] H. Grassmann,[36] C. Green,[29] L. Groer,[32] C. Grosso-Pilcher,[5] G. Guillian,[20] J. Guimaraes da Costa,[15] R. S. Guo,[33] C. Haber,[18] E. Hafen,[19] S. R. Hahn,[7] R. Hamilton,[11] T. Handa,[12] R. Handler,[40] W. Hao,[35] F. Happacher,[9] K. Hara,[37] A. D. Hardman,[29] R. M. Harris,[7] F. Hartmann,[16] J. Hauser,[4] E. Hayashi,[37] J. Heinrich,[26] A. Heiss,[16] B. Hinrichsen,[14] K. D. Hoffman,[29] C. Holck,[26] R. Hollebeek,[26] L. Holloway,[13] Z. Huang,[20] B. T. Huffman,[28] R. Hughes,[23] J. Huston,[21] J. Huth,[11] H. Ikeda,[37] M. Incagli,[27] J. Incandela,[7] G. Introzzi,[27] J. Iwai,[39] Y. Iwata,[12] E. James,[20] H. Jensen,[7] U. Joshi,[7] E. Kajfasz,[25] H. Kambara,[10] T. Kamon,[34] T. Kaneko,[37] K. Karr,[38] H. Kasha,[41] Y. Kato,[24] T. A. Keaffaber,[29] K. Kelley,[19] M. Kelly,[20] R. D. Kennedy,[7] R. Kephart,[7] D. Kestenbaum,[11] D. Khazins,[6] T. Kikuchi,[37] M. Kirk,[3] B. J. Kim,[27] H. S. Kim,[14] S. H. Kim,[37] Y. K. Kim,[18] L. Kirsch,[3] S. Klimenko,[8] D. Knoblauch,[16] P. Koehn,[23] A. Köngeter,[16] K. Kondo,[37] J. Konigsberg,[8] K. Kordas,[14] A. Korytov,[8] E. Kovacs,[1] W. Kowald,[6] J. Kroll,[26] M. Kruse,[30] S. E. Kuhlmann,[1] E. Kuns,[32] K. Kurino,[12] T. Kuwabara,[37] A. T. Laasanen,[29] S. Lami,[27] S. Lammel,[7] J. I. Lamoureux,[3] M. Lancaster,[18] M. Lanzoni,[27] G. Latino,[27] T. LeCompte,[1] S. Leone,[27] J. D. Lewis,[7] M. Lindgren,[4] T. M. Liss,[13] J. B. Liu,[30] Y. C. Liu,[33] N. Lockyer,[26] O. Long,[26] M. Loreti,[25] D. Lucchesi,[27] P. Lukens,[7] S. Lusin,[40] J. Lys,[18] K. Maeshima,[7] P. Maksimovic,[11] M. Mangano,[27] M. Mariotti,[25] J. P. Marriner,[7] G. Martignon,[25] A. Martin,[41] J. A. J. Matthews,[22] P. Mazzanti,[2] K. McFarland,[30] P. McIntyre,[34] P. Melese,[31] M. Menguzzato,[25] A. Menzione,[27] E. Meschi,[27] S. Metzler,[26] C. Miao,[20] T. Miao,[7] G. Michail,[11] R. Miller,[21] H. Minato,[37] S. Miscetti,[9] M. Mishina,[17] S. Miyashita,[37] N. Moggi,[27] E. Moore,[22] Y. Morita,[17] A. Mukherjee,[7] T. Muller,[16] A. Munar,[27] P. Murat,[27] S. Murgia,[21] M. Musy,[36]

H. Nakada,[37] T. Nakaya,[5] I. Nakano,[12] C. Nelson,[7] D. Neuberger,[16] C. Newman-Holmes,[7] C.-Y. P. Ngan,[19] H. Niu,[3] L. Nodulman,[1] A. Nomerotski,[8] S. H. Oh,[6] T. Ohmoto,[12] T. Ohsugi,[12] R. Oishi,[37] M. Okabe,[37] T. Okusawa,[24] J. Olsen,[40] C. Pagliarone,[27] R. Paoletti,[27] V. Papadimitriou,[35] S. P. Pappas,[41] N. Parashar,[27] A. Parri,[9] D. Partos,[3] J. Patrick,[7] G. Pauletta,[36] M. Paulini,[18] A. Perazzo,[27] L. Pescara,[25] M. D. Peters,[18] T. J. Phillips,[6] G. Piacentino,[27] M. Pillai,[30] K. T. Pitts,[7] R. Plunkett,[7] A. Pompos,[29] L. Pondrom,[40] J. Proudfoot,[1] F. Ptohos,[11] G. Punzi,[27] K. Ragan,[14] D. Reher,[18] M. Reischl,[16] A. Ribon,[25] F. Rimondi,[2] L. Ristori,[27] W. J. Robertson,[6] A. Robinson,[14] T. Rodrigo,[27] S. Rolli,[38] L. Rosenson,[19] R. Roser,[13] T. Saab,[14] W. K. Sakumoto,[30] D. Saltzberg,[4] A. Sansoni,[9] L. Santi,[36] H. Sato,[37] P. Schlabach,[7] E. E. Schmidt,[7] M. P. Schmidt,[41] A. Scott,[4] A. Scribano,[27] S. Segler,[7] S. Seidel,[22] Y. Seiya,[37] F. Semeria,[2] T. Shah,[19] M. D. Shapiro,[18] N. M. Shaw,[29] P. F. Shepard,[28] T. Shibayama,[37] M. Shimojima,[37] M. Shochet,[5] J. Siegrist,[18] A. Sill,[35] P. Sinervo,[14] P. Singh,[13] K. Sliwa,[38] C. Smith,[15] F. D. Snider,[7] J. Spalding,[7] T. Speer,[10] P. Sphicas,[19] F. Spinella,[27] M. Spiropulu,[11] L. Spiegel,[7] L. Stanco,[25] J. Steele,[40] A. Stefanini,[27] R. Ströhmer,[7] J. Strologas,[13] F. Strumia, [10] D. Stuart,[7] K. Sumorok,[19] J. Suzuki,[37] T. Suzuki,[37] T. Takahashi,[24] T. Takano,[24] R. Takashima,[12] K. Takikawa,[37] M. Tanaka,[37] B. Tannenbaum,[4] F. Tartarelli,[27] W. Taylor,[14] M. Tecchio,[20] P. K. Teng,[33] Y. Teramoto,[24] K. Terashi,[37] S. Tether,[19] D. Theriot,[7] T. L. Thomas,[22] R. Thurman-Keup,[1] M. Timko,[38] P. Tipton,[30] A. Titov,[31] S. Tkaczyk,[7] D. Toback,[5] K. Tollefson,[30] A. Tollestrup,[7] H. Toyoda,[24] W. Trischuk,[14] J. F. de Troconiz,[11] S. Truitt,[20] J. Tseng,[19] N. Turini,[27] T. Uchida,[37] F. Ukegawa,[26] J. Valls,[32] S. C. van den Brink,[15] S. Vejcik, III,[7] G. Velev,[27] I. Volobouev,[18] R. Vidal,[7] R. Vilar,[7] D. Vucinic,[19] R. G. Wagner,[1] R. L. Wagner,[7] J. Wahl,[5] N. B. Wallace,[27] A. M. Walsh,[32] C. Wang,[6] C. H. Wang,[33] M. J. Wang,[33] A. Warburton,[14] T. Watanabe,[37] T. Watts,[32] R. Webb,[34] C. Wei,[6] H. Wenzel,[16] W. C. Wester, III,[7] A. B. Wicklund,[1] E. Wicklund,[7] R. Wilkinson,[26] H. H. Williams,[26] P. Wilson,[7] B. L. Winer,[23] D. Winn,[20] D. Wolinski,[20] J. Wolinski,[21] S. Worm,[22] X. Wu,[10] J. Wyss,[27] A. Yagil,[7] W. Yao,[18] K. Yasuoka,[37] G. P. Yeh,[7] P. Yeh,[33] J. Yoh,[7] C. Yosef,[21] T. Yoshida,[24] I. Yu,[7] A. Zanetti,[36] F. Zetti,[27] and S. Zucchelli[2]

(CDF Collaboration)

[1] *Argonne National Laboratory, Argonne, Illinois 60439*

[2] *Istituto Nazionale di Fisica Nucleare, University of Bologna, I-40127 Bologna, Italy*

[3] *Brandeis University, Waltham, Massachusetts 02254*

[4] *University of California at Los Angeles, Los Angeles, California 90024*

[5] *University of Chicago, Chicago, Illinois 60637*

[6] *Duke University, Durham, North Carolina 27708*

[7] *Fermi National Accelerator Laboratory, Batavia, Illinois 60510*

[8] *University of Florida, Gainesville, Florida 32611*

[9] *Laboratori Nazionali di Frascati, Istituto Nazionale di Fisica Nucleare, I-00044 Frascati, Italy*

[10] *University of Geneva, CH-1211 Geneva 4, Switzerland*

[11] *Harvard University, Cambridge, Massachusetts 02138*

[12] *Hiroshima University, Higashi-Hiroshima 724, Japan*

[13] *University of Illinois, Urbana, Illinois 61801*

[14] *Institute of Particle Physics, McGill University, Montreal H3A 2T8, and University of Toronto, Toronto M5S 1A7, Canada*

[15] *The Johns Hopkins University, Baltimore, Maryland 21218*

[16] *Institut für Experimentelle Kernphysik, Universität Karlsruhe, 76128 Karlsruhe, Germany*

[17] *National Laboratory for High Energy Physics (KEK), Tsukuba, Ibaraki 305, Japan*

[18] *Ernest Orlando Lawrence Berkeley National Laboratory, Berkeley, California 94720*

[19] *Massachusetts Institute of Technology, Cambridge, Massachusetts 02139*

[20] *University of Michigan, Ann Arbor, Michigan 48109*

[21] *Michigan State University, East Lansing, Michigan 48824*

[22] *University of New Mexico, Albuquerque, New Mexico 87131*

[23] *The Ohio State University, Columbus, Ohio 43210*

[24] *Osaka City University, Osaka 588, Japan*

[25] *Universita di Padova, Istituto Nazionale di Fisica Nucleare, Sezione di Padova, I-35131 Padova, Italy*

[26] *University of Pennsylvania, Philadelphia, Pennsylvania 19104*

[27] *Istituto Nazionale di Fisica Nucleare, University and Scuola Normale Superiore of Pisa, I-56100 Pisa, Italy*

[28] *University of Pittsburgh, Pittsburgh, Pennsylvania 15260*

[29] *Purdue University, West Lafayette, Indiana 47907*

[30] *University of Rochester, Rochester, New York 14627*

[31] *Rockefeller University, New York, New York 10021*

[32] *Rutgers University, Piscataway, New Jersey 08855*

[33] *Academia Sinica, Taipei, Taiwan 11530, Republic of China*

[34] *Texas A&M University, College Station, Texas 77843*

[35] *Texas Tech University, Lubbock, Texas 79409*

[36] *Istituto Nazionale di Fisica Nucleare, University of Trieste/ Udine, Italy*

[37] *University of Tsukuba, Tsukuba, Ibaraki 305, Japan*

[38] *Tufts University, Medford, Massachusetts 02155*

[39] *Waseda University, Tokyo 169, Japan*

[40] *University of Wisconsin, Madison, Wisconsin 53706*

[41] *Yale University, New Haven, Connecticut 06520*

Bibliography

[1] J. Dalton, *A New System of Chemical Philosophy, Parts I and II* (Weale, London, 1810).

[2] H. Becquerel, *Sur les Propriétés Différentes des Radiations Invisibles Émises par les Sels d'Uranium, et du Rayonnement de la Paroi Anticathodique d'un Tube de Crookes*, Compt. Ren. **122**, 762 (1896).

[3] H. Becquerel, *Émission de Radiations Nouvelles par l'Uranium Métallique*, Compt. Ren. **122**, 1086 (1896).

[4] J. J. Thomson, *Cathode Rays*, Phil. Mag. **44**, 293 (1897).

[5] J. J. Thomson, *Cathode Rays*, Nature **55**, 453 (1897).

[6] E. Rutherford, *The Scattering of α and β Particles by Matter and the Structure of the Atom*, Phil. Mag. **21**, 669 (1911).

[7] J. Chadwick, *Possible Existence of a Neutron*, Nature **129**, 312 (1932).

[8] W. Pauli, *Structure et Proprietes des Noyaux Atomique*, PARIS-34 (1934), unpublished.

[9] P. A. M. Dirac, *Quantized Singularities in the Electromagnetic Field*, Proc. Roy. Soc. **A133**, 60 (1931).

[10] C. D. Anderson, *The Positive Electron*, Phys. Rev. **43**, 491 (1933).

[11] S. H. Neddermeyer and C. D. Anderson, *Note on the Nature of Cosmic-Ray Particles*, Phys. Rev. D **51**, 884 (1937).

[12] H. Yukawa, *On the Interaction of Elementary Particles. I.*, Proc. Phys.-Math. Soc. Jap. **17**, 48 (1935).

[13] D. H. Perkins, *Nuclear Disintegration by Meson Capture*, Nature **159**, 126 (1947).

[14] G. P. S. Occhialini and C. F. Powell, *Nuclear Disintegrations Produced by Slow Charged Particles of Small Mass*, Nature **159**, 186 (1947).

[15] M. Gell-Mann, *The Eightfold Way: A Theory of Strong Interaction Symmetry*, Caltech Internal Note CTSL-20 (1961), unpublished.

[16] M. Gell-Mann and Y. Ne'eman, *The Eightfold Way: A Review - With Collection of Reprints, Frontiers in Physics* (W. A. Benjamin, Inc., New York, 1964).

[17] Y. Ne'eman, *Derivations of Strong Interactions from a Gauge Invariance*, Nucl. Phys. **26**, 222 (1961).

[18] M. Gell-Mann, in *Proceedings of the International Conference on High Energy Physics* (CERN, Geneva, 1964), p. 105.

[19] V. E. Barnes *et al.*, *Observation of a Hyperon with Strangeness Minus Three*, Phys. Rev. Lett. **12**, 204 (1964).

[20] M. Gell-Mann, *A Schematic Model of Baryons and Mesons*, Phys. Lett. **8**, 214 (1964).

[21] G. Zweig, *An SU(3) Model for Strong Interaction Symmetry and its Breaking I*, CERN preprint CERN-8182-TH-401 (1964), unpublished.

[22] G. Zweig, *An SU(3) Model for Strong Interaction Symmetry and its Breaking II*, CERN preprint CERN-8419-TH-412 (1964), unpublished.

[23] S. L. Glashow, *Partial-Symmetries of Weak Interactions*, Nucl. Phys. **22**, 579 (1961).

[24] S. Weinberg, *A Model of Leptons*, Phys. Rev. Lett. **19**, 1264 (1967).

[25] A. Salam, *Weak and Electromagnetic Interactions* (Almqvist and Wiksells, Stockholm, 1968), p. 367.

[26] F. Abe *et al.*, *Evidence for Top Quark Production in $\overline{p}p$ Collisions at $\sqrt{s} = 1.8$ TeV*, Phys. Rev. Lett. **73**, 225 (1994).

[27] F. Abe *et al.*, *Evidence for Top Quark Production in $\overline{p}p$ Collisions at $\sqrt{s} = 1.8$ TeV*, Phys. Rev. D **50**, 2966 (1994).

[28] F. Abe *et al.*, *Observation of Top Quark Production in $\overline{p}p$ Collisions with the Collider Detector at Fermilab*, Phys. Rev. Lett. **74**, 2626 (1995).

[29] S. Abachi *et al.*, *Observation of the Top Quark*, Phys. Rev. Lett. **74**, 2632 (1995).

[30] N. Cabibbo, *Unitarity Symmetry and Leptonic Decays*, Phys. Rev. Lett. **10**, 531 (1963).

[31] M. Kobayashi and K. Maskawa, *CP-Violation in the Renormalizable Theory of Weak Interaction*, Prog. Theor. Phys. **49**, 652 (1973).

[32] S. L. Glashow, J. Iliopoulos, and I. Maiani, *Weak Interaction with Lepton-Hadron Symmetry*, Phys. Rev. D **2**, 1285 (1970).

[33] J.-E. Augustin *et al.*, *Discovery of a Narrow Resonance in e^+e^- Annihilation*, Phys. Rev. Lett. **33**, 1406 (1974).

[34] C. Bacci *et al.*, *Preliminary Result of Frascati (ADONE) on the Nature of a New 3.1-GeV Particle Produced in e^+e^- Annihilation*, Phys. Rev. Lett. **33**, 1408 (1974).

[35] J. J. Aubert *et al.*, *Experimental Observation of a Heavy Particle J*, Phys. Rev. Lett. **33**, 1404 (1974).

[36] M. K. Gaillard and B. W. Lee, *Search for Charm*, Rev. Mod. Phys. **47**, 277 (1975).

[37] S. W. Herb *et al.*, *Observation of a Dimuon Resonance at* 9.5-*GeV in* 400-*GeV Proton-Nucleus Collisions*, Phys. Rev. Lett. **39**, 252 (1977).

[38] P. Nason, S. Dawson, and R. K. Ellis, *The Total Cross Section for the Production of Heavy Quarks in Hadronic Collisions*, Nucl. Phys. **B303**, 607 (1988).

[39] P. Nason, S. Dawson, and R. K. Ellis, *The One Particle Inclusive Cross Section for Heavy Quark Production in Hadronic Collisions*, Nucl. Phys. **B327**, 49 (1989).

[40] B. Andersson, G. Gustafson, G. Ingelman, and T. Sjostrand, *Parton Fragmentation and String Dynamics*, Phys. Rep. **97**, 31 (1983).

[41] R. D. Field and R. P. Feynman, *A Parametrization of the Properties of Quark Jets*, Nucl. Phys. **B136**, 1 (1978).

[42] C. Peterson, D. Schlatter, I. Schmitt, and P. M. Zerwas, *Scaling Violations in Inclusive e^+e^- Annihilation Spectra*, Phys. Rev. D **27**, 105 (1983).

[43] J. Chrin, *Upon the Determination of Heavy Quark Fragmentation Functions in e^+e^- Annihilation*, Z. Phys. **C36**, 163 (1987).

[44] B. Barish *et al.*, *Measurement of the $\overline{B} \to D^* l \overline{\nu}$ Branching Fractions and $|V_{cb}|$*, Phys. Rev. D **51**, 1014 (1995).

[45] C. P. Jessop *et al.*, *Measurement of the Decay Amplitudes and Branching Fractions of $B \to J/\psi K^*$ and $B \to J/\psi K$ Decays*, Phys. Rev. Lett. **79**, 4533 (1997).

[46] F. Abe *et al.*, *Ratios of Bottom Meson Branching Fractions Involving J/ψ Mesons and Determination of b Quark Fragmentation Fractions*, Phys. Rev. D **54**, 6596 (1996).

[47] F. Abe *et al.*, *A Measurement of b Quark Fragmentation Fractions Into Strange and Light B Mesons in $p\overline{p}$ Collisions at $\sqrt{s} = 1.8$ TeV*, to be submitted to Phys. Rev. D.

[48] D. Buskulic *et al.*, *Measurement of the Decay Amplitudes and Branching Fractions of $B \to J/\psi K^*$ and $B \to J/\psi K$ Decays*, Phys. Lett. B **359**, 236 (1995).

[49] C. Caso *et al.*, *The 1998 Review of Particle Properties*, The European Physical Journal **C3**, 1 (1998).

[50] R. Barate *et al.*, *Measurement of the b Baryon Lifetime and Branching Fractions in Z Decays*, The European Physical Journal **C2**, 197 (1998).

[51] P. Abreu *et al.*, *Lifetime and Production Rate of Beauty Baryon from Z Decays*, Z. Phys. **C68**, 375 (1995).

[52] F. Abe *et al.*, *Observation of B_c Mesons in $p\overline{p}$ Collisions at $\sqrt{s} = 1.8$ TeV*, Fermilab preprint FERMILAB-PUB-98/121-E, submitted to Phys. Rev. D.

[53] G. Bocquet *et al.*, *A Study of Particle Ratios and Strangeness Suppression in $p\overline{p}$ Collisions at $\sqrt{s} = 630$ GeV with UA1*, Phys. Lett. B **366**, 447 (1996).

[54] F. Abe *et al.*, *K^0_S Production in $\overline{p}p$ Interactions at $\sqrt{s} = 630$ GeV and 1800 GeV*, Phys. Rev. D **40**, 3791 (1989).

[55] J. D. Richman and P. R. Burchat, *Leptonic and Semileptonic Decays of Charm and Bottom Hadrons*, Rev. Mod. Phys. **67**, 893 (1995).

[56] J. J. Sakurai, *Mass Reversal and Weak Interactions*, Nuovo Cim. **7**, 649 (1958).

[57] B. Grinstein, M. B. Wise, and N. Isgur, *Weak Mixing Angles From Semileptonic Decays Using the Quark Model*, Phys. Rev. Lett. **56**, 298 (1986).

[58] N. Isgur *et al.*, *Semileptonic B and D Decays in the Quark Model*, Phys. Rev. D **39**, 799 (1989).

[59] A. D. Rújula, H. Georgi, and S. Glashow, *Hadron Masses in a Gauge Theory*, Phys. Rev. D **12**, 147 (1975).

[60] S. Henderson *et al.*, *Measurements of Semileptonic Branching Fractions of B Mesons at the $\Upsilon(4S)$ Resonance*, Phys. Rev. D **45**, 2212 (1992).

[61] G. Garron *et al.*, *Stochastic Cooling Tests in ICE*, Phys. Lett. **B77**, 353 (1978).

[62] D. Mohl, G. Petrucci, L. Thorndahl, and S. van der Meer, *Physics and Technique of Stochastic Cooling*, Phys. Rep. **58**, 73 (1980).

[63] S. van der Meer, *Stochastic Cooling in the CERN Antriproton Accumulator*, IEEE Trans. Nucl. Sci. **28**, 1994 (1981).

[64] F. Abe *et al.*, *The CDF Detector: An Overview*, Nucl. Instrum. Meth. **A271**, 387 (1988).

[65] P. Azzi *et al.*, *SVX', the New CDF Silicon Vertex Detector*, Nucl. Instrum. Meth. **A360**, 137 (1995).

[66] F. Bedeschi *et al.*, *Design and Construction of the CDF Central Tracking Chamber*, Nucl. Instrum. Meth. **A268**, 50 (1988).

[67] L. Balka *et al.*, *The CDF Central Electromagnetic Calorimeter*, Nucl. Instrum. Meth. **A267**, 272 (1988).

[68] L. Nodulman *et al.*, *Central Shower Counter Prototype for the Fermilab Collider Detector Facility*, Nucl. Instrum. Meth. **204**, 351 (1983).

[69] S. Bertolucci *et al.*, *The CDF Central and Endwall Hadron Calorimeter*, Nucl. Instrum. Meth. **A267**, 301 (1988).

[70] D. Amidei *et al.*, *The CDF Trigger*, Nucl. Instrum. Meth. **A265**, 326 (1988).

[71] F. Abe *et al.*, *Measurement of the Antiproton-Proton Total Cross Section at* $\sqrt{s} = 546$ *and* 1800 *GeV*, Phys. Rev. D **50**, 5550 (1994).

[72] J. T. Carroll *et al.*, *The CDF Level 3 Trigger*, Nucl. Instrum. Meth. **A300**, 552 (1991).

[73] A. B. Wicklund and F. Ukegawa, *Hadron Backgrounds in the Inclusive Electron Sample*, CDF Internal Note CDF-ANAL-ELECTRON-PUBLIC-1640 (1991), unpublished.

[74] N. Solomey and A. B. Wicklund, *Study of Electromagnetic Showers in the CDF Central Electromagnetic Calorimeter*, CDF Internal Note CDF-DOC-CDF-PUBLIC-247 (1984), unpublished.

[75] D. Amidei *et al.*, *New Shower Maximum Trigger for Electrons and Photons at CDF*, FERMILAB-CONF-94-243-E, Presented at the Eighth Meeting of the Division of Particles and Fields of the American Physical Society, University of of New Mexico, Albuquerque, NM (1994), unpublished.

[76] T. Dorigo, *A Trigger Breakdown of the Inclusive Central Electron Datasets*, CDF Interal Note CDF-PHYS-BOTTOM-CDFR-4079 (1997), unpublished.

[77] M. Gold, *Identification of Conversion Electron Pairs*, CDF Internal Note CDF-ANAL-ELECTRON-CDFR-913 (1989), unpublished.

[78] K. J. Ragan, J. J. Walsh, and H. H. Williams, *Identification of Photon Conversions*, CDF Interal Note CDF-ANAL-ELECTRON-CDFR-902 (1989), unpublished.

[79] G. Unal, *Conversions in the 1992 Data*, CDF internal documentation (1993), unpublished.

[80] F. Abe *et al.*, *Measurement of the Bottom-Quark Production Cross Section Using Semileptonic Decay Electrons in $p\overline{p}$ Collisions at $\sqrt{s} = 1.8$ TeV*, Phys. Rev. Lett. **71**, 500 (1993).

[81] A. Warburton, *Run 1A and 1B Low-p_t Single- and Double-Track CTC Pattern Recognition Efficiencies*, CDF Internal Note CDF-ANAL-BOTTOM-CDFR-4139 (1997), unpublished.

[82] P. Sphicas, *A $b\overline{b}$ Monte Carlo Generator*, CDF Internal Note CDF-DOC-BOTTOM-CDFR-2655 (1994), unpublished.

[83] A. D. Martin, R. G. Roberts, and W. J. Stirling, *Parton Distributions Updated*, Phys. Lett. **B306**, 145 (1993).

[84] J. Lewis and P. Avery, *CLEOMC: The CDF Interface to the CLEO Monte Carlo (QQ)*, CDF Internal Note CDF-DOC-MONTECARLO-PUBLIC-2724 (1994), unpublished.

[85] D. Scora, Ph.D. thesis, University of Toronto, Toronto, Ontario, 1992.

[86] M. Shapiro *et al.*, *A User's Guide to QFL*, CDF Internal Note CDF-1810 (1992), unpublished.

[87] W. Trischuk and A. Warburton, *A Parametrisation for the Run 1 Low p_t CTC Track Finding Efficiency*, CDF Internal Note CDF-ANAL-TRACKING-CDFR-4423 (1997), unpublished.

[88] K. Byrum and A. B. Wicklund, *The Level-2 Trigger Efficiency for 9 GeV Electrons in Run IA*, CDF Internal Note CDF-MEMO-ELECTRON-GROUP-3120 (1996), unpublished.

[89] K. Byrum and A. B. Wicklund, *The Level-2 Trigger Efficiency for 9 GeV Electrons in Run IA - Part II*, CDF Internal Note CDF-MEMO-ELECTRON-GROUP-3665 (1996), unpublished.

[90] W. J. Taylor, K. Byrum, and P. K. Sinervo, *Run 1B Level 2 CEM_8_CFT_7_5 and XCES Electron Trigger Efficiencies*, CDF Internal Note CDF-DOC-TRIGGER-CDFR-4691 (1998), unpublished.

[91] F. James, *MINUIT - Function Minimization and Error Analysis*, CERN Program Library Long Writeup D506 (1994), unpublished.